TECHNISCHE UNIVERSITÄT WIEN

DISSERTATION

Development of a PET module prototype toward 100 ps FWHM timing resolution

zur Erlangung des akademischen Grades eines
Doktors der Naturwissenschaften
unter der Leitung von

Prof. Johann Marton

E141 - Atominstitut
eingereicht an der Technischen Universität Wien
Fakultät für Physik

von

Giulia Terragni, M.Sc.
Matrikelnummer 12131123

Wien, 18.10.2024

Abstract

Fast-timing radiation detectors are leading to numerous innovations in the fields of high energy physics (HEP) and medical physics. One of the possible applications in the field of medical physics is positron emission tomography (PET). PET is a functional imaging technique able to provide 3D information on the metabolic activity in a living organism. To achieve this, a β^+-emitting isotope embedded in a drug that follows a specific metabolic pathway is injected into the patient. As a result of the β^+ decay, the positron annihilates with an electron, and two back-to-back gamma photons of 511 keV energy are produced. The gammas are detected in coincidence using detector blocks placed around the patient and organized in rings, made of scintillators, photodetectors, and readout electronics. They allow for the reconstruction of the line along which the annihilation process took place, called line of response (LOR). After the accumulation of many LORs, the reconstruction of a 3D image is possible.

The localization of the electron-positron annihilation along a LOR can be obtained by measuring the time difference between the detection of the two photons, known as time of flight (TOF), whose accuracy is defined by the coincidence time resolution (CTR). In TOF-PET this information allows to improve the signal-to-noise ratio (SNR) and therefore the quality of the reconstructed image. This resolution is affected by all components in the detector chain and, hence, to improve its performance, a careful optimization of all detector elements is needed.

The current state-of-the-art CTRs for commercially available PET scanners were set by the Siemens Biograph Vision PET/CT scanner, with a time resolution of 214 ps full-width-at-half-maximum (FWHM), and the Biograph Vision.X PET/CT system, with a even better time resolution of 178 ps FWHM thanks to the use of artificial intelligence. Such a good time resolution already leads to a 3 cm spatial resolution along the LOR. Nonetheless, a number of medical challenges call for a further improvement in TOF precision of TOF-PET scanners. Achieving a CTR of 100 ps FWHM translates to a shorter examination time or a lower radioactive dosage administered to the patient. The ultimate goal is to reach 10 ps FWHM, which translates to 1.5 mm spatial resolution and also corresponds to the range of the positron. This level of precision would provide the true space points of positron annihilation, enabling reconstruction-less imaging.

Scintillating inorganic crystals like lutetium–yttrium oxyorthosilicate (LYSO) represent the best scintillator for TOF-PET scanners, owing to their high light yield and fast scintillation kinetics. With new advancements in silicon photomultiplier (SiPM) technologies and electronics readouts, the timing performance of this scintillator is pushed

to its limit. As a consequence, the depth of interaction (DOI) of a gamma inside the scintillator and its contribution to the CTR are no longer negligible. This is particularly important in preclinical and organ-dedicated human PET scanners, which require high spatial resolution and sensitivity to achieve detailed imaging and high SNR.

This thesis investigates a detector block made of a set of crystals with depolished lateral surfaces together with a light guide placed on top of it to enable light sharing between neighboring crystals, and thus allow for the extraction of DOI information of gamma rays. This approach is applied to a matrix of 15 mm long LYSO:Ce scintillators and the most advanced SiPMs available, using both custom-made and commercially available electronic readout systems. The custom-made readout is based on the NINO 32-chip used for time extraction and on an analog amplifier for energy extraction. The readout processes each SiPM output signal of the array, which is later digitized with a sampling rate of 5 GS/s. With this setup and using the new Metal-in-Trench SiPM technology, a CTR of 170 $\pm$ 5 ps FWHM is achieved after DOI correction, along with a DOI resolution of 2.5 $\pm$ 0.2 mm FWHM. On the other hand, using the PETsys TOFPET2 ASIC, a commercially available electronic readout, a CTR of 216 $\pm$ 6 ps FWHM and a DOI resolution of 2.6 $\pm$ 0.2 mm FWHM are obtained. The PETsys TOFPET2 ASIC readout is chosen for comparison to assess the detector's performance and applicability to future scalable systems of several thousands of channels.

In addition, a custom-made and sixteen-channel low-noise, low-power, high-frequency (LNLPHF) board is tested to further enhance the time resolution by making use of a lower leading-edge threshold that allows the detection of the earliest photons produced, such as Cherenkov photons. Using 20 mm long crystals, commonly used in commercial PET scanners, the DOI-capable detector block achieves a new benchmark CTR of 133 $\pm$ 2 ps FWHM after DOI correction. For comparison, the CTR of the standard (non-DOI) module of the same length is 130 $\pm$ 2 ps FWHM. Thus, the DOI-capable concept not only achieves similar performance as the standard configuration but also has the benefit of retrieving the DOI information, which can later be used to correct parallax errors in scanners.

The merits of the LNLPHF board become particularly visible in crystals with slow scintillation profiles where, however, few Cherenkov photons are produced owing to these crystals' high refractive index, such as in bismuth germanate (BGO) or in scintillators with high photon density, such as in plastic. In fact, the timing resolution of these materials crucially depends on the threshold applied to extract the time information. If 250 μm thick layers of BGO and plastic scintillators are alternately stacked, in the so-called heterostructure concept, the fast scintillation production of the plastic and the high stopping power of BGO can be combined in one "crystal", and the light attenuation due to the stratification of the layers be used to retrieve the DOI information by means of a light sharing mechanism. Selecting events where part of the energy is shared between the two materials and using the DOI information for time correction, a CTR of 182 $\pm$ 6 ps FWHM is achieved with a matrix of 20 mm long heterostructured scintillators. This approach offers a cost-effective compromise between adequate time resolution and high sensitivity.

Finally, the DOI-capable detector block is used to explore a new statistical method designed to identify the first crystal-of-interaction in the stack in the case of inter-crystal scatter (ICS) events. These events, in which gamma rays interact with multiple crystals, degrade spatial resolution if not properly addressed. Removing the ambiguity in the determination of the crystal of the first interaction could improve LOR delineation and therefore spatial resolution. If the expected charge distribution across all photodetectors, as a function of DOI and energy deposition, is known from prior calibration procedures, the information can be used to estimate the most probable gamma-ray interaction points across multiple crystals and accurately identify the first crystal of interaction. The statistical method is tested using Geant4 Monte-Carlo simulations and proves to be accurate to better than 85% and predicts a DOI resolution of 4.5 mm FWHM. This approach offers a novel strategy to enhance the spatial resolution of ICS events used for image reconstruction.

Zusammenfassung

Der Einsatz von Strahlungsdetektoren mit guter Zeitauflösung führt zu zahlreichen Innovationen in den Bereichen Hochenergiephysik (HEP) und medizinischer Physik. Eine der möglichen Anwendungen in dem Gebiet der medizinischen Physik ist die Positronen-Emissions-Tomographie (PET). PET ist ein funktionelles Bildgebungsverfahren, das 3D-Informationen über die Stoffwechselaktivität in einem lebenden Organismus liefern kann. Dazu wird dem Patienten ein Radiopharmakon injiziert, welches einem spezifischen metabolischen Ablauf folgt und ein Isotop enthält, das β^+ Teilchen emittiert. Als Ergebnis des β^+-Zerfalls annihiliert das Positron mit einem Elektron und es entstehen zwei gegenläufige Gammaphotonen mit einer Energie von 511 keV. Die Gammastrahlen werden mit Hilfe von Detektorblöcken, die ringförmig um den Patienten angeordnet sind und aus Szintillatoren, Photodetektoren und Ausleseelektronik bestehen, in Koinzidenz erfasst. Dies ermöglicht die Rekonstruktion einer Linie, entlang derer der Annihilationsprozess stattgefunden hat, diese wird Koinzidenzlinie (Line of Response, LOR) genannt. Nach der Erfassung vieler LORs ist die Rekonstruktion eines 3D-Bildes möglich.

Die Lokalisierung der Elektron-Positron-Annihilation entlang einer LOR kann durch Messung der Zeitdifferenz zwischen der Detektion der beiden Photonen ermittelt werden. Die Genauigkeit dieser Flugzeitbestimmung (Time of Flight, TOF) wird durch die Koinzidenz Zeitauflösung (Coincidence Time Resolution, CTR) definiert. Bei der TOF-PET Bildgebung ermöglicht diese Information eine Verbesserung des Signal-Rausch-Verhältnisses (Signal to Noise Ratio, SNR) und führt damit auch zu einer Verbesserung der Qualität des rekonstruierten Bildes. Diese Auflösung wird von allen Komponenten in der Detektorkette beeinflusst. Dadurch ist, um ihre Genauigkeit zu verbessern, eine sorgfältige Optimierung aller Detektorelemente erforderlich.

Den aktuellen Stand der Technik bei kommerziell erhältlichen TOF-PET Systemen definieren der Biograph Vision PET/CT-Scanner von Siemens mit einer Zeitauflösung von 214 ps Halbwertsbreite (full width at half maximum, FWHM) und das Biograph Vision.X PET/CT System mit einer noch besseren CTR von 178 ps FWHM dank des Einsatzes von künstlicher Intelligenz. Eine so gute Zeitauflösung entspricht einer Ortsauflösung von 3 cm entlang der LOR. Allerdings erfordern eine Reihe von medizinischen Herausforderungen eine weitere Verbesserung der TOF-Präzision. Das Erreichen einer CTR von 100 ps FWHM bedeutet eine kürzere Untersuchungszeit oder eine geringere Strahlendosis, die der Patient erfährt. Das ultimative Ziel sind 10 ps FWHM, dies entspricht 1,5 mm räumlicher Auflösung und somit auch der Reichweite von Positronen. Dadurch wäre der tatsächliche Ort der Annihilation bekannt, was eine rekonstruktions-

freie Echtzeit-Bildgebung ermöglichen würde.

Anorganische Szintillationskristalle wie Lutetium-Yttrium Oxyorthosilicat (LYSO) sind aufgrund ihrer hohen Lichtausbeute und schnellen Szintillationskinetik die erste Wahl für TOF-PET-Scanner. Angesichts der aktuellen Fortschritte bei der Entwicklung schneller Silizium Photomultiplier (SiPM) und schneller Ausleseelektronik stößt die zeitliche Auflösung dieser Szintillatoren jedoch an ihre Grenzen. Infolgedessen ist der Beitrag der Wechselwirkungstiefe (Depth of Interaction, DOI) eines Gammas im Szintillator auf die CTR nicht mehr vernachlässigbar. Dies ist besonders wichtig bei präklinischen und organspezifischen humanmedizinischen PET-Scannern, die eine hohe räumliche Auflösung und Sensitivität benötigen, um eine detaillierte Bildgebung und hohes SNR zu erreichen.

In dieser Arbeit wird ein Detektorblock untersucht, bei dem ein Satz Kristalle mit matten Seitenflächen und einem darauf platzierten Lichtleiter verwendet werden, um eine Verteilung des Lichts zwischen benachbarten Kristallen zu ermöglichen. Diese Anordnung erlaubt die Herleitung von DOI-Informationen der Gammastrahlen. Dieser Ansatz wird auf eine Matrix aus 15 mm langen LYSO:Ce-Szintillatoren und den aktuell besten SiPMs angewandt, wobei sowohl speziell angefertigte als auch kommerziell erhältliche Ausleseelektronik verwendet werden. Die speziell angefertigte Auslesetechnik basiert auf dem NINO 32-Chip für die Zeitbestimmung, einem analogen Verstärker für die Energiemessung und digitalisiert jedes SiPM-Ausgangssignal mit einer Frequenz von 5 Gs/s. Mit diesem Aufbau und unter Verwendung der neuen Metal-in-Trench SiPM-Technologie wird eine CTR von 170 ± 5 ps FWHM nach DOI-Korrektur erreicht, zusammen mit einer DOI-Auflösung von 2,5 ± 0,2 mm FWHM. Auf der anderen Seite bei Anwendung des PETsys TOFPET2 ASIC's, eines kommerziell erhältlichen elektronischen Ausleseelektronik, wird eine CTR von 216 ± 6 ps FWHM und eine DOI-Auflösung von 2,6 ± 0,2 mm FWHM erreicht. Die PETsys TOFPET2 ASIC wurde zum Vergleich ausgewählt, um die Leistung des Detektors und seine Anwendbarkeit auf zukünftige skalierbare Systeme mit mehreren Tausend Kanälen zu bewerten.

Darüber hinaus wurde eine selbst entwickelte 16-Kanal Elektronik getestet, welche rauscharm, energieeffizient und hochfrequent ist (Low-Noise Low-Power High-Frequency, LNLPHF), um durch einen noch niedrigeren Schwellenwert die Zeitauflösung zu verbessern. Dies ermöglicht die Erkennung der ersten aus der Kaskade erzeugten Photonen, wie z.B. Cherenkov-Photonen. Mit Kristallen von 20 mm Länge, einer in kommerziellen PET-Scannern üblichen Größe, erreicht der DOI-fähige Detektorblock eine beispielhafte CTR von 133 ± 2 ps FWHM, nach DOI-Korrektur. Vergleichsweise liegt die CTR des Standard-(nicht-DOI) Moduls gleicher Länge bei 130 ± 2 ps FWHM. Daraus lässt sich folgern, dass das DOI-fähige Konzept nicht nur eine ähnliche Zeitauflösung wie die Standardkonfiguration erreicht, sondern es hat auch den Vorteil, dass die DOI-Informationen abgerufen werden können, wodurch sich später Parallaxenfehler in Scannern korrigieren lassen.

Der Vorteil der LNLPHF-Elektronik zeigt sich besonders bei Kristallen mit langsameren Szintillationsprofilen, bei denen jedoch aufgrund ihres hohen Refraktionsindexes einige wenige Cherenkov-Photonen erzeugt werden, wie z. B. bei Bismutger-

manat (BGO) oder bei Szintillatoren mit hoher Photonendichte, wie z. B. bei Plastik. Die zeitliche Auflösung dieser Materialien hängt in hohem Maße von dem Schwellenwert ab, der zur Gewinnung der Zeitinformationen verwendet wird. Wenn 250 μm dicke Schichten aus BGO und Plastik abwechselnd in einem so genannten heterostrukturierten Konzept angeordnet sind, können die schnelle Szintillationsproduktion der Plastikkomponente und das hohe Stoppvermögen von BGO in einem Szintillator kombiniert werden. Außerdem kann die durch die Schichtungen bedingte Lichtabschwächung genutzt werden, um die DOI-Information mit Hilfe des Lichtleiters zu erhalten. Durch die Auswahl von Ereignissen, bei denen ein Teil der Energie zwischen den beiden Materialien geteilt wird und eine zeitliche Korrektur mithilfe der DOI-Informationen durchgeführt wird, wird eine CTR von 182 $\pm$ 6 ps FWHM mit einer Matrix aus 20 mm langen heterostrukturierten Szintillatoren erreicht. Dies stellt einen kostengünstigen Kompromiss zwischen guter Zeitauflösung und hoher Empfindlichkeit dar.

Schließlich wird der DOI-fähige Detektorblock verwendet, um eine neue statistische Methode zu untersuchen, die erlaubt, den Kristall zu identifizieren, in dem die erste Wechselwirkung bei interkristallinen Streuereignissen (Inter Crystal Scattering, ICS) stattgefunden hat. Diese Ereignisse verschlechtern die räumliche Auflösung, wenn sie nicht in geeigneter Weise behandelt werden. Die Beseitigung der Ambiguität bei der Bestimmung des Kristalls der ersten Wechselwirkung könnte die Definition der LOR und damit die räumliche Auflösung verbessern. Wenn die erwartete Ladungsverteilung über alle Fotodetektoren als Funktion von DOI und Energieabgabe aus früheren Kalibrierungsverfahren bekannt ist, können diese Informationen verwendet werden, um die wahrscheinlichsten Gammastrahlen-Wechselwirkungspunkte über mehrere Kristalle hinweg abzuschätzen und den ersten Wechselwirkungskristall genau zu identifizieren. Diese statistische Methode wird mithilfe von Geant4 Monte-Carlo-Simulationen getestet, und erweist sich als zu über 85% genau und sagt den DOI mit einer Auflösung von 4,5 mm FWHM voraus. Dieser Ansatz stellt eine neue Art dar um die räumliche Auflösung von ICS Ereignissen für die Bildrekonstruktion zu optimieren.

Contents

1 Introduction

The advancements in fast-timing detection are leading to numerous innovations, with significant potential for applications in many areas of society. There is a growing demand for increasingly precise detectors with timing capabilities across several scientific disciplines, including high-energy physics (HEP), nuclear medicine such as range verification in particle therapy and positron emission tomography (PET), and industrial sectors.

In particular, PET is a diagnostic technique able to provide an image of the metabolic activity of the patient. It detects the concentration of a radioactive biomarker that, injected in the patient, follows a specific metabolic pathway. The radiotracer is a β^+ emitting isotope embedded in a drug and chosen depending on the specific application and target. It disintegrates via β^+ decay, producing a positron (e^+) that annihilates with an electron (e^-) and consequently generates two anti-collinear 511 keV gammas. A PET system aims to detect the pair of gammas using suited detectors placed around the patient. The detection is performed using dense scintillation materials that stop the gamma and convert it into several thousand optical photons. The optical photons are then detected by a photodetector, such as a silicon photomultiplier (SiPM), that produces an electrical signal later discriminated and digitized by highly integrated readout electronics. This allows to reconstruct the line along which the annihilation process lays, the line of response (LOR), by connecting the elements detecting the two coincident gamma-photons. Clinical PET systems require several thousands of such detector channels.

An event is recorded when two gammas are detected within a certain time window. Without estimation of the difference in time of arrival of the two gammas, the annihilation event is associated with the same probability to any point along the LOR. Therefore, a high concentration of radiotracer and long acquisitions are required to extract many LORs and a complex algorithm for the image reconstruction. Time of flight (TOF)-PET introduces the use of the information on the difference in the time of arrival of the two gamma photons with sufficient accuracy to determine the position where the annihilation occurred along the LOR. The ability of a pair of detectors to determine the difference in the time of arrival of the two gamma photons is called coincidence time resolution (CTR), which translates into spatial resolution along the LOR. This, in turn, improves the signal-to-noise ratio (SNR) and therefore the quality of the

reconstructed image. The introduction of Lutetium oxyorthosilicate (LSO) scintillators made TOF-PET possible for the first time. The Biograph Vision PET/CT scanner from Siemens achieved a state-of-the-art time resolution of 214 ps [1], corresponding to 3 cm precision along the LOR.

A number of medical challenges call for further improvement of the timing and sensitivity of the scanners as it could allow to reduce the injected radiation dose, scan duration and cost [2], with the ultimate goal of real-time reconstruction-less imaging. Reaching a CTR of 100 ps would already improve the TOF precision to 1.5 cm and increase the SNR by a factor of 2.7 compared to a non-TOF image and by a factor of 1.5 compared to the Biograph Vision PET/CT scanner Siemens. The ultimate CTR goal is 10 ps, also corresponding to the range of the positron, which would translate to 1.5 mm, paving the way towards reconstruction-less imaging [3]. Achieving 100 ps represents a twofold improvement over current scanners and requires careful optimization of the whole detection chain: evaluation for the most suitable material and photodetector, optimization of the readout electronics, acquisition system and reconstruction algorithms.

LSO remains one of the most favored scintillators for PET applications, owing to its high light yield and rapid emission decay characteristics [4]. It is widely used in commercial PET scanners. With advancements in photodetector technologies and electronic readout, its timing performance is pushed to its limit. As a result, the contribution to the CTR of the depth of interaction (DOI) of a gamma inside the scintillator is no longer negligible [5]. Moreover, in preclinical and organ-dedicated human PET scanners, which require high spatial resolutions and sensitivity to achieve detailed imaging and SNR comparable to other PET applications, long scintillators with small cross-sections are used. However, this approach gives rise to distortions in the reconstructed images due to parallax effects. Parallax errors also affect the image quality of PET detectors with large fields of view. To overcome these limitations, detector configurations and methodologies to measure the DOI of the gamma rays along the main axis of the scintillators can be developed and applied to correct the parallax effect.

Other materials of interest for PET applications include plastic scintillators, which offer fast scintillation production but have low stopping power, and BGO, which provides high density and stopping power despite the slow scintillation profile. To combine the advantages and obtain a fast detector with high sensitivity, layers of the two materials can be alternated in the so-called heterostructure concept [6]. Moreover, thanks to the high refractive index of BGO, several Cherenkov photons are produced in the very first picoseconds after the gamma interaction. However, to fully exploit the fast light production mechanisms, the development of ultra-fast and low-noise electronics is essential [7].

An alternative approach to maintaining good detector sensitivity and enhancing spatial resolution is to identify the first crystal of interaction for Inter-Crystal Scatter (ICS) events using dedicated algorithms. ICS events involve energy deposits in two or

more crystals, leading to a deterioration in spatial resolution due to the mispositioning of the crystal where the initial interaction occurred. These events contribute to over half of the total coincidence events [8].

1.1 Objective and outline of the thesis

Organized into five sections, this thesis investigates the theoretical background and state-of-the-art of TOF-PET detectors and presents the research conducted to improve their overall performance, especially in terms of timing resolution.

Part I: The evolution of Positron Emission Tomography

Chapter 2: Positron Emission Tomography introduces the fundamentals of PET and PET detectors, covering the principles and history from the introduction of this imaging modality to the current state-of-the-art. It also discusses the motivation for TOF-PET and the research conducted at CERN, the framework in which this thesis work was performed.

Chapter 3: Radiation detector unit gives a detailed description of the three main components of the radiation detector used in PET. First, the material used to stop and convert the gamma into optical photons and the mechanisms of conversion investigated in this thesis work. Second, the silicon photomultipliers that convert the optical photons into an electrical pulse. Third, electronic readout designs used to amplify and shape the signals coming from the photodetector, with particular focus on the NINO, High-Frequency and PETsys TOFPET2 electronic readouts investigated in this thesis work.

Part II: Performance evaluation of a PET module prototype with DOI and TOF capabilities using different electronics

Chapter 4: TOF and DOI performance of a LYSO:Ce PET module using a custom-made NINO 32-chip board presents a sixteen-channel detector unit with TOF and DOI capability. Its performances are evaluated using different SiPM technologies and a custom-made electronics based on the NINO 32-chip.

Chapter 5: Scalability of the TOF - DOI capable PET module using PETsys TOFPET2 ASIC evaluates the performance of the module using an electronic readout commercially available and scalable to thousands of channels and compares the results to those obtained with the custom-made set-up.

Part III: Pushing the timing resolution towards 100 ps

Chapter 6: Pushing the timing performance using Low- noise Low-power High-Frequency electronics presents an emerging ultra-fast electronics based on the high-frequency readout concept and applies it to the sixteen-channel module to improve the timing performance by using the very first photons produced with the fastest light-production mechanism, Cherenkov emission, for timing estimation.

Chapter 7: Optimization of Low-noise Low-power High-frequency electronics for novel material application introduces the heterostructure concept, developed to incorporate in one scintillator two materials with complementary properties: fast timing and high stopping power. Its properties and performance are investigated using the last developed version of an ultra-fast High-Frequency concept.

Part IV: An innovative method to solve the inter-crystal scattering kinematics

Chapter 8: An innovative method to solve the inter-crystal scattering kinematics presents a statistical method utilizing the DOI-capable module to identify the first crystal of interaction in the case of ICS events, where gamma rays interact with multiple crystals. By improving the estimation of their points of interaction, these events can be used for more precise image reconstruction.

Part V: Conclusion and Outlook

Chapter 9: Summary and conclusions provides a summary and draws conclusions on the research conducted. It also outlines potential directions for future research based on the findings of this study.

I

Positron Emission Tomography

2 Fundamentals of Positron Emission Tomography

Positron emission tomography (PET) is an in-vivo imaging technique able to provide a metabolic image of a patient by measuring quantitatively the three dimensional distribution of radiolabeled biomolecules. Several techniques are available for the detection and imaging of specific biomarkers in vivo, each with its own characteristics. Among the methodologies, PET is of great interest from the view of sensitivity, since it detects from nano to femtomolar ($10^{-9} - 10^{-15}$) tracer concentration [2]. PET images biomarkers radiolabeled with isotopes disintegrating via β^+ decay and producing two almost collinear 511 keV gammas by annihilation with an electron (Figure 2.1). The two gammas are recorded by detectors placed around the patient and are the input data for image reconstruction. The carrier molecules of biomarkers can be designed to match particular characteristics of the targeted cells or metabolism. However, this technique does not come without limitations. PET entails a high radiation dose for patients, and its spatial resolution is less optimal than techniques such as computed tomography (CT) and magnetic resonance imaging (MRI). Despite these constraints, PET's microscopic insight into metabolic processes renders it indispensable to medical

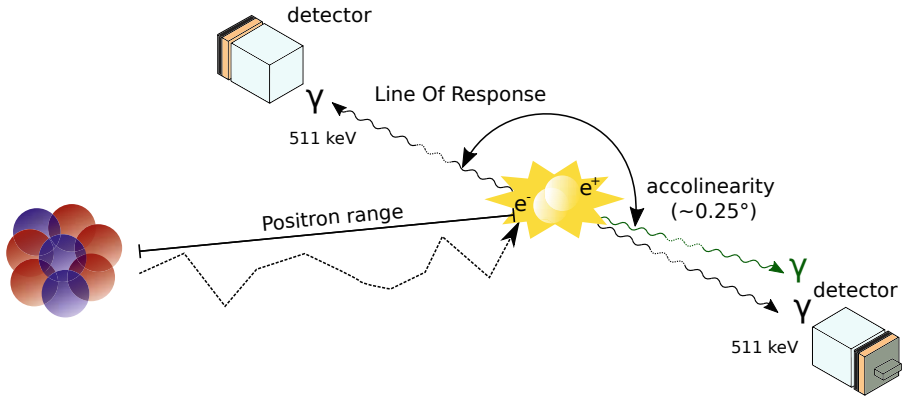

Figure 2.1: Principle of PET. Positron emission via β^+ decay, its annihilation with an electron of the tissue into two 511 keV gammas that are detected in coincidence, creating a line of response.

imaging.

In this chapter, the basic principles of PET (radioactive tracers, $\beta+$ emission and detection, the use of the detected information for image reconstruction, scatter event detection, and parallax error) are initially outlined in Section 2.1. Section 2.2 illustrates the significant historical events and developments that have contributed to the current state of PET technology. Section 2.3 introduces the time-of-flight (TOF) technique as a potential means of enhancing spatial resolution and PET image quality, and discusses the benefits derived from it.

2.1 Physical principles of PET

To reconstruct the three-dimensional image of the metabolic activity of the body, a radioactive biomarker (radiotracer) that follows a specific metabolic pathway is injected or inhaled by the patient. It is a β^+ emitting isotope embedded in a drug, which is chosen depending on the specific application and target. The positron will undergo collisions in the tissue until being thermalized with the environment. The mean distance the positron will be spread is called the positron range. This spread leads to a spatial smearing of the tracer distribution in the reconstructed image. As a result of the annihilation of the emitted positron with an electron of the body, two back-to-back 511 keV gamma photons are produced ($e + e^- \rightarrow 2\gamma$) and detected in coincidence by radiation detectors, made of crystals coupled to photodetectors, placed around the patient. Due to the residual momentum of the electron-positron pair before annihilation, the produced gammas are not perfectly collinear, introducing an additional degradation to the spatial resolution [9].

Locating the interaction of the two annihilation gammas in detectors placed around the patient, a Line of Response (LOR) is defined connecting the two points and on it the annihilation position lays. Tracing several LORs, it is possible to extract the activity distribution of the radioisotope in the body by means of reconstruction algorithms. The activity distribution represents the tracer concentration and provides an insight into the physiology or pathology of the patient.

2.1.1 Radioactive tracers

The radioactive tracer is a positron emitter radiopharmaceutical, i.e. a chemical compound in which one or more atoms are replaced with a β^+ short-lived radioisotope. It is injected into the patient and follows a specific metabolic pathway depending on the compound, the application and the target.

The possibility of using radiotracers in PET, as well as in other fields of nuclear medicine, is due to the discovery of the positron (1932, C. D. Anderson, Nobel Prize in 1936 "for his discovery of the positron" [10]), of the cyclotron (1929, E. O. Lawrence, Nobel Prize 1939 "for the invention and development of the cyclotron and for results obtained with it, especially with regard to artificial radioactive elements" [11]) and of the principle of radiotracers (1923, George de Hevesy, Nobel Prize 1943 "for his work

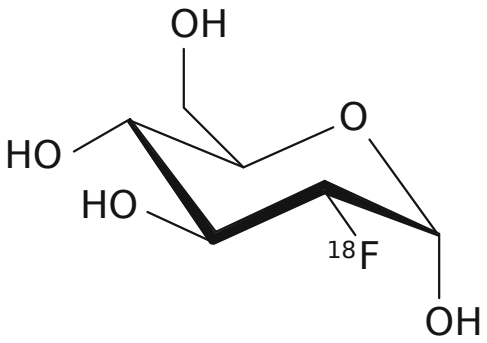

Figure 2.2: Skeletal chemical formula of Fluorodeoxyglucose PET tracer ($[^{18}F]FDG$, glucose metabolism). Data from [14].

on the use of isotopes as tracers in the study of chemical processes." [12]). Positron sources are not stable in nature and need to be artificially produced bombarding stable isotopes with positively charged particles by means of a cyclotron. The produced nucleus has a different Z value from the target nucleus and therefore the two species are chemically separable. Finally, thanks to the principle of radiotracers, which states that the changing of an atom in a molecule with its radioisotope does not change its chemical and biological behaviour significantly [12], it is possible to measure the distribution and concentration of a molecule in the body by loading the molecule with a radioisotope and subsequently detecting the product of its gamma or beta decay.

To date, the most used PET radiopharmaceutical in oncology is fluorine - 18 - fluorodeoxyglucose (F-18-FDG, Figure 2.2), a radiolabelled glucose analogue in which fluorine, replacing the normal hydroxyl group OH at the C-2 position in the molecule, is present in its unstable isotope, fluorine-18 (^{18}F). It allows the detection of neoplastic cells due to their frequently increased glucose metabolism and, consequently, their increased uptake to this tracer [13].

Other commonly used isotopes in radiopharmaceutical are listed in Table 2.1.

2.1.2 β^+ emission

The radiotracer, depending on the compound and the metabolic pathways, accumulates in specific area of the body and its concentration can be measured by detecting the product of its β^+ decay

$$ {}^{A}_{Z}X_N \xrightarrow{\tau_A} {}^{A}_{Z-1}Y_{N+1} \; + \; e^+ \; + \; \nu_e \tag{2.1} $$

in which a proton (p) of the radioisotope X decays in a neutron (n), a positron (e^+) and an electronic neutrino (ν_e). Being this a three-body decay process, the positron can be emitted with any energy up to the maximum available in the decay, resulting in a typical continuous emission spectrum. It loses this energy through multiple Coulomb interactions with orbital electrons of the tissue atoms. Once it reaches thermal equilibrium with the tissue, it forms an unstable bound state with an electron, the positronium,

Table 2.1: Common isotopes and their main physical properties. Some of the nuclear reactions used for the production are also listed [15, 16].

Isotope	Nuclear reaction	Half-life (min)	Average e^+ kin. energy (keV)	Max. e^+ kin. energy (keV)	Average e^+ range in water (mm)
^{11}C	^{14}N(p,α)^{11}C	20.4	385	960	1.2
^{13}N	^{13}C(p,n)^{13}N	10.0	491	1198	1.6
	^{16}O(p,α)^{13}N				
^{15}O	^{14}N(d,n)^{15}O	2.0	735	1732	2.8
	^{15}N(p,n)^{15}O				
^{18}F	^{16}O(p,n)^{18}F	109.8	242	633	0.6

which annihilates into two quasi-anti collinear gamma with 511 keV each, while the neutrino rarely interacts with matter. The two back-to-back gammas are detected in coincidence, outlining a LOR along which the annihilation occurs. This mechanism is illustrated in Figure 2.1. In order to reconstruct the position of the annihilation events, many LORs need to be acquired and processed with reconstruction algorithms. While several sources of uncertainty on the reconstructed annihilation position in PET are related to the reconstruction algorithms or limitation of the whole system, there are two constraints intrinsic to the physics process setting a limit to the best achievable spatial resolution:

- *The range of the positron.* The mean distance the positron travels before the annihilation occurs sets a lower limit to the spatial resolution of PET. It strongly depends on the initial kinetic energy and thus on the type of used radioactive isotope (see Table 2.1). The average positron range in water for ^{18}F is 0.6 mm, with 0.2 mm spread as full width at half maximum (FWHM) [16].

- *The non-collinearity of the two annihilation photons.* The annihilation occurs when the positron has reached thermal equilibrium with an electron, not at rest. Because of the conservation of momentum, the two gammas emitted are not exactly collinear. This results in a Gaussian dispersion centred at 180° of about 0.5° FWHM or when a positron annihilates in water [15]. This acollinearity leads to an additional spatial resolution degradation in the order of 2 mm for a whole body PET scanner with a ring diameter of 80 cm.

The concentration of the radioisotope in the body decreases with time and follows the standard exponential decay law

$$N(t) = N_0 \, e^{-\frac{t}{\tau}} \tag{2.2}$$

where N_0 is the number of molecules of the radiotracer at $t = 0$, and τ the mean-life of the radioisotope, defined as the time necessary to decrease the N_0 of a factor $1/e$. The

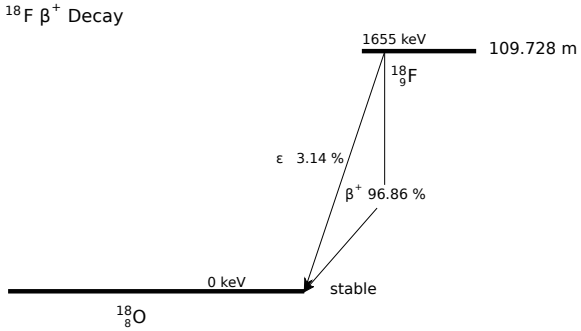

Figure 2.3: Decay scheme of ^{18}F, commonly used β^+ emitter source for PET in oncology. Data from [17].

half-life, the time necessary to halve the number of initial radioactive nuclei, is related to the mean-life according to the following equation

$$N(T_{1/2}) = \frac{N_0}{2} = N_0\, e^{-\frac{T_{1/2}}{\tau}} \rightarrow T_{1/2} = ln(2)\, \tau \tag{2.3}$$

The number of disintegrations per second, related to the concentration of the radiotracer in the body, defines the activity A of the source

$$A(t) = -\frac{dN(t)}{dt} = \frac{N(t)}{\tau} = \frac{1}{\tau}\, N_0\, e^{-\frac{T_{1/2}}{\tau}} = A_0\, e^{-\frac{T_{1/2}}{\tau}} \tag{2.4}$$

In the International System of Units (S.I.) it is measured in Becquerel ($1\,\mathrm{Bq} = 1$ disintegration/s), but another commonly used unit is Curie ($1\,\mathrm{Ci} = 3.7 \cdot 10^{10}$ Bq), which corresponds to the activity of one gram of ^{226}Ra. The half-life of the commonly used radioisotope for PET is of the order of few minutes (see Table 2.1), which allows exploiting most of the activity injected into the patient during the PET examination and reducing the radioactive waste disposal while using the minimal amount required to produce a scan. However, the short half-life imposes strict constraints on the production of the isotopes in hospitals. When it is too short for storage, it must be produced in loco and rapidly delivered. This is the case of ^{15}O.

The most used radioisotope for PET in oncology is the Fluorine-18 (^{18}F). ^{18}F is obtained bombarding the stable mother target ^{18}O with protons

$$^{18}\mathrm{O} \; + \; p \rightarrow \; ^{18}\mathrm{F} \; + \; n \tag{2.5}$$

It decays β^+ with a half-life of 109.8 min. The decay scheme is reported in Figure 2.3.

2.1.3 Gamma interaction with matter

The two gamma photons originating from the annihilation need to be revealed in suited detectors. Gamma photons can interact with matter according to three main mechanisms: Compton scattering, photoelectric absorption and pair production. Only the first two are relevant in PET since pair production requires 1022 keV energy to occur.

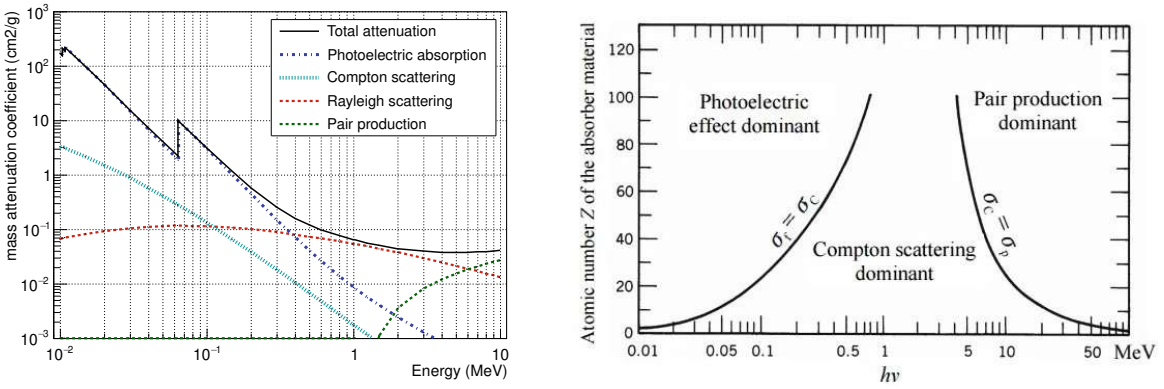

Figure 2.4: (Left) Energy dependence of gamma interaction processes in LSO. Data are taken from [20]. (Right) The relative importance of the three major types of gamma interaction. The lines show the values of Z and $h\nu$ for which the two neighboring effects are equal. Reprint from [21].

These processes lead to partial or complete transfer of the gamma energy to electrons in the material, resulting in a sudden and abrupt change in its history: the photon either disappears entirely or is scattered through a significant angle. This behavior is in marked contrast with respect to charged particles that slow down gradually through continuous interactions with the absorber atoms [18]. These processes highly depend on the energy of the photons and also on the atomic number Z of the absorber medium. Figure 2.4 on the left shows the case for lutetium oxyorthosilicate (Lu_2Si0_5 or LSO) [19] and Figure 2.4 on the right shows the relative importance of the major types of gamma interaction depending on the energy of the gamma and the Z of the material. The arguing will be later adapted to the chosen materials and to energies around 511 keV as used in PET.

Photoelectric absorption:

In the photoelectric absorption process, a photon with energy $E_\gamma = h\nu$ is completely absorbed by an electron bound to an atom. Due to the conservation of momentum and energy, this process is not possible for free electrons. However, the recoil energy of the atom involved is very small and usually can be neglected. The absorbed gamma energy is used to free the electron from one of its bound shells, with energy given by

$$E_{e^-} = h\nu - E_b \tag{2.6}$$

and as shown in Figure 2.5, where E_b is the binding energy of the electron in its original shell, thus representing a threshold for the process.

For gamma rays of sufficient energy, the most probable origin of the photoelectron is the most tightly bound K-shell of the atom. The interaction also creates a vacancy in one of the shells quickly filled through the capture of a free electron from the medium and the rearrangement of electrons from the other shells. Therefore, one or more characteristic X-ray photons may also be generated or an Auger electron emitted. If

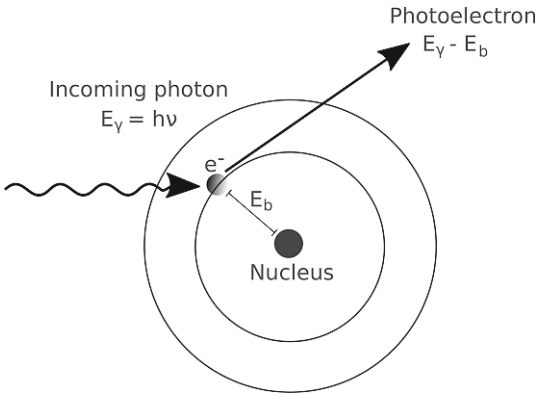

Figure 2.5: Illustration of the photoelectric absorption of a gamma.

the detector dimensions are small, then such photons can escape the detector and cause an escape peak in the energy distribution. In some cases, Auger electrons can also carry away the atomic excitation energy.

The photoelectric effect is the predominant process that takes place in the interaction of X-rays or gamma rays of low energy and high atomic number Z. Its cross-section depends both on the energy of the photons and the atomic number according to the following approximated expression

$$\tau \sim \frac{Z^n}{E_\gamma^{3.5}} \tag{2.7}$$

where the exponent n varies between 4 and 5 depending on the gamma energy range of interest.

Compton scattering:

For gamma rays of energy around 511 keV (annihilation photons), Compton scattering is the predominant process that takes place in most of the media (see Figure 2.4). The incoming photon transfers a portion of its energy to a free electron in the material and is deflected through an angle θ with respect to the original direction as shown in Figure 2.6. Using the energy and momentum conservation laws, it is possible to derive the equation relating the energy transfer and the scattering angle. Assuming the recoil electron is initially at rest, the equation is

$$h\nu' = \frac{h\nu}{1 + \frac{h\nu}{m_0c^2}(1 - \cos\theta)} \tag{2.8}$$

where $h\nu$ is the energy of the incoming photon, $h\nu'$ that of the scattered photon, and m_0c^2 the rest-mass energy of the electron. The greatest energy transfer happens at $\theta = \pi$. However, some of the original energy is anyway retained by the incident photon. For an incident gamma with energy $h\nu = 511$ keV, the minimum retained energy is $h\nu' = 170$ keV. As all angles of scattering are possible, the energy transfer can vary from zero to 511 keV - 170 keV = 341 keV, called Compton edge.

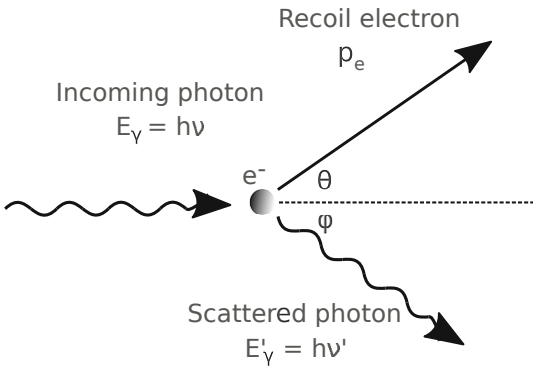

Figure 2.6: Illustration of the Compton scattering of a gamma.

Compton scattering is the dominant interaction for gamma rays in the energy range 0.1 - 1 MeV (see Figure 2.4) and its probability per atom of the absorber depends on the number of available electrons as scattering centers, therefore the cross-section scales linearly with Z. The exact differential cross-section $\frac{d\sigma}{d\Omega}$ is described by the Klein-Nishina formula [18]:

$$\frac{d\sigma}{d\Omega} = Zr_0^2 \left(\frac{1}{1+\alpha(1-\cos\theta)}\right)^2 \left(\frac{1+\cos^2\theta}{2}\right) \left(1 + \frac{\alpha^2(1-\cos\theta)^2}{(1+\cos^2\theta)[1+\alpha(1-\cos\theta)]}\right) \tag{2.9}$$

where

$$\alpha \equiv \frac{h\,\nu}{m_0\,c^2} \tag{2.10}$$

and

$$r_0 = \frac{e^2}{4\pi\epsilon_0 m_0 c^2} \tag{2.11}$$

r_0 is the classical electron radius. The angular distribution of scattered photons can be deduced from Equation 2.9 and is graphically illustrated in Figure 2.7. The plot illustrates that Compton scattering tends to be more forward-directed if the gamma photon energy is increasing.

Pair production:

If the gamma ray energy exceeds twice the rest-mass energy of an electron ($2m_0c^2 = 1.02$ MeV), the process of pair production can occur. In the coulomb field of a nucleus, the gamma ray photon disappears and is replaced by an electron-positron pair, as described in Figure 2.8. The probability of this reaction compared to Compton scattering and photoelectric absorption remains very low until the gamma energy approaches several MeV (see Figure 2.4). Therefore, pair production will be neglected in further discussions as such energies are not reached in PET.

Rayleigh scattering:

Besides Compton, another kind of process, named Rayleigh scattering, may occur whenever a photon interacts with an atom. It neither excites nor ionizes the atom. The

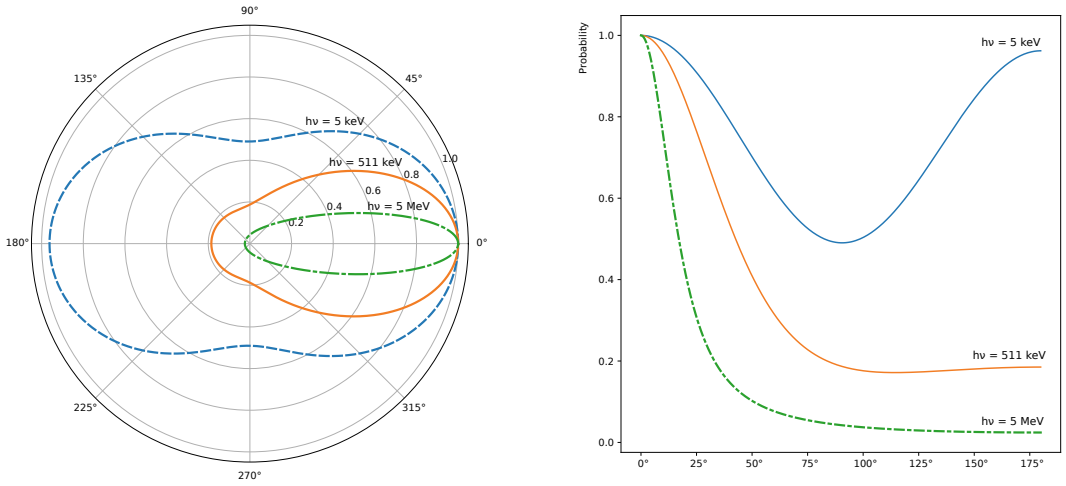

Figure 2.7: Klein-Nishina distribution for different energies. The case for gamma energy of 511 keV is also plotted.

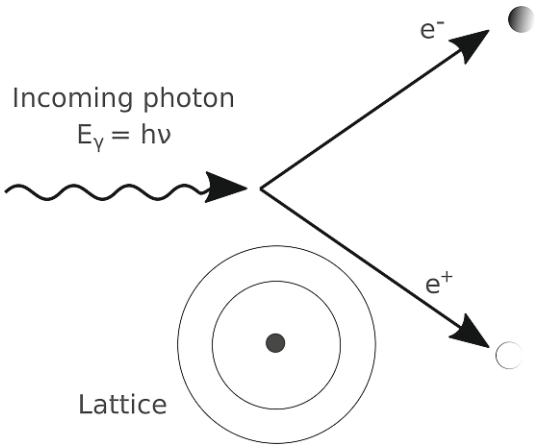

Figure 2.8: Illustration of the pair production from a gamma.

gamma photon retains its original energy after the scattering event, however, the direction of the photon is changed. This type of coherent scattering is dominant for low gamma energies and is an order of magnitude lower than the photoelectric effect and therefore is neglected for PET applications.

Gamma attenuation:

If a narrow beam of mono-energetic photons with an incident intensity I_0 is considered, each of the interaction processes described above removes the gamma photon from the beam with a fixed probability of occurrence. The total cross-section, excluding pair production, is the sum of contributions from the two principal photon interactions

$$\sigma_{tot} = \tau_{ph} \ + \ \sigma_c \tag{2.12}$$

The number of transmitted photons I can be written in terms of the number before absorption I_0 as

$$\frac{I}{I_0} = e^{-\frac{\mu}{\rho}\rho x} \tag{2.13}$$

where μ is the linear attenuation coefficient and $\frac{\mu}{\rho}$ the mass attenuation coefficient, which is related to the total cross section as

$$\frac{\mu}{\rho} = \frac{N_A}{A}\sigma_{tot} \tag{2.14}$$

with N_A the Avogadro's number ($6.02 \cdot 10^{23}$ mol[1]) and A the atomic weight of the absorber.

The gamma photon attenuation can also be described in terms of the mean free path λ, the average distance traveled in the absorber before an interaction takes place. It can be extracted as

$$\lambda = \frac{\int_0^\infty x e^{-\mu x} dx}{\int_0^\infty e^{-\mu x} dx} = \frac{1}{\mu} \tag{2.15}$$

and proves to be the reciprocal of the linear attenuation coefficient. Therefore:

$$\frac{I}{I_0} = e^{-\frac{x}{\lambda}} \tag{2.16}$$

Detection efficiency:

The detection efficiency describes the ability of a detector to stop gamma rays, e.g. 511 keV gamma photons. The detection efficiency can be expressed by the gamma attenuation length λ according to Equation 2.16. For proper detection, a low attenuation length or high attenuation coefficient is required to stop the gamma rays.

In the case of the photoelectric effect, the gamma absorption is proportional to Z^n with n in the range between 4 and 5 (see Equation 2.7). Equation 2.9 shows that the Compton scattering gamma absorption is linearly dependent on the charge number Z. Figure 2.4 shows the attenuation coefficients as a function of Z and the incident photon energy. For the particular case of LSO, $\rho = 7.4\frac{g}{cm^3}$ [19], the gamma ray attenuation length $\lambda = \frac{1}{\mu}$ is 11.5 mm.

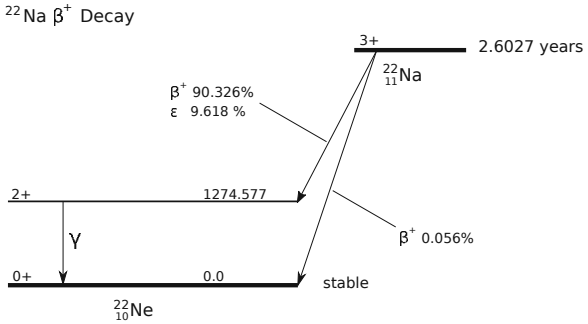

Figure 2.9: Decay scheme of ^{22}Na, commonly used β^+ emitter source in PET research because of its long half-life (2.6 years). Data from [17].

Typical energy spectrum measured with ^{22}Na:

For laboratory research purposes, β^+ emitters with longer half-life compared to ^{18}F are used, among which the most common is ^{22}Na, having a half-life of 2.6 years and whose decay scheme is reported in Figure 2.9. When using a detector for gamma radiation, the gamma photon interactions previously described can be observed in the spectrum obtained from the measurement of the energy deposition. In particular, using the ^{22}Na radioactive source, a positron is emitted when the isotope ^{22}Na decays into ^{22}Ne and the excited state of ^{22}Ne generates an additional gamma with an energy of 1274 keV going to the stable state (Figure 2.9). The positron annihilates immediately with an electron of the surroundings, producing two quasi-anti collinear gamma with 511 keV energy. Using a detector based on an LSO scintillator coupled to a photodetector, it is possible to observe the 511 keV and 1274 keV peaks associated with the photoelectric effect, the Compton edges, and plateaux (Figure 2.10). The ^{22}Na energy response is on top of the Lutetium background. On the left of the 511 keV peak, the Lutetium (^{71}Lu) escape peak can be recognized at an energy of 511 keV - 63 keV = 448 keV. Lutetium naturally contains 2.6% ^{176}Lu, which beta decays to ^{176}Hf emitting three gamma rays with energy 88 keV, 202 keV, and 307 keV. The total activity of this background is 40 cps/g for LSO [22]. The background activity is a disadvantage but can be used to calibrate the energy response of the detector using the known position of the three emitted gammas.

2.1.4 Image reconstruction

When a pair of detectors record an annihilation event, the LOR is fully characterized by its orientation in the scanner plane (angle ϕ) and its distance s from the center of the detector ring. The raw data are the accumulation of events detected on each LOR during the acquisition, i.e., the line integrals of the tracer activity distribution f, which can be defined as [23]

$$p(s,\phi) = \int_{LOR} f(x = s\cos\phi - l\sin\phi, y = s\sin\phi + l\cos\phi)dl \tag{2.17}$$

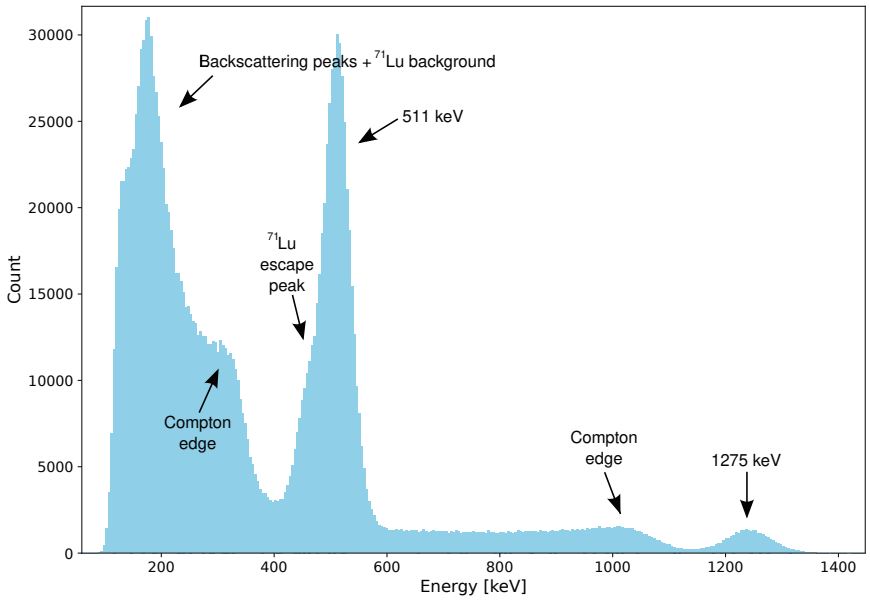

Figure 2.10: Typical energy spectrum of ^{22}Na observed using a detector for gamma radiation based on an LSO crystal.

where l is the coordinate along the line and (x, y) the Cartesian coordinate system centered in the detector's plane. The resulting function $p(s, \phi)$ is called a sinogram since the LORs, containing a reference point $(x_0,\ y_0)$, constitute a sinusoid described by $s = x_0 cos\phi + y_0 sin\phi$ in the (s, ϕ) plane (see Figure 2.11). The mathematical transformation of the function $f(x, y)$ into its line integrals $p(s, \phi)$ is called the X-ray transform, which in 2D coincides with the Radon transform, after the Austrian mathematician Johann Radon, who introduced the mathematical description already in 1917 [24]. In Figure 2.11 an example of the Radon transformation is given. On the left, a tracer distribution shows two points and a straight line while, on the right, the respective Radon transformation is illustrated. A point located in the center of the PET ring will be transformed into a horizontal line. If the point is off-centered then the transformation gives a sine wave-like function ("sinogram"). The line is given by the sum of many points. In the sinogram, every point represents the integral activity of the LOR defined by s and ϕ.

The algorithms used in tomographic reconstruction to transform the sinogram back to the original image in the coordinate space can be divided into two main categories: analytic and iterative methods. The former methods apply the inversion of the Radon transform to the measured data, while the latter ones use models that include a finite number of image values from a finite number of measurements to converge to the original image by means of successive approximations to it.

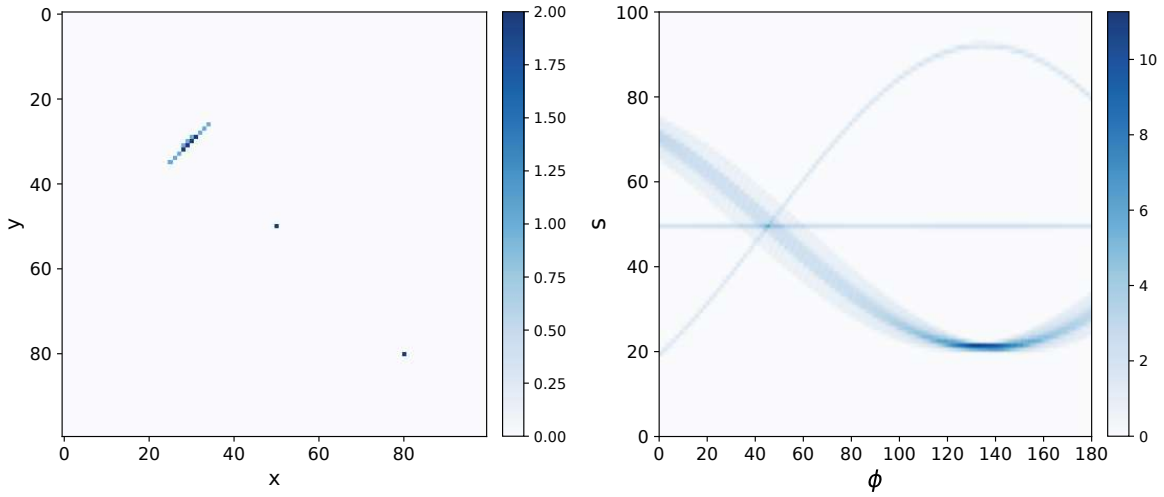

Figure 2.11: Illustration of the Radon transformation. On the left is the image in the coordinate space and on the right is the sinogram of the respective Radon transformation. Inspired by [25].

Analytic methods

The most basic analytic approach to reconstruct an image starting from its measured profiles is by filtered back projection. Data from each profile are projected back across the entire image grid and the projections of N profiles are added together [26], obtaining

$$f'(x,y) = \frac{1}{N}\sum_{i=1}^{N} p(xcos\phi_i + ysin\phi_i, \phi_i) \tag{2.18}$$

where ϕ_i is the i^{th} projection angle. The larger the number of projections N, the better the resemblance of the backprojected image with the original one. However, the simple backprojection amplifies low frequencies and, as a result, the projected image is blurred. To improve this, a filter in the frequency domain is applied before the backprojection, resulting in

$$f''(x,y) = \int_0^{\pi} p^F(xcos\phi_i + ysin\phi_i, \phi_i)d\phi \tag{2.19}$$

where p^F are the filtered projections. Filtered backprojection can be further stabilized using adequate filter functions.

Filtered back projection has been the choice in PET for many years because of its simpleness and low computational needs. However, this method has disadvantages if the recorded data is noisy.

Iterative methods

Iterative algorithms are instead based on the successive actualization of an image estimate $f^*(x,y)$, aiming to converge to the true image $f(x,y)$. They offer a viable alternative to the analytic ones to improve the image quality. The algorithm starts

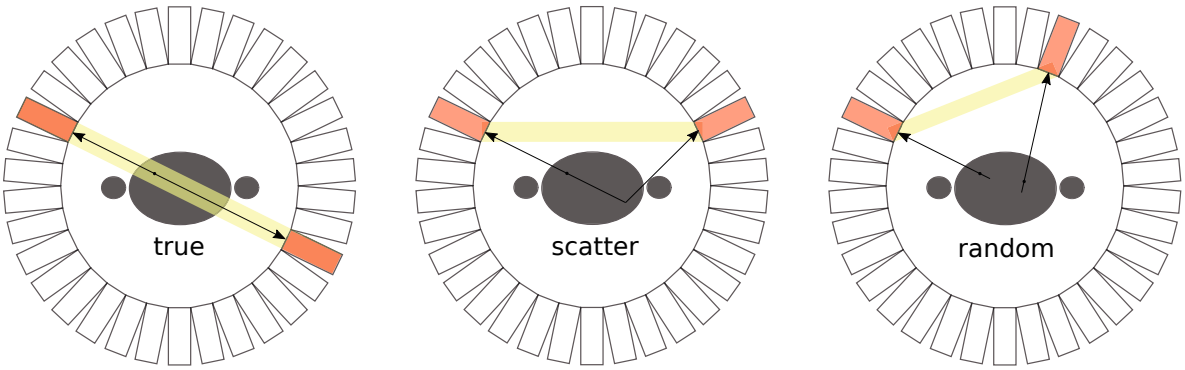

Figure 2.12: Coincidence events in PET imaging shown on a single detector ring. A true coincidence, scatter coincidence or random coincidence can take place. The last two are noise signals that worsen the reconstruction of the radiotracer distribution.

with an initial estimate, which is then forward projected to obtain the projections that would have been measured for the estimated image. The generated sinogram is then compared to the real measured set of projections and the difference between them is used to update the image estimate. The process is then repeated until $f^*(x, y)$ converges to $f(x, y)$ within an acceptable level. The Maximum Likelihood Expectation Maximization (ML-EM) algorithm is one of the most used PET reconstruction algorithms and is based on statistical considerations to compute the most likely radioactivity distribution that created the observed projections [26]. It aims to find the activity values in each pixel (voxel) that maximize the probability of the corresponding measured values, and this probability is represented by a likelihood function. This method works with data stored directly in LORs, without the need of sinograms. It is slower compared to filtered back projection but characterized by a lower noise.

The fundamentals of image reconstruction presented can be expanded to several detector rings (3D PET) as well as include correction methods for physical phenomena such as attenuation, scatter, depth of interaction, non-collinearity.

2.1.5 True, Random and Scatter Events

During a PET acquisition, different typologies of events can pass the coincidence selection: true, scatter and random coincidences (see Figure 2.12). True coincidences provide the correct LOR along which the annihilation occurs, while scatter and random coincidences introduce noise signals in the acquisition.

Scatter coincidences

Scatter coincidences occur when at least one of the two gamma rays produced in the same annihilation interacts through Compton scattering inside the body of the patient, the scanner frame, or the detector itself. In the first two cases, depending on the scattering angle θ, a noticeable amount of energy is transferred to an electron and lost before the gamma reaches the detector. The greater the deviation angle, the higher the

energy transfer. This generates a noise signal that can be reduced by accepting coincidence events with deposited energy above a certain threshold. However, in systems that are based on pixellated detectors, events where a gamma ray deposits its energy in two or more crystals are frequent and contribute up to 50% of the total amount of detected events. These events are called Inter-Crystal Scatter (ICS) events. The ability to correctly identify and solve the kinematics of these events would enhance the precision in the localization of the annihilation, without any loss in sensitivity. This aspect will be investigated in Chapter 8.

Random coincidences

Random coincidences happen if the two 511 keV gamma rays detected are not generated in the same annihilation event. This, once again, gives rise to noise signals and can be partly avoided by reducing the time coincidence window.

Signal-to-noise ratio and Sensitivity

All the false coincidence events, added to background noise in the reconstructed image, reduce the signal-to-noise ratio (SNR), contrast and resolution of the image. The SNR is a function of the count rate of true coincidence events R_{true} , random coincidence events R_{random} and scattered coincidence events $R_{scatter}$ as [27]

$$SNR \propto \sqrt{\frac{R_{true}^2}{R_{true} + R_{random} + R_{scatter}}} \tag{2.20}$$

Finally, the attenuation length in tissue (λ_{tissue}) is about 10 cm, and therefore a noticeable amount of gammas will be absorbed before reaching the detectors, lowering the event rate. This decreases the sensitivity of the PET scanner and worsens the reconstruction of the radiotracer distribution. The sensitivity of a PET system is defined as the number of detected true coincidence events normalized to the activity of the radiotracer. The true coincidence event rate R_{true}, and thus the sensitivity, depends on the gamma detector efficiency ($\eta_{detector}$), solid angle coverage of the detector (geometrical efficiency η_Ω) and gamma attenuation in the tissue (λ_{tissue})

$$R_{true} = R_0 \cdot \eta_{detector}^2 \cdot \eta_\Omega^2 \cdot e^{-\frac{D}{\lambda_{tissue}}} \tag{2.21}$$

where D is the thickness of the patient and R_0 the tracer activity. $\eta_{detector}$ and η_Ω are squared since the two 511 keV gamma have to be detected in coincidence in two detectors. This highlights the need for materials with a high gamma stopping power in order to keep $\eta_{detector}$ high. For this purpose, thick and dense crystals with high effective Z are used as will be discussed in Section 3.1.

2.1.6 Parallax error

If long and dense detectors are needed to maximize sensitivity, their section affects the spatial resolution and segmentation can be used to improve it (Figure 2.13).

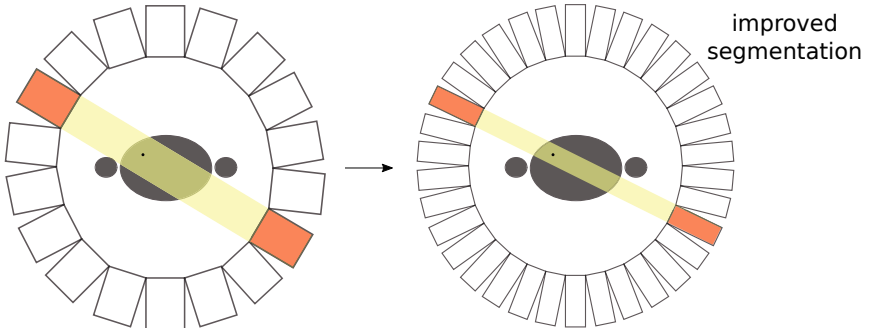

Figure 2.13: Crystal section affects the spatial resolution and the detector segmentation can be increased to improve it.

Spatial resolution

The spatial resolution of a PET scanner is given by the width of the Point Spread Function (PSF), which describes the response of an imaging system to a point source, defined in terms of FWHM. The contributions to the spatial resolution can be described as [28]

$$FWHM = 1.25\sqrt{(d/2)^2 + (0.0022D)^2 + r^2 + b^2 + p^2} \tag{2.22}$$

where d is the size of the detector, D the diameter of the scanner, which gives an estimation of the uncertainty due to the not perfect collinearity of the two annihilation gamma rays, and r the range of the positron, which puts a lower bound to the best possible spatial resolution. b and p account for the coding and parallax error. The first one is because of the association of more than one crystal to a single photodetector and therefore the position of interaction is obtained using an Anger logic scheme. This term also includes the possibility of ICS events. The resolution is measured in both the axial and transaxial directions because the geometry of the system causes different performances in different directions.

When a coincidence event takes place at the center of the field of view (FOV), the volume of response (VOR) size is solely determined by the cross-section of the crystals and the scanner diameter. If the coincidence event is located at the margin of the FOV, the size of the VOR is influenced by the crystal length as well (Figure 2.14). The VOR is defined as the volume in which every β^+ decay can cause an observation of two true coincident gamma events in a chosen detector pair. Coincidence events taking place off-centered do not travel parallel to the crystal axis and the VOR can be calculated by the projection of the whole crystal dimensions. Despite being useful in increasing sensitivity, long crystals cause an increase in parallax error.

A possible solution to overcome this difficulty is to include depth of interaction (DOI) information in the calculation of the VOR. DOI, defined as the position of the interaction of the gamma photon in the crystal along its main axis, helps to reduce the parallax error as it narrows the dimension of the projection of the crystal. Several techniques can be used to determine the DOI information.

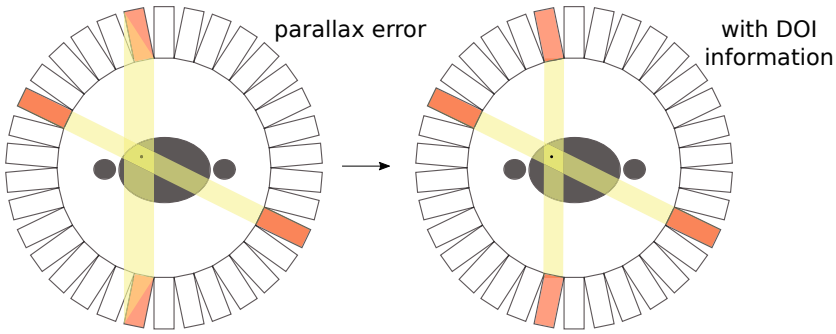

Figure 2.14: Left: Effect of parallax error. Right: Recovery of the detector response using the information on the DOI.

The extraction of the information on DOI plays an important role both in small animal PET detectors (where it helps to reduce parallax error), as well as in full-body TOF-PET scanners (in which it is fundamental to reduce the time jitter caused by the interaction of the primary gamma photon at different DOI). In the latter case, an improvement in time resolution is directly correlated to an increase in signal-to-noise ratio (SNR) in the reconstruction process, ultimately leading to better images of the region under study.

Different methods have been developed to extract the information on the DOI and will be described and investigated in Chapter 4.

2.2 History of PET

The first preliminary idea of PET was presented in 1951 by two separate reports by William H. Sweet [29] and Wrenn et at [30]. The following year, Brownell and Sweet built the first prototype of a brain PET scanner using two sodium iodide (NaI:Tl) crystals, each coupled to a photomultiplier tube (PMT), moving on a grid and connected to an ink plotter. They presented the results in a publication [31].

Dr. Brownell and his team at Massachusetts Hospital (MGH) in Boston developed the positron camera that became operational in 1969 [32]. It consists of two planar arrays of 127 NaI:Tl crystals read out by 72 PMTs. The patient is positioned between the two detectors. A unique feature of the design was a coding scheme that allowed small NaI:Tl crystals to be encoded by fewer, larger photomultipliers, thereby reducing cost and improving spatial resolution, using the well-established method of light sharing between photomultipliers introduced by Anger in the gamma camera [33].

After the announcement of the invention by Hounsfield of a method for x-ray computerized tomography [34], for which he shared the 1979 Nobel Prize in Physiology and Medicine with Cormack, the MGH positron camera was rotated to record multiple views, which were then filtered and back-projected to produce transaxial tomographic images [32].

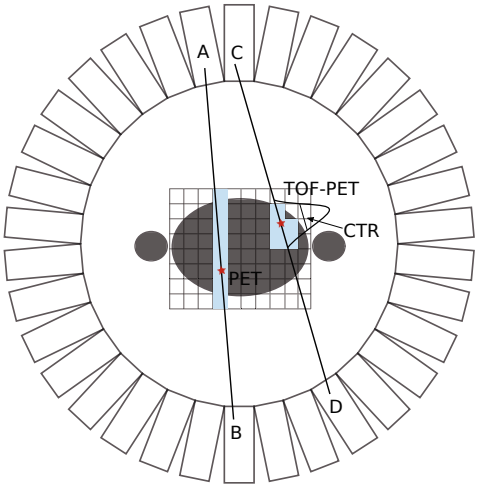

Figure 2.15: Time-of-flight information in PET constraints the positron emission region along the LOR.

In 1974, for the first time, the use of Bismuth Germanate (BGO) as a scintillating crystal was introduced. Throughout the 1980s and most of the 1990s, BGO was the main scintillator used in PET scanners. Finally, there was a switch from BGO to LSO, chosen for its excellent properties of high light yield and fast decay time, which later allowed the introduction of the "time-of-flight" PET.

2.3 Time-of-Flight PET

A major advantage of LSO, apart from the higher light output compared to BGO, leading to better spatial resolution, is the fast-timing that leads to lower detector dead-time and, above all, the capability to measure with enough precision the time difference between the arrivals of the two annihilation photons in the detectors, the "time-of-flight (TOF)".

In PET, image reconstruction is based on the determination of the LOR. Without TOF information, the position of the annihilation point is assigned with the same probability to all the points on the LOR inside the body of the patient. The information on the difference between the arrival time of the two gamma rays provided by the hit detectors can be used to determine the position, with reduced uncertainty, where the annihilation occurred along a LOR and improve the quality of a PET image. Knowing the time difference Δt, it is possible to obtain the coordinate s of the annihilation point with respect to the center of the LOR as [35]

$$s = \frac{\Delta t}{2} \cdot c \tag{2.23}$$

where c is the speed of light. In addition to the improved event localization along the LOR, the TOF information decreases noise correlation in overlapping LORs, improving SNR and image contrast. In Figure 2.15 the concept of time-of-flight in a single detector ring can be seen.

If, in addition, the time resolution of the detector was sufficient to determine the point of emission of every β^+ decay exactly, true 3D image reconstruction based on single events would be possible.

The image SNR gain of a TOF-PET system compared to a non-TOF-PET system can be expressed as [35]

$$G = \frac{SNR_{TOF}}{SNR_{non-TOF}} = \sqrt{\frac{2D}{c\,CTR}} \tag{2.24}$$

where D is the diameter of the imaged subject and CTR denotes the coincidence time resolution achieved by the system. Table 2.2 shows examples of the gain of a whole-body TOF-PET system compared to non-TOF. Assuming a patient diameter of 40 cm.

The goal to achieve CTR of 100 ps FWHM would correspond to 1.5 cm position resolution and an SNR gain of 5 or a PET sensitivity gain of about a factor 25 if compared to a non-TOF-PET system [27]. Thus, for constant image quality, a TOF-PET system with 100 ps CTR can result in a big reduction of the patient examination time or a lower radiation dose to the patient. It should be noted that the gain in SNR of a TOF-PET system compared to non-TOF rises with the patient diameter D (Equation 2.24). Hence, corpulent patients benefit the most from the TOF information in PET. The SNR for corpulent patients is normally worse because of a lower sensitivity due to gamma absorption in the tissue. Currently, commercial scanners achieve a CTR of around 200 ps FWHM. Specifically, the Siemens Biograph Vision and Biograph Vision.X achieve respectively 214 ps and 178 ps FWHM CTRs.

To further improve the CTR towards 100 ps, detailed studies and knowledge of the full detection chain are required. This is the intended purpose of this thesis work and will be presented in the following chapters.

Table 2.2: Coincidence time resolution (CTR), spatial resolution and SNR gain of a TOF-PET system compared to non-TOF for a patient diameter of 40 cm.

CTR	Spatial resolution	G
1 ns	15.0 cm	1.6
500 ps	7.5 cm	2.3
200 ps	3.0 cm	3.7
100 ps	1.5 cm	5.2
10 ps	0.15 cm	20

2.3.1 Why PET research at CERN?

The Crystal Clear Collaboration (CCC) [36] is an international collaboration created at the European Council for Nuclear Research (CERN) in 1990 with the initial aim of developing scintillating materials suitable for use at the Large Hadron Collider (LHC). The LHC project comprises a particle accelerator consisting of a 27 km ring of superconducting magnets with a number of accelerating structures and a huge system of detectors with state-of-the-art technology for four experiments to work in parallel.

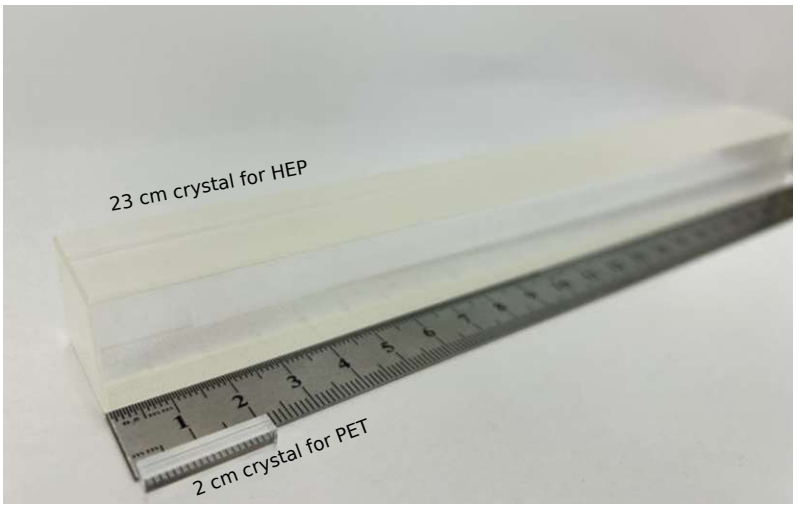

Figure 2.16: Comparison of the dimensions of a PWO crystal from the CMS electromagnetic calorimeter and a LYSO crystal used for PET applications.

Table 2.3: Comparison of the requirements for crystals for HEP and PET.

Requirements	HEP	PET
High density ($\geq$ 6 g/cm^3)	$\surd$	$\surd$
Fast light emission ($\leq$ 100 ns)	$\surd$	$\surd$
Light Yield	Moderate-High	High
Radiation hardness	High	Moderate
Fast and low-noise electronics	$\surd$	$\surd$
Compact integration design	$\surd$	$\surd$
Compact, high-gain photodetectors	$\surd$	$\surd$

The CCC set up an interdisciplinary network involving world experts in different aspects of material science and instrumentation for the detection of high-energy photons and electrons. Following the studies conducted by several groups within the CCC in the search for the most suitable scintillator for use at the LHC, Compact Muon Solenoid (CMS) and A Large Ion Collider Experiment (ALICE) collaborations decided in 1994 to choose a detector based on the use of lead tungstate ($PbWO_4$) scintillator for the electromagnetic calorimeter [37, 38]. Today, 75848 PWO crystals are installed in CMS and 17920 in ALICE.

In the same years, the CCC decided to apply and transfer its expertise on high-energy physics (HEP) to medical imaging, in particular to PET, due to the similarities of this field to electromagnetic calorimetry (Table 2.3). The Lutetium-Yttrium Oxy-orthoSilicate (LYSO) was studied, read out by Avalanche Photodiode (APD) and later Silicon Photomultiplier (SiPM), allowing much higher gain at lower biased voltage compared to PMT. Despite the similar technology employed in the two fields, the dimensions (crystal length of 2 mm for PET compared to 22 cm for HEP, see Figure 2.16) and energy scales (511 keV in PET compared to hundreds of GeV in HEP) involved are very different. This is the framework in which I conducted my PhD thesis work.

3 Radiation detector unit

The first step of a PET measurement is the detection of the two back-to-back gammas with energy around 511 keV. The common approach to detect such energetic photons is via scintillating crystals, that convert the incoming gamma into recoil electrons that, through excitation and ionization processes, generate visible light. The density and length of the scintillator are chosen to ensure the gamma photons are stopped efficiently. The visible photons are subsequently detected using a photodetector, e.g. a silicon photomultiplier (SiPM), an avalanche photodiode (APD) or a classical photomultiplier tube (PMT). They convert the photons into an electronic signal which is further treated by the readout electronics.

In this chapter, the three building blocks of the radiation detector, illustrated in Figure 3.1, are discussed. Section 3.1 explains the process of scintillation, while Section 3.2 focuses on the photodetection process, with particular attention to SiPMs. Finally, Section 3.3 describes the electronic readouts available for TOF-PET, highlighting their advantages and disadvantages.

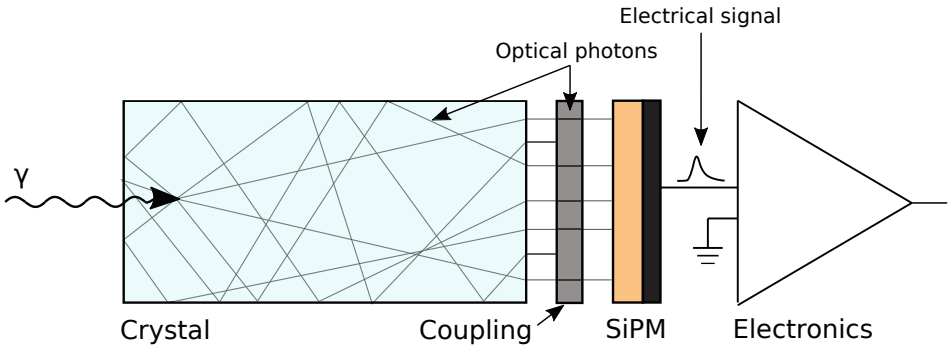

Figure 3.1: Schematic representation of the building blocks of a radiation detector: crystal, photodetector (SiPM), and electronics readout.

3.1 Gamma stopping materials

Following the gamma interaction mechanisms described in Section 2.1.3, the atoms of the material are ionized, i.e. electrons are freed from their bound state. The passage

of these charged particles through the crystal excites electrons. The number of these electrons is proportional to the energy lost by the incoming particle. The radiative de-excitation is called *scintillation*. The produced optical photons, in number proportional to the energy lost by the charged particle inside the bulk of the crystal, are collected by a photodetector. For PET applications, dense materials capable of stopping a high number of incoming gammas and producing light with fast scintillation are needed. In addition, even faster light production mechanisms, such as Cherenkov production, and a combination of dense and fast materials, in the so-called heterostructure concept, are being investigated.

3.1.1 Scintillators

Scintillating materials are usually divided into two families, organic and inorganic scintillators and they differ by the process in which energy is converted.

Organic scintillators

Organic scintillators consist of aromatic hydrocarbon compounds containing embedded benzene ring structures. These materials can be either plastic or liquid depending on their composition. In particular, plastic scintillators consist of a hosting polymer matrix, usually made of polystyrene, containing organic scintillating components. In organic scintillators transitions of free valence electrons that occupy molecular orbits lead to fluorescence. When an organic molecule absorbs energy, it rises to an excited state and returns to its fundamental state through the emission of visible light. This process has a typical time scale of a few nanoseconds. Plastic scintillators are widely employed due to their low production cost, versatility and tunability. They can achieve light outputs up to 10000 ph/MeV and decay times between hundreds of ps and a few ns. The typical density of these compounds is slightly above 1 g/cm^3 and their Z_{eff} is also low.

Inorganic scintillators

Inorganic scintillators are generally semiconductor or insulator crystals, and in such materials, the energy diagram is described in terms of conduction, valence, and core bands. The energy difference between the valence and conduction band is called energy bandgap and it constitutes a forbidden band i.e., electrons cannot occupy those states in a pure crystal. Scintillation in inorganic materials can be either intrinsic or extrinsic. Examples of intrinsic inorganic scintillators are BGO and PWO. Extrinsic scintillators, on the other hand, involve luminescent centres that are not intrinsic to the crystal lattice but are introduced through the addition of specific impurities, known as activators. This intentional doping of impurities leads to the creation of special allowed sites within the band structure of the material, with enhanced scintillation properties. This is the case for most inorganic scintillators, such as LSO:Ce, LSO:Ce:Ca, Gadolinium Aluminium Gallium Garnet crystals (GAGG) as GAGG:Ce, GAGG:Ce:Mg, NaI:Tl.

The scintillation mechanism in inorganic crystals can be described in four stages characterized by a different time constant [18, 39]. The first step is the multiplication

process. The hot electron-hole pair is subjected to electron-electron scattering and Auger processes in the material. In this way, further electron-hole pairs are created through inelastic scattering, until the energy of each electron and hole falls below the ionization threshold, i.e. twice the bandgap. This process usually takes between 0.1 and 10 fs. The second step is the thermalization. Once the energy of the charge carriers is below the ionization threshold, their thermalization via phonon scattering starts. This process is in the order of the picosecond. The third step is the transfer to luminescence centers. The thermalized charge carriers are transferred to the luminescence centers. The filling of luminescence centers takes between 1-100 ps. The last step is the recombination. Finally, the relaxation of the luminescence centers and recombination of the electron-hole pairs with the corresponding light emission can start. This process is characterized by time constants distributed in a wide time range, up to hundreds of nanoseconds, depending on the levels involved in the transition. The sum of the time needed for the thermalization of the charge carriers and filling of the luminescence centers defines the rise time of the scintillation pulse, and it is usually below 100 ps. The time needed for the recombination defines instead the decay time of the scintillation pulse, usually between 20 and 600 ns.

3.1.2 Cherenkov emission

Besides scintillation, a further light-generation mechanism commonly exploited in radiation detectors is the Cherenkov emission. Cherenkov radiation is the electromagnetic radiation emitted when a charged particle passes through a dielectric medium at a speed greater than the phase velocity of light in that medium

$$v > \frac{c}{n} \tag{3.1}$$

where c is the speed of light and n is the refractive index of the material.

Its cause is similar to that of a sonic boom, the sharp sound heard when faster-than-sound movement occurs. If hot electrons, produced upon 511 keV gamma interaction in the material, pass through the crystal at a speed greater than the phase velocity of light, they emit Cherenkov photons. The phenomenon is named after the physicist Pavel Cherenkov, who shared the 1958 Nobel Prize in Physics for its discovery with the colleagues Igor Tamm and Ilya Frank, for developing the theory of this effect [40]. When a charged particle moves inside a polarizable medium, it excites the molecules to the higher states. Upon returning to their ground state, the molecules re-emit photons in the form of electromagnetic radiation. According to the Huygens principle, the emitted waves move out spherically at the phase velocity of the medium. If the particle motion is slow, the radiated waves bunch up slightly in the direction of motion, but they do not cross. However, if the particle moves faster than the light speed, the emitted waves add up constructively leading to coherent radiation at angle θ_C with respect to the particle direction, known as Cherenkov radiation. The signature of the effect is a cone of emission in the direction of particle motion

$$cos(\theta_c) = \frac{1}{\beta n} \tag{3.2}$$

The emission of Cherenkov photons takes place in the early stages of the relaxation cascade (in the phase of electron scattering), providing a precise timestamp compared with scintillation photons. The emission is quasi instantaneous (< 10 ps) but few photons are emitted. The number of produced Cherenkov photons at a given wavelength is

$$\frac{d^2N}{d\lambda dx} = \frac{2\pi\alpha z^2}{\lambda^2}(1 - \frac{1}{\beta^2 n^2}) \tag{3.3}$$

being $\alpha = 1/137$, z the charge of the particle in units of e and λ the wavelength of the photon. This equation shows a dependence of the number of Cherenkov photons generated with $1/\lambda^2$, meaning that the light emission is mostly in the UV region. Comparing Cherenkov radiation with scintillation light two differences of crucial importance can be noted:

- the number of Cherenkov photons is, in general, much lower with respect to the number of photons produced in a scintillation process for the same amount of energy deposited.
- differently from scintillation being an isotropic process, the Cherenkov process is highly non-isotropic since the emitted photons are produced along a cone with an opening angle of θ_c around the axis of motion of the particle.

In high-energy physics, the measurement of Cherenkov helps particle identification and speed evaluation. Cherenkov counters have found applications in a variety of particle physics experiments in many different configurations. The Cherenkov photon yield decreases when approaching lower particle energies, as in prompt gamma imaging for range verification in hadron therapy [41] and in TOF-PET. Despite this, for the latter, the detection of few prompt photons in addition to scintillation can largely improve the timing performance [4].

3.1.3 Scintillators requirements

The ideal scintillating material should have high efficiency and linearity in the conversion of the kinetic energy of charged particles into detectable light (high light yield), high density and high linear attenuation coefficients at 511 keV to stop the gammas in the detector and measure accurately the deposited energy. Transparency to its emission and good optical coupling to the photodetector is necessary to maximize light collection. Finally, the decay time (defined as the time constant of the emitted light profile) should be fast to have a good time resolution and to correctly identify the coincidence events. The choice of the most appropriate scintillator for PET is based on a compromise among these different features.

Scintillation efficiency

The ratio of the energy of the produced scintillation light to the gamma ray energy can be calculated as

$$\eta_{scintillation} = \frac{E_{scintillation}}{E_\gamma} \tag{3.4}$$

For example, in the case of LSO, the emission peak is at a wavelength around 420 nm which corresponds to a transition energy of 2.95 eV and the absolute light yield of such scintillator materials is in the order of 40000 photons per MeV [37]. Therefore

$$\eta_{scintillation} = \frac{40000 \cdot 2.95\ eV}{1 \cdot 10^6\ eV} = 11.8\% \tag{3.5}$$

only a small fraction of the gamma ray energy is converted to scintillation photons. The scintillation efficiency describes how effectively the gamma ray energy can be converted to scintillation photons detectable by a photodetector.

Transmission and Absorbance

The light generated in a scintillator has to travel inside the material in order to reach the photodetector and produce a detectable signal. Passing through the medium, the emitted photons can be absorbed, or undergo Fresnel reflections and Rayleigh scattering. It is possible to quantify these effects by measuring the intensity I of light through the scintillator with a monochromatic beam of intensity I_0 and wavelength λ as

$$T(\lambda) = \frac{I(\lambda)}{I_0(\lambda)} \tag{3.6}$$

This quantity is defined as the transmission of the scintillator, and it is usually measured using a spectrophotometer providing a monochromatic beam of variable wavelength. Another quantity that combined with transmission offers insights into the photoluminescence centers in the material is the absorbance, computed as the logarithm of the ratio of incident to transmitted light intensity

$$A(\lambda) = -log_{10}T(\lambda) \tag{3.7}$$

Scintillation Kinetics

The time evolution of the scintillation intensity $f(t)$ is characterized by a fast dynamic in the first part of the process. Therefore, the intensity of emission $f(t)$ grows exponentially with one or more rise time constants $\tau_{rise,i} \sim 10^{-12}$-$10^{-11}$ s. The emission maximum is reached close to the moment when all the luminescence centers are filled. Then $f(t)$ decreases exponentially with behavior depending on the number of excited luminescence centers N_i for each component, their relative intensity R_i and their decay constants $\tau_{decay,i}$. A first-order formula to describe $f(t)$ is given by sums of bi-exponential functions as

$$f(t|t_0) = \Theta(t - t_0) \sum_{i=1}^{N} R_i \cdot \frac{e^{(t-t_0)/(\tau_{decay,i})} - e^{(t-t_0)/(\tau_{rise,i})}}{\tau_{decay,i} - \tau_{rise,i}} \tag{3.8}$$

a figure of merit that describes the de-excitation part of the scintillation kinetics is provided by the effective decay time $\tau_{decay,eff}$ defined as

$$\frac{1}{\tau_{decay,eff}} = \sum_{i=1}^{N} \frac{R_i}{\tau_{decay,i}} \tag{3.9}$$

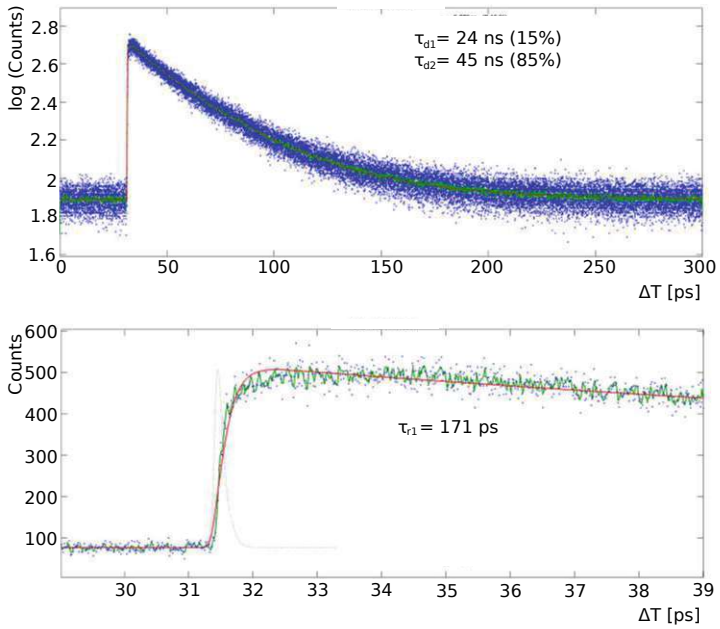

Figure 3.2: Time evolution of the scintillation intensity for LYSO:Ce. The effective decay time is 40 ns and the rise time is 171 ps. (top) The relative intensity of the decay constants and (bottom) zoom on the rising edge.

Figure 3.2 shows the time evolution of the scintillation intensity and the relative intensity of the decay constants for the case of LYSO:Ce. The effective decay time is 40 ns and the rise time is 171 ps.

Timing resolution

The timing resolution of a scintillator is the measurement of the precision to reconstruct the moment of interaction of an incident particle. A commonly used technique for the extraction of the timestamp is the **leading edge discrimination**, where the timestamp is determined as the moment when the signal generated by the scintillation pulse crosses a predefined amplitude threshold. Considering the properties described above, the detector time resolution (DTR) is proportional to [42]

$$DTR \propto \sqrt{\frac{\tau_d \cdot \tau_r}{N_{ph}}} \tag{3.10}$$

where N_{ph} is the number of detected photons that account for the scintillation efficiency and transmission and absorbance of the light produced, while τ_d and τ_r are the decay and rise times of the scintillation profile. In PET, the CTR defined as time resolution measured by two identical detectors in coincidence can be derived from the DTR as

$$CTR = \sqrt{2} \cdot DTR. \tag{3.11}$$

To achieve a good timing resolution, a scintillator should have both fast emission kinetics and high light output.

Table 3.1: Properties of the EJ-232 [43] and inorganic scintillators used in this work.

Name	Producer	Density [g/cm^3]	Emission peak [nm]	Light Yield [ph/keV]	Decay time [ns]	Refractive index
EJ-232	Eljen Technology	1.023	370	8.4	1.6 (100%)	1.58
LYSO:Ce,Ca[1]	Agile	7.4	420	39.2	33(94%) 8(6%)[4]	1.82
LYSO:Ce[1,2]	CPI	7.1	420	41.1	45(85%) 24(15%)[4]	1.82
BGO[3]	Epic Crystal	7.1	480	10.7	337(92%) 2(1%) 42(7%) [5]	2.15

[1] Data from [4] [2] CPI Datasheet [44] [3] Epic Crystal Datasheet [45] [4] Data from [46] [5] Data from [47]

The materials of interest that will be investigated in this thesis work are EJ-232, among the organic scintillators, and the fast LYSO and dense BGO, among the inorganic scintillators. The properties of these scintillators are summarised in Table 3.1.

- **EJ-232** is the commercial name of a plastic scintillator manufactured by Eljen Technology. It has a light yield of about 8000 photons/MeV. Its decay constant (1.6 ns) is one of the lowest of other materials with similar characteristics, making it particularly suitable for fast-timing applications.

- **LYSO** is a commercially available inorganic scintillating crystal of mixed composition that belongs to the family of rare earth oxyorthosilicates. LYSO requires cerium doping in order to activate its scintillation properties. It is characterized by a very high light yield ($\sim$ 40000 photons/MeV) and fast decay time ($\sim$ 40 ns). The ^{126}Lu isotope is radioactive (250 Bq/cm^3) and discourages any low background application but it is fortunately of low importance in PET applications, where the coincidence between detectors allows its suppression. The decay chain for lutetium-176 is shown in Figure 3.3. The mixed composite LYSO was developed to balance the best properties of LSO (high yield and high stopping power) and YSO (favorable growth and cost).

- **BGO** is an intrinsic inorganic scintillator made of bismuth, germanium and oxygen ($Bi_4Ge_3O_{12}$). The high density (7.13 g/cm^3) and large effective atomic number (Z = 83), despite the low light yield, make it of interest in terms of sensitivity. The light collection is made difficult by the high refractive index (n = 2.15) but it allows, on the other hand, the production of some prompt Cerenkov photons. Despite the low number of photons produced, Cherenkov emission could be exploited to improve time resolution. In fact, BGO is characterized by a slower decay time and lower light emission compared to LYSO.

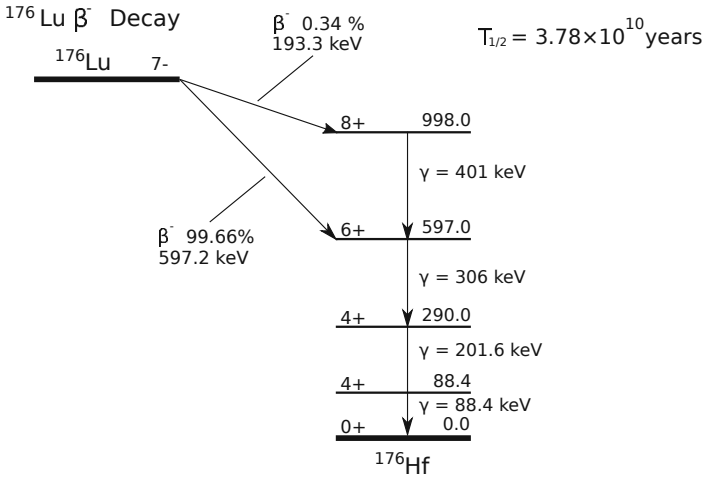

Figure 3.3: Decay scheme of ^{176}Lu, contained in LSO and LYSO, producing background radiation. Data from [17].

3.1.4 Heterostructures

Heterostructured scintillators involve the combination of two or more materials with distinct properties, strategically chosen to exploit the advantages of each component. In the specific context of TOF-PET, the two key properties that are not simultaneously found in a single material to the required extent are an efficient stopping power for gamma rays at 511 keV and a high photon density, i.e. the emission of a large number of photons in the first few nanoseconds.

The concept follows the one of sampling calorimeter in HEP, where two different materials are combined [48, 49]. In this approach, a dense, non-scintillating material (e.g. tungsten) is used solely to stop the incoming radiation and initiate the hadronic or electromagnetic shower. This material is then combined with a scintillating one, which provides the necessary properties for accurate energy measurement. The simplest way to combine different materials is by stacking alternating layers, as illustrated in Figure 3.4. Despite other configurations are also possible, the underlying principle of heterostructure is the same independently of the configuration used. It is called energy sharing [6] as it refers to the fact that the energy of the incoming radiation is deposited in both materials. This phenomenon becomes relevant when the thickness of the heavy material is comparable to the range of the recoil electron resulting from the photoelectric absorption of a 511 keV gamma in the material itself (a few hundred micrometers). Thus, the incident gamma can be stopped by the photoelectric effect in the heavier material, but there is a non-negligible probability that the photoelectron will escape from it to the faster material, where it will deposit the remaining energy. The events, for which energy sharing occurs, are called shared events. The more energy is deposited in the faster material, the faster photons are produced, improving the overall time resolution of the detector.

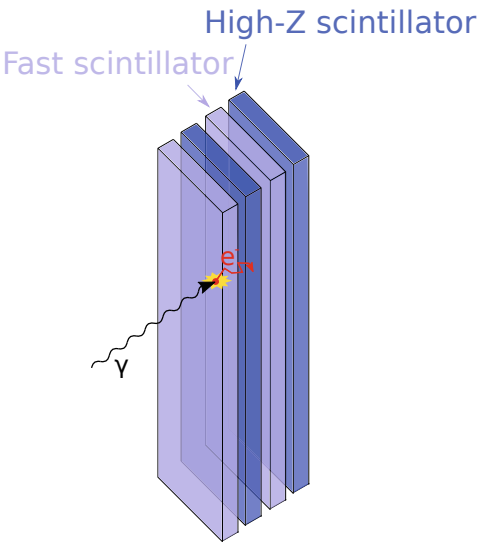

Figure 3.4: Concept of heterostructure and mechanism of energy sharing. The heavy material most likely stops the incoming gamma and the resulting recoil photoelectron can escape from it and travel into the fast-emitting material, depositing the remaining energy and producing fast photons.

3.2 Photodetector

The optical photons produced via scintillation or Cherenkov emission carry the information on the incident gamma ray. Therefore, they need to be collected and converted into a detectable and measurable electrical signal, preserving the original energy and timing information. The principle at the basis of a photodetector is the generation of free electrons or electron-hole pairs in a medium and their multiplication to generate a current signal with a measurable amplitude and charge. Because a minimum energy is necessary for ionization, photon detection is a threshold phenomenon, i.e. the photon energy $E_\gamma = \frac{hc}{\lambda}$ has to overcome a certain limit. Optical photon detection is carried out either by vacuum photodetectors or solid-state sensors, each exploiting its own technology. In vacuum photodetectors, optical photons are converted into electrons in an external photocathode by photoelectric interaction. These electrons are then accelerated in a high electric field and produce secondary electrons by interaction on the so-called multiplication stages. Examples of vacuum devices are the photomultiplier tube (PMT) and the microchannel plate (MCP). In solid-state photodetectors, electron-hole pairs are produced by internal photon interaction in a semiconductor. The produced electron-hole pairs are accelerated in the electric field and multiplied by impact ionization in the semiconductor itself. The avalanche photodiode (APD) and Geiger-mode APD (G-APD), which lead to the silicon photomultiplier (SiPM), are examples of this type of photodetectors. In this section, the working principle of the PMT and the SiPM will be described with a focus on the analog SiPM.

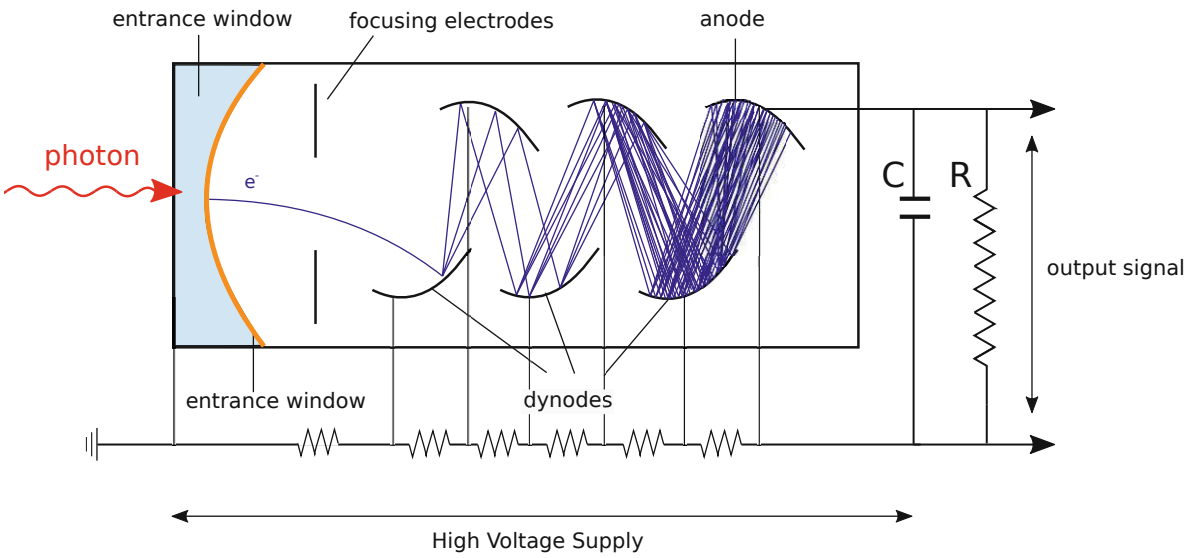

Figure 3.5: Schematic illustration of a PMT structure. Inspired by [25].

3.2.1 The photomultiplier tube

Photodetectors work in a proportional regime if there is a proportional relation between the incoming photon energy and the amount of charge collected. This is the case of the PMT, one of the most common photodetectors used to read the light emitted by a scintillating crystal and used in commercial PET scanners up to recent years when silicon-based photodetectors gained popularity. The photons generated in the crystals enter through a window which is usually made out of bialkali, or quartz, for good UV transparency. The entrance window is covered with a photosensitive compound, called photocathode, which releases an electron by photoemission when hit by a photon. The probability of emitting an electron per incident photon gives the quantum efficiency (QE), which is strongly dependent on the material and the incident photon wavelength. This is the highest disadvantage of PMTs as the photon detection efficiency is limited by the QE (20-40%). The electrons are then accelerated and focused onto the first dynode, where secondary emission frees other electrons that are then accelerated and focused on the second dynode and so on. The dynodes are biased with increasing voltage in order to create an accelerating electric field and finally collected at the anode where the current is read. This gives a signal that is well above the electronic background noise and can easily be detected with rather simple electronics. A big advantage of PMTs is their linear response from one initial photoelectron to several thousands. The main disadvantages of PMTs are the low efficiency of light collection and their sensitivity to electric and magnetic fields, high power consumption, and high transit time spread that degrades the time resolution of the pulse. A schematic illustration of a PMT structure is shown in Figure 3.5.

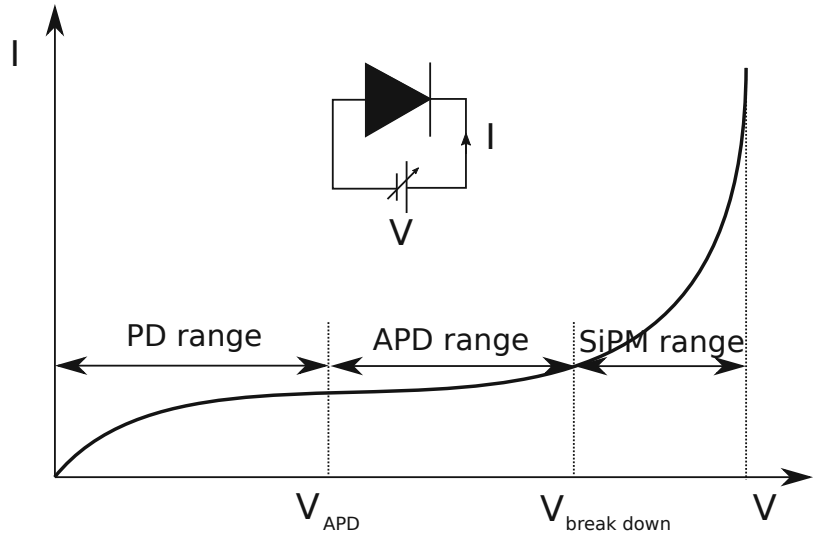

Figure 3.6: The three working regions of a p-n junction diode as a function of reverse bias voltage. The SiPM operates in the region above the breakdown voltage. Inspired by [25].

3.2.2 The silicon photomultiplier

If a p-n junction diode is biased reversely one can distinguish between three different regions depending on the reverse bias voltage applied. Figure 3.6 illustrates these three working regions. At low reverse bias voltages, when ionization produces electron-hole pairs in this volume, they are separated by the applied electric field without any other effects in the solid. The current remains low and it is proportional to the input light flux. The minimal detectable signal is in the range of several hundred (200-300) photoelectrons [50], i.e. produced electron-hole pairs. This is the working range of standard **photodiodes (PD)**.

If the reverse bias is increased, free electrons are accelerated and acquire sufficient kinetic energy to produce additional electron-hole pairs in the solid. In this process, the number of free carriers is amplified and avalanches formed. Because of the higher mobility and ionization coefficient of electrons in Silicon, only electrons contribute to the avalanche process. The multiplication process is linear, i.e. proportional to the initial produced photoelectrons, and the minimal detectable signal is in the order of several tens (10-20) photoelectrons [50]. This is the working range of the **avalanche photodiodes (APDs)**. To maintain the proportionality between the number of absorbed photons and the electron-hole pairs created, the photodiode can work below the break-down voltage (V_{APD}), but the main limitation is the lack of internal amplification.

If the reverse voltage is increased further above the so-called breakdown voltage (V_{BD}) the electric field becomes high enough to trigger a self-sustained avalanche in the p-n junction. Both electrons and holes contribute to the avalanche process. Each incoming photon is able to trigger such an avalanche and thus the device is able to de-

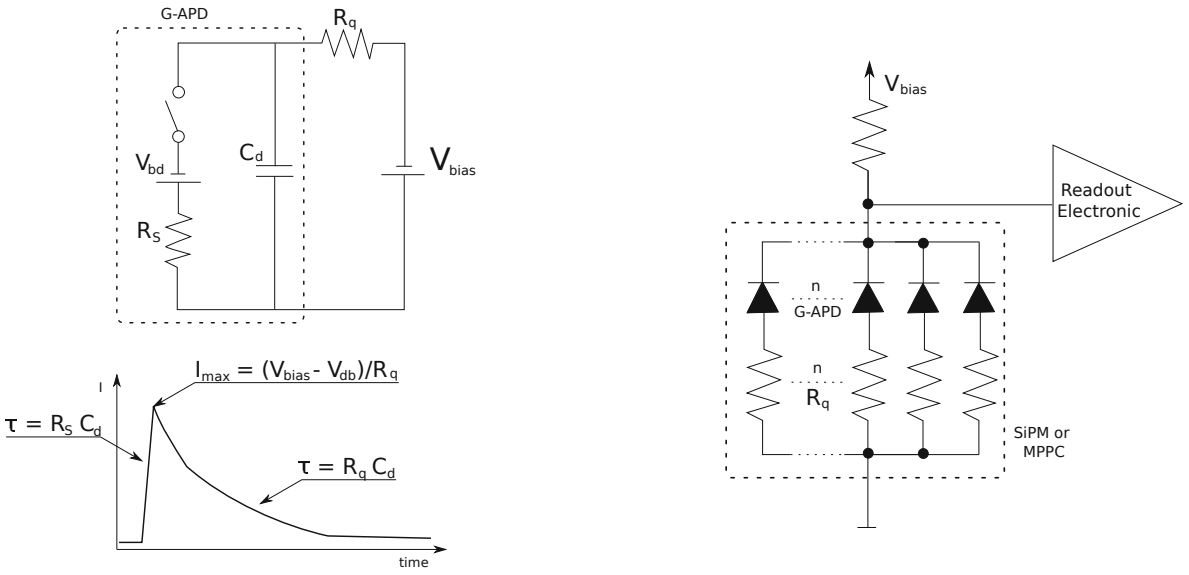

Figure 3.7: (left) Equivalent circuit of a G-APD and conceptual output pulse of the equivalent circuit [51]. (right) Schematic illustration of a SiPM structure. All microcells are connected together and readout in parallel. It should be noted that in a real device, parasitic capacitances and resistances complicate the equivalent circuit.

tect single photoelectrons, but the proportionality with the energy of the initial gamma is lost. The initiated avalanche has to be quenched externally either by a series resistor or by active quenching. This is the working regime of the **Geiger-mode APD (G-APD)**, since the charge collected is always the same and does not depend on the energy of the incoming photon and the detector works in Geiger mode.

A single device can not perform energy measurements, since the signal is saturated by the multiplication stage, independently of the number of incident optical photons. On the other hand, if a large amount of Geiger mode devices are grouped in a single photodetector, it is possible to employ it for spectroscopy. Several of such G-APD cells connected in parallel form the so-called **Silicon Photomultiplier (SiPM)** or multi-pixel photon counter (MPPC) and their constituents are single photon avalanche diodes (SPADs) G-APD (Figure 3.7 left). In Figure 3.7 on the right, the schematics of the parallel connected SPADs with serial quenching resistors R_q (passive quenching) as well as external biasing and analog readout of the summed cell signals are shown. If an avalanche occurs in the microcell a current will start to flow provoking a voltage drop on the serial quenching resistor R_q. With a progressing avalanche, the voltage drop on R_q increases until the point when the operational voltage of the SPAD is below the breakdown voltage, provoking the stop of the avalanche.

Properties of the silicon photomultipliers

The SiPMs produce always the same output signal, no matter how many photons initially triggered the avalanche. The gain (G) can be expressed as

$$G = \frac{C \cdot V_{OV}}{q} \tag{3.12}$$

being C is the cell capacitance, V_{OV} the bias overvoltage, which is the operating reverse bias voltage minus the breakdown voltage, and q the elementary charge equal to $1.602 \cdot 10^{-19}$C. Typical values for G are in the order of 10^5-10^7 and are enough to produce a single photon signal above the electronic noise.

The noise introduced by the SiPM can be uncorrelated and correlated. Uncorrelated noise is due to dark counts, the random appearance of electron-hole pairs in the depletion zone that triggers a breakdown, caused by temperature and operating voltage. These two components can be reduced by decreasing respectively the temperature and the bias voltage. Correlated noise is due to optical cross-talk and afterpulsing. Internal cross-talk is the triggering of a neighboring cell during the discharge of one cell due to a secondary photon produced which causes a secondary avalanche in another SPAD. External cross-talk happens if the secondary photon produced by the avalanching microcell exits the surface of the SiPM and is reflected back to it. This becomes likely in systems where the SiPM is coupled to a crystal that can act as a reflector. Afterpulsing happens when carriers are trapped and released after the discharge, causing a second, less intense, discharge with a delay of up to several nanoseconds.

The time after a breakdown has been quenched until the microcell is charged and ready for the next firing is characterized by the recovery time. The time constant τ is mostly dependent on the quenching resistor R_q and the cell capacitance C, i.e. $\tau = R_q \cdot C$. For instance, Hamamatsu has a quenching resistor of about 150 kΩ for 50 μm SPADs and a cell capacitance of about 100 fF. The recovery time is several tens of nanoseconds [51]. Because the used quenching resistor value is strongly dependent on the temperature the recovery time is a function of temperature as well.

The photon detection efficiency (PDE) is another important parameter of a SiPM, which is the probability that a single photon triggers a SPAD to produce a pulse. It is the product of three quantities

$$PDE = QE \cdot \epsilon \cdot P_{trigger} \tag{3.13}$$

where QE is the quantum efficiency that can reach values up to 90% for the active area, ϵ the fill factor, defined as the ratio between the photosensitive area and the total surface of the SiPM, and $P_{trigger}$ the probability of an electron-hole pair to trigger an avalanche, which increases with increasing bias voltage. PDE for modern SiPMs reaches values up to 60%, compared to the efficiency of light collection of PMTs (20-40%).

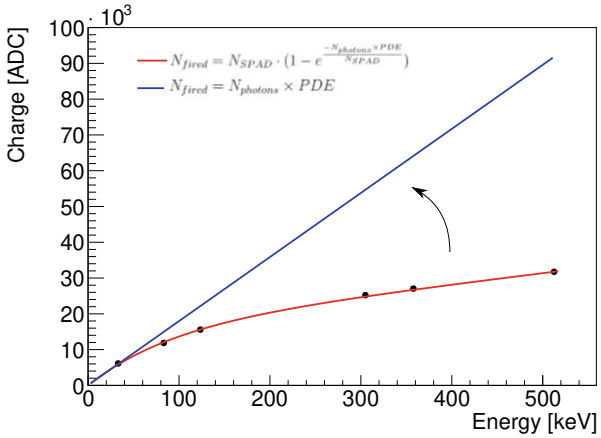

Figure 3.8: SiPM saturation effect, due to the limited number of SPADs, evaluated using different radioactive sources. The ideal linear response is shown for comparison.

If the number of photons ($N_{photons}$) times the PDE is small compared to the number of microcells (N_{SPAD}), the SiPM output signal (N_{fired}) is proportional to $N_{photons}$. If the input photon flux increases, the SiPM shows saturation due to the limited availability of SPADs to detect succeeding photons while a portion of the SPADs population is recovering from the detection of preceding photons. The response of the SiPM is

$$N_{fired} = N_{SPAD} \cdot (1 - e^{\frac{-N_{photons} \times PDE}{N_{SPAD}}}) \tag{3.14}$$

if the width of the incident light pulse (PW) is smaller than the recovery time. If PW is longer than the recovery time, the number of available SPADs is no longer N_{SPAD}, but $N_{SPAD} \times \frac{PW}{t_{recovery}}$. To evaluate the saturation effect, and correct for it, the measured integrated charge for each SiPM is evaluated for the photopeaks corresponding to the gamma emissions of radioactive sources of different energies, such as ^{22}Na, ^{137}Cs, ^{57}Co, ^{60}Co and also ^{176}Lu contained in the LYSO crystal (Figure 3.8).

Recent advances in the development of semiconductor photomultipliers have led to the substitution of PMT with solid-state photodetectors in PET because of several advantages: photon detection efficiency, lower power consumption, insensitivity to magnetic fields, compactness and potential cheapness. The reduced space in which charges move translates in a lower time spread. The QE in solid state devices is defined as the probability of generating an electron-hole pair per incident photo and it is much higher when compared to the values reached with the best photocathodes used in PMTs. This leads to a higher photon detection efficiency and thus to a potentially better energy and time resolution if used in scintillator based gamma detectors. Additionally, in a combined PET-MR scanner magnetic fields higher than 1 T is used and therefore PMTs would be not operational as well. However, a major disadvantage of SiPMs is the saturation behavior and nonlinearity of the energy response, as described above.

The main properties of the SiPM arrays of interest for this thesis work are summaries in Table 3.2.

Table 3.2: Properties of the SiPM arrays of interest for this work from Broadcom and Hamamatsu [51, 52].

Name	Producer	N_{ch}	N_{SPAD} /ch	A_{active} /ch [mm]	SPAD size [μm]	V_{BD} [V]	V_{OV} [V]	PDE [%]
S13361-3 050AE-04	HPK	16	3584	3x3	50	53	6	40 @450nm
AFBR-S4 N33C013	BCM	16	9815	3x3	30	32	10	43 @420nm
AFBR-S4 N44P014M	BCM	16	8334	3.72x3.62	40	32	16	63 @420nm

3.3 Electronics

Photomultiplier tubes are often used because of their built-in signal amplification mechanism and therefore larger electrical pulses. In many detector types, such as SiPMs, there is no such built-in amplification mechanism, and it needs to be added by means of front-end electronic boards. Two modes are usually employed to measure the detector signals: *current mode* and *pulse mode*. The current mode allows the simple measurement of the total current of the detector, ignoring the pulse number and nature of the signal. The *pulse mode* is used to count the individual pulses generated by the particles and extract the timing and amplitude (or integral) information that is present in the signal, as required in PET. The main challenge is distinguishing the small signals from the noise, i.e. any random signal that is not due to the physical process one intends to measure. Therefore, low noise and fast electronics are needed to readout the small signals generated by the SiPM.

An extensive part of this thesis work has been dedicated to the evaluation of different readout electronics dedicated to PET, in particular of the ultrafast front-end discriminator amplifier NINO [53] developed at CERN, the PETsys TOFPET2 ASIC developed by PETsys Electronics SA [54] and a Low-Noise Low-Power High-Frequency board developed at the Lawrence Berkeley National Laboratory [55]. The advantages and disadvantages of each electronic readout are described.

3.3.1 NINO 32-chip board

NINO is an ultrafast front-end amplifier and discriminator, originally developed for TOF particle discrimination in the ALICE experiment [53]. The version of the NINO chip used is made of 32 channels, each able to process the signal in differential form, from input to output. Each NINO channel is made of an input stage, followed by

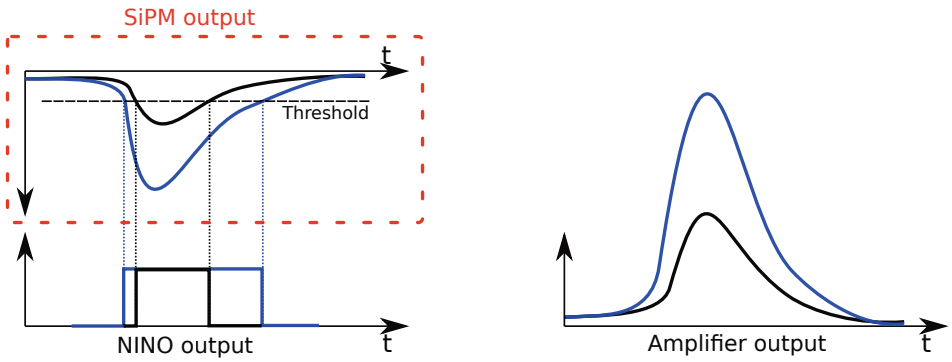

Figure 3.9: The signal from each of these channels is split in two: the first is fed to a NINO chip, the second one is amplified. The output pulse of the NINO chip (left) and of the amplifier (right) are illustrated.

four amplifiers and an output driver which adapt the output signal to the low-voltage differential signaling (LVDS) standard. The cascade amplifiers, producing a factor 6 gain, allow using NINO as a discriminator. The output is a square pulse that carries both time and energy information: the leading edge provides a time stamp correlated to the input pulse (leading edge discrimination) and the pulse duration is correlated to the Time Over Threshold (TOT), therefore carrying information regarding the input pulse charge.

For our applications, both the information on the charge and timing are necessary, with the best possible resolutions. This is achieved by developing a custom Front End Board (FEB) that splits the signal from each SiPM array channel into two, and by setting up two parallel chains for the signal processing, one for the energy and one for the time measurement (Figure 3.9).

The FEB is designed [5] to host up to two SiPM arrays, each with up to 16 channels, via Samtec SS4-20 connectors. The signal from each of these channels is split in two: the first is fed to a NINO chip and the other is amplified. The output of the board is therefore a number 2N of signals, N being the number of SiPM channels, plus a sum signal which is the sum of all the charge signals. This last signal is fundamental for trigger purposes for the subsequent acquisition and digitalization chain as will be explained later on. The board is connected to multiple power supplies, necessary to bias the SiPMs, to power the NINO chip and the amplifiers.

A picture of the FEB is shown in Figure 3.10: on the left, perpendicular to the board, the NINO chip is visible and on the right we can see the 32 amplifiers (one for each SiPM channel) as well as the connector for the flat cable used to carry the charge signal. The LEMO connectors are used for biasing purposes and for the sum signal output.

3.3.2 PETsys TOFPET2 ASIC

The TOFPET ASIC series is developed by PETsys Electronics S.A., Oeiras, Portugal to read out SiPM-based detectors in medical and HEP applications. It was initially developed in the framework of the ENDOTOFPET-US project [54]. The TOFPET2 ASIC

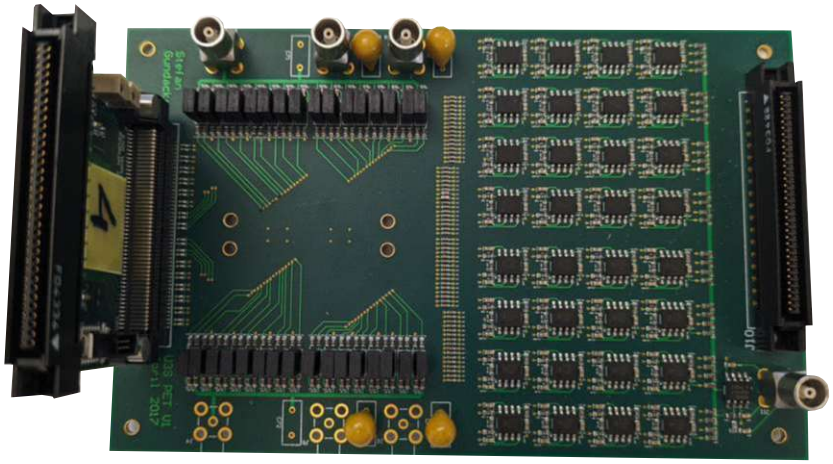

Figure 3.10: Picture of one of the two custom FEBs developed using the NINO 32-chip. On the right, the array of 32 amplifiers, on the left, a NINO 32-chip plugged into the board. The two Samtech connectors are placed on the rear side of the board (not visible in this picture).

(version b) that will be described was released in 2017. It is commercially available. Ready-to-use evaluation kits include a custom sensor front-end board (FEB/S) and an adapter board to connect the SiPMs, plus two FEB/A_v2 boards each with one 64-channel High-Performance TOFPET2 ASIC and an interface front-end board (FEB/I) connecting the ASICs to the motherboard (FEB/D_v2) via Samtec high-speed coaxial (HQCD) cables. This is called the standard Front-End-Module (FEM-128) (Figure 3.11). Two FEM-128 are used to read out two detectors in coincidence.

Each TOFPET2 ASIC is characterized by compactness, the possibility to read out 64 channels, maximum power consumption of 8.2 mW per channel, and its high capacity of data rates of up to 600 kcps per channel. Each channel, which is divided into two branches, employs a three-threshold trigger logic with two discriminators D_{T1} and D_{T2} in the timing and one discriminator D_E in the energy branch [54, 56, 57].

The trigger circuit of each channel enables dark count rejection and high timing resolution by triggering at a low threshold with the first discriminator D_{T1}, in other words, on the first optical photons hitting the SiPM. This trigger enters an AND gate opened by a second trigger activated at a higher threshold by a second discriminator D_{T2}. In the second branch, a third discriminator D_E operates at an even higher LSB scale, generating the trigger used to validate the signal. Per default configuration, a signal is only considered valid after triggering all three discriminators of the circuit. The thresholds of the three discriminators can be adjusted via the three dimensionless parameters vth_t1, vth_t2, and vth_e in the ASIC configuration.

A time-to-digital converter (TDC) assigns a timestamp to an event, and the energy of the respective event can then be measured either by signal integration featuring capacitors (qdc-method, determining the energy via signal integration over a period of 290 ns) or by measuring the time over a specified threshold (tot-method). The charge-to-digital converter (QDC) is used in qdc mode for the aim of this work. After

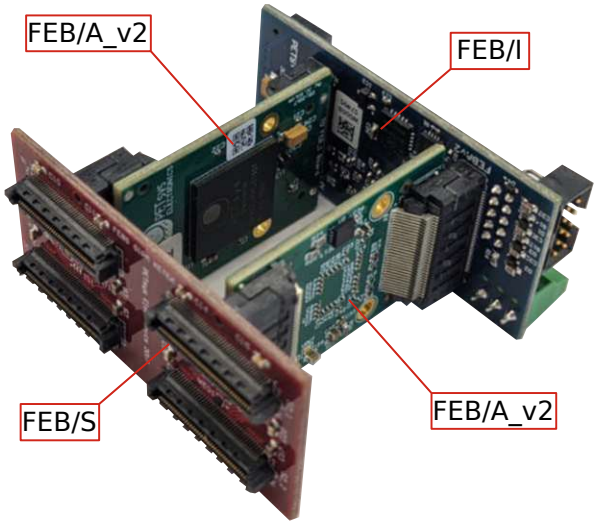

Figure 3.11: Picture of the standard Front-End-Module (FEM-128), made up of one interface board FEB/I, two FEB/A_v2 boards (each with one 64-ch High Performance TOFPET2 ASIC) and one FEB/S board able to host two 8x8 SiPM arrays, making a set of 128 readable SiPM channels. Up to eight PETsys Front-End Modules can be connected to one FEB/D board either directly, or using an HQCD series cable from SAMTEC.

calibrating the channel baselines, the TDCs, and QDCs, using the calibration routine provided with the evaluation kit software, measurememts can be performed.

Using the convert_raw_to_singles_method implemented by PETsys Electronics S.A. [57], acquired raw data are converted to single hit information, each with a timestamp, energy value, and channel-ID.

3.3.3 High Frequency readout

High-frequency (HF) electronics emerged among the readout technologies for analog PET detectors. Owing to their excellent performance, they revealed the timing limitations in TOF-PET due to scintillator material and SiPM technology. First, prototypes with one channel were proposed, while nowadays multi-channel versions are under study and development.

In the first proposal of Cates et al. [58, 7], a passive compensation circuit as a modified version of that outlined in [59] is used where a balun transformer (Macom MABA-007159) is connected between the cathode and anode of the SiPM in a balanced-to-unbalanced configuration to two Minicircuits MAR-6 RF amplifiers in cascade, as shown in the circuit schematic and the printed board in Figure 3.12.

Following up, efforts were made to reduce the power consumption of the circuit [60], where the new circuit design (Figure 3.13) included an ATB-2012 micro-balun

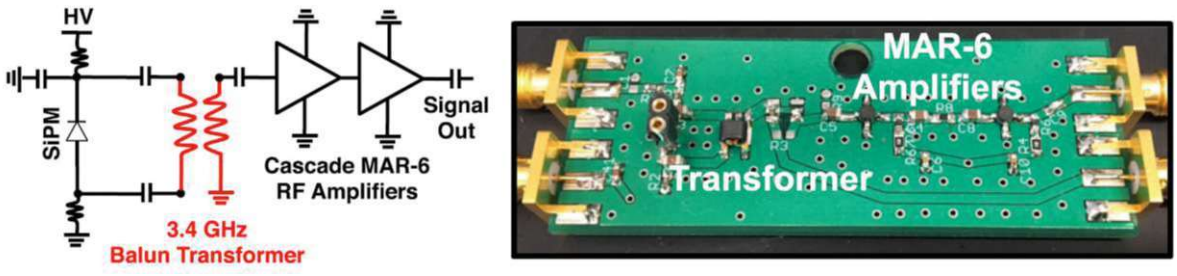

Figure 3.12: Schematic of the high-frequency (HF) circuit introduced by Cates et al. with the use of passive capacitance compensation and example of the circuit assembled. Image taken from [7].

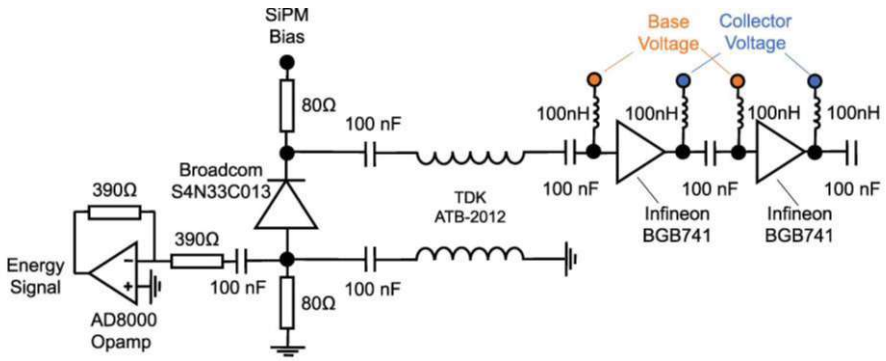

Figure 3.13: Schematic of the HF circuit implemented by Cates et al. making use of an ATB-2012 micro-balun transformer, two BGB671 amplifiers by Infineon, and an AD8000 operational amplifier to enable energy qualification. Image taken from [60].

transformer, two BGB671 amplifiers by Infineon and the operational amplifier AD8000 from Analog Devices as anode buffer to enable energy qualification as introduced by Gundacker et al. [61], where the anode signal is split into two signal branches to allow for the separate shaping of an energy signal using the non-inverting operational amplifier AD8000 supplied with 6 V.

Low-power low-noise high-frequency 16-channel development board

In order to test detector prototypes consisting of multiple channels, a custom, sixteen-channel electronics readout board employing a modified version of the low noise, high frequency (LNHF) signal processing chain described in [7] is developed by J. Cates at the Lawrence Berkeley National Laboratory, Berkeley, California, USA (Figure 3.14) from the one described in [55]. In addition to the components previously described, each analog timing branch is processed by a fast discriminator to extract a fast digital signal. Moreover, global energy output is extracted as the sum of all the deposited energies and it is used for triggering the acquisition system.

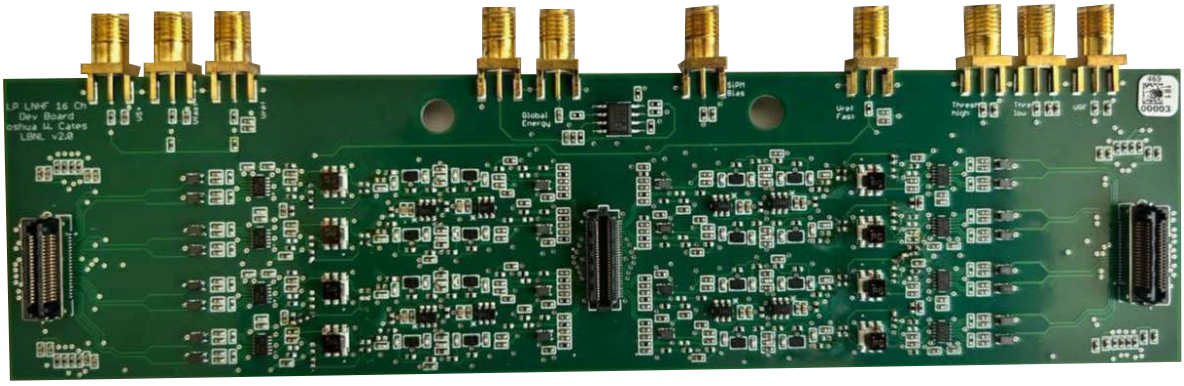

Figure 3.14: Low-power low-noise high-frequency (LPLNHF) sixteen-channel development board implemented by J. Cates at the Lawrence Berkeley National Laboratory.

II

Performance evaluation of a PET module prototype with DOI and TOF capabilities using different electronics

4 TOF and DOI performance of a LYSO:Ce PET module using a custom-made NINO 32-chip board

The basic PET detection module is made of several scintillators that convert the energy of the incoming gamma into optical photons, detected by SiPMs that convert the scintillation light into an electrical signal. As presented in Section 3.1.1, one of the most suitable scintillators for PET applications is LYSO:Ce, owing to its high photon yield of 40000 ph/MeV, high density (7.4 g/cm^2), and fast scintillation profile ($\tau_{decay,eff}$ = 40 ns) [46]. The need for high sensitivity imposes the use of long scintillators, which can give rise to distortions in the reconstructed images due to parallax effects. Moreover, as the frontier of timing is more and more pushed towards the goal of 10 ps FWHM CTR [3, 62], the influence of light transport on the CTR, and its dependence on the gamma-rays' DOI position along the main crystal axis, becomes no longer negligible [63, 64, 65].

The evaluation of the depth of interaction (DOI) of gamma rays along the main axis of the scintillator is fundamental to avoiding parallax errors in the image reconstruction process and achieving high spatial and timing resolution. This is of particular importance for preclinical and organ-dedicated human PET scanners that require very

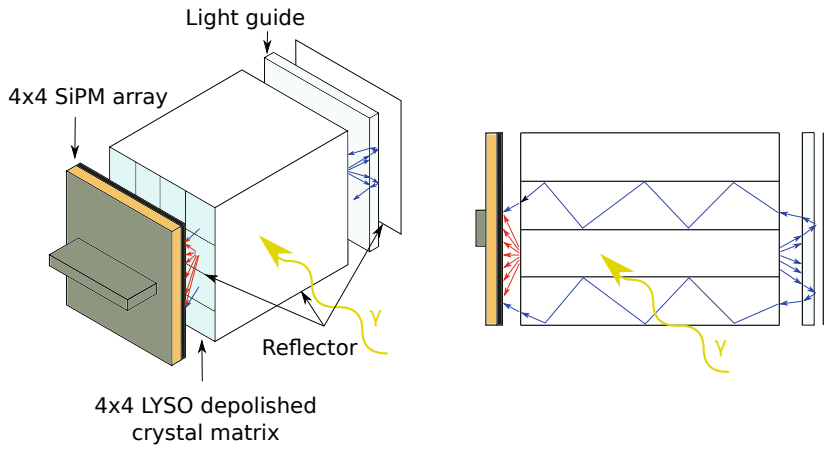

Figure 4.1: Schematic of the DOI capable module.

high spatial resolution, of the order of 1–2 mm, and that suffer from a large influence of parallax errors, because of their geometry and position to achieve a high solid angle coverage. There is a very high probability of an oblique angle of incidence in these scanners.

A method to effectively extract the DOI information is the use of an array of scintillators, laterally depolished and coupled on one side to a 4x4 matrix of photodetectors and on the other side to a light guide covered with a specular reflector [66] (Figure 4.1). The DOI coordinate can then be derived from the ratio of light detected by the SiPM directly coupled to the scintillator and the total light collected by all the SiPMs, and as such can be used to correct the timing evaluation [5].

This chapter presents the described DOI approach using LYSO:Ce and a custom-made 32-channel board based on the NINO chip [5]. In Section 4.1, an overview of the detector chain is presented, which includes scintillators, photodetectors, two identical electronic boards based on the NINO chip to read out the signals from the detectors, and the acquisition set-ups used to conduct the measurements. Section 4.2 describes the characterization methods in terms of timing, energy and DOI resolutions. Finally, Section 4.3 outlines the results obtained, followed by the discussion of the results (Section 4.4) and drawn conclusions (Section 4.5).

4.1 Materials

Two different configurations of PET modules, illustrated in Figure 4.2, are investigated for this study: the former, analogous to the ones employed in the modern PET scanners, composed of fully polished scintillators lacking DOI extraction capability (standard module), the latter, exploiting surface depolishing of the crystals and light recirculation within the module, capable of retrieving the DOI information (DOI-capable module). Both modules consist of 16 crystals of LYSO:Ce scintillators produced by CPI and an array of 4x4 SiPMs. In particular, a S13361-3050AE-04 SiPM array from Hamamatsu, an array of 16 NUV-HD SiPMs and the 4×4 NUV-MT SiPM array from Broadcom.

4.1.1 Standard detector module

The standard module is made of 16 LYSO:Ce crystals, each measuring 3.1×3.1×15 mm^3. Each crystal is fully polished and coupled *one by one* to a single detector of the SiPM array and separated from its neighbors by foils of reflective material (enhanced specular reflector (ESR)). Finally, a foil of ESR is placed in dry contact on the side of the matrix opposite to the photodetectors to act as a mirror.

On the one hand, as light sharing and attenuation are extremely low within the module, no DOI capabilities are expected for such a configuration. On the other hand, the reduced path traveled by the optical photons to reach the SiPM array yields the best results in terms of timing and energy resolution [5].

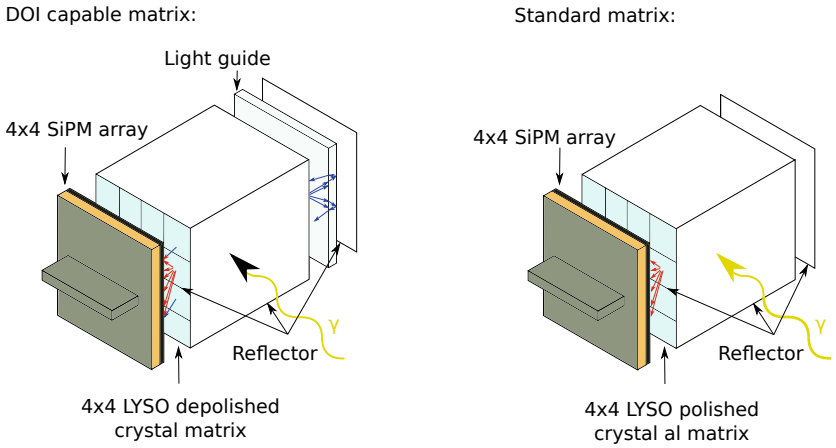

Figure 4.2: Structure of DOI modules (left) and standard modules (right). The two structures differ only in the presence of a light guide, and the depolished surface finishing in the DOI modules.

4.1.2 TOF and DOI capable detector module

The structure of the DOI-capable module is very similar to that of the standard module. The only differences are the use of scintillators with the lateral surfaces depolished, thus attenuating the light based on the depth of interaction, and the presence of a light guide made of glass between the crystal matrix and the reflective foil, as shown in Figure 4.2. The light guide is coupled to the side of the scintillator block opposite to the photodetectors using optical clear adhesive (OCA) of 150 µm, enabling light re-circulation inside the crystal matrix.

Thanks to this light re-circulation scheme, a certain number K of photo-detectors is hit by the photons generated by the scintillation event. We denote these photo-detectors as $i = 1, 2, ..., K$. For each detector D_i, the amount of light collected by the photodetector is denoted as p_i, and the measured time of detection as t_i. When a gamma ray interacts at a given DOI of a pixel in the scintillator array (identified as $i = 1$), the light produced propagates in the crystal and, eventually, is emitted both from the *photodetector-side* (red arrows in Figure 4.2) and the opposite end *reflector-side* (blue arrows in Figure 4.2). For each scintillation event, this photodetector D_1 can easily be identified as it is expected to measure the maximum amount of light $p_1 = p_{max}$. Because of the optical depolishing of the lateral surfaces of the crystal, the ratio of the amount of light emitted from the two ends of the scintillator determines the gamma interaction point w along the crystal axis [67, 68]

$$w = \frac{p_{max}}{P} \text{ , with } P = \sum_{i=1}^{K} p_i \tag{4.1}$$

P denotes the total amount of light collected by the K photodetectors. Moreover, the

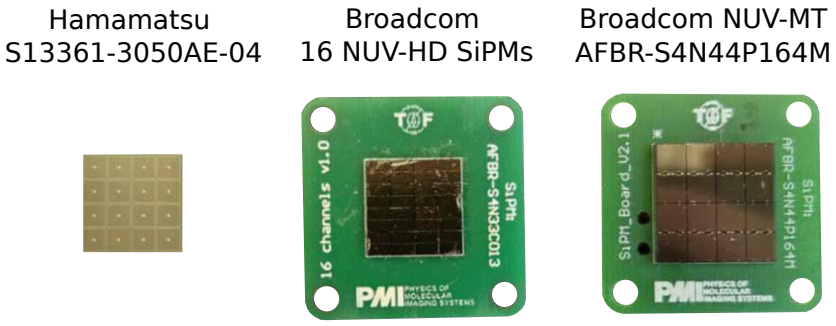

Figure 4.3: Picture of the three types of SiPM arrays used for this study: Hamamatsu model S13361-3050AE-04, 16 NUV-HD SiPMs and the high-performance NUV-MT (metal in trench) SiPM array from Broadcom.

quantities

$$u = \frac{1}{P}\sum_{k=1}^{K} p_k x_k \ , \quad v = \frac{1}{P}\sum_{i=k}^{K} p_k y_k \tag{4.2}$$

allow for the correct identification of the crystal where the gamma interaction occurred.

4.1.3 SiPM arrays

Different SiPM arrays are used for this study and are illustrated in Figure 4.3:

- *Hamamatsu model S13361-3050AE-04.* Consists of an array of 4x4 SiPMs, each with 3x3 mm^2 active area and 50 μm spad pitch, matching the dimensions of the crystals of the module.
- *16 Broadcom NUV-HD SiPMs.* An array of 16 SiPMs with 3x3 mm^2 active area and 30 μm spad pitch is assembled to match the same dimensions of the crystal matrix.
- *Broadcom NUV-MT AFBR-S4N44P164M.* Based on the new metal in trench (MT) technology from Broadcom and Fondazione Bruno Kessler (FBK) [69], it has a total dimension of 16x16 mm^2. It is made of SiPMs each with a sensitive area of 3.72x3.62 mm^2 and 40 μm spad pitch, therefore there is no one-to-one coupling with the crystal array.

The crystal modules are coupled via OCA of 50 μm to the Hamamatsu 13361-3050AE-04 array and via Cargille Meltmount (refractive index n = 1.582) to the Broadcom arrays. The crystal modules and SiPM arrays are all commercially available.

4.1.4 Multi-channel NINO32-chip based board

An accurate evaluation of the amount of light hitting each photodetector is required to be able to extract information on the energy deposited by the gamma ray in a crystal. This can be achieved by integrating the electrical pulses generated by each photodetector when hit by the scintillation light. At the same time, evaluating the timing and

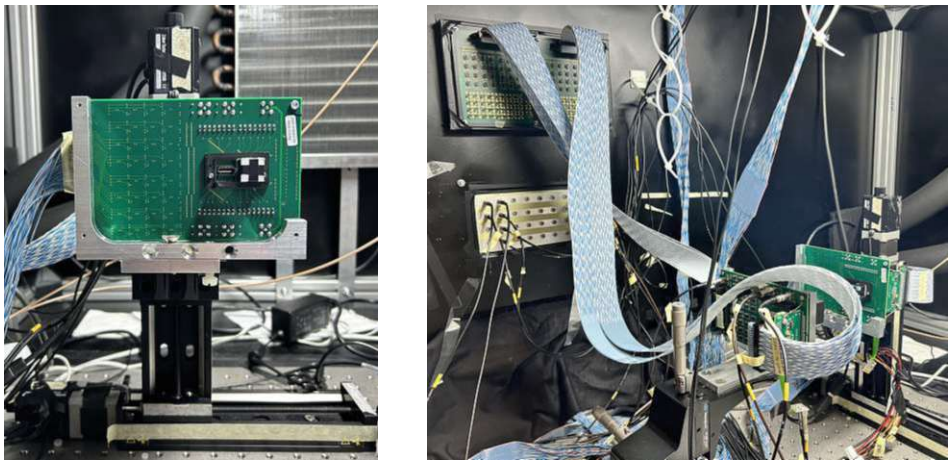

Figure 4.4: Picture of the experimental set-up. (left) Close-up picture of the FEB connected to a DOI-capable detector module using the Hamamatsu array and mounted on two automatic linear stages from Zaber. (right) Coincidence between reference detector and detector module. The FEBs, the modules, the radioactive source and the stages are placed inside a temperature-monitored light-tight box. On the left side, patch panels, mezzanines, and holes connect the electronics with the external section of the acquisition system.

applying corrections using the DOI information require parallel multichannel readout with fast electronics. This is achieved by the NINO 32-chip FEB board presented in Section 3.3.1, which allows the extraction, for each SiPM of an array, of an analog signal carrying the information on the deposited energy and a digital signal with the information on the time of collection of the light produced in the crystal.

4.1.5 Measurements set-up

Two FEB modules are used to perform coincidence measurements between two detectors placed at opposite sides of a ^{22}Na source, with 2 MBq activity. One FEB is used to read out the detector modules described above, while the other FEB module reads out a reference detector consisting of a LYSO:Ce:Ca crystal with dimensions 1.7x1.7x3 mm^3 and coupled to a Hamamatsu S13360-3050-CS.

Mechanical set-up

The FEB module connected to the reference detector is mounted on two manual stages, while the detector array is mounted on two automatic linear stages from Zaber (model T-LRS150B) to allow movements in the two directions of the plane perpendicular to the axis described by the reference crystal and sodium source. A picture is shown in Figure 4.4. The stages are connected to the computer used to run the acquisition and controlled by the main readout software, using secondary Python scripts that automatically change the positioning during multiple data acquisition.

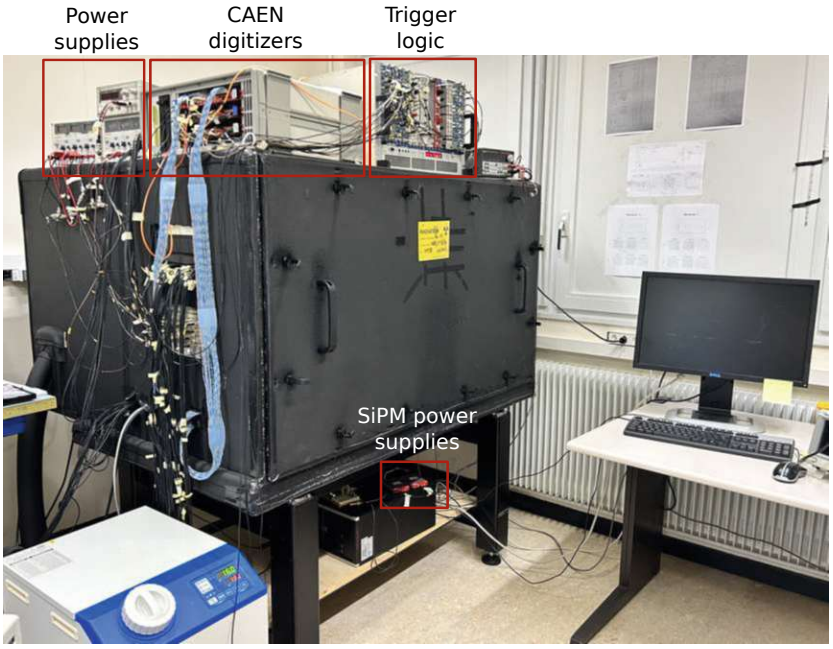

Figure 4.5: Picture of the experimental set-up from the outside. The black box contains the FEBs, the modules and the radioactive source. Patch panels connect the FEBs to external power supplies, digitizers, trigger logic and computer.

Black box

The FEBs, the modules, the radioactive source and the stages are placed inside a light-tight black box (Figure 4.5), where the temperature is kept stable at 18°C by using an external cooling system (HRS018-AF-20-BM from SMC). On one side of the box, patch panels, mezzanines, and holes allow connecting the electronics inside with the external section of the acquisition system. The positive and negative timing signals of each channel coming from the NINO chip are summed (after the inversion of the negative one) to obtain a single signal with a higher amplitude. This is done, for each FEB, in the mezzanine shown at the top of Figure 4.4, on the right.

The patch on Figure 4.4, on the right, is used to power all the components inside the box, through LEMO connectors on the inside and outside of the panel. In particular, the two SiPM arrays are connected to two external low voltage power supplies from CAEN (model DT5485) that are respectively connected to the computer and controlled remotely through a Python script. This allows to perform automatic voltage scans and to change remotely the parameters of the acquisition. Finally, simple holes are used to pass through the flat cables carrying the charge signals and the cable used to control the stages.

Digitalization and acquisition system

The charge signals amplified by the FEBs are fed to a 64 channels Analog to Digital Converter (ADC) by CAEN, model V1740D, shown at the top Figure 4.6. This module samples the signal with a frequency of 62.5 MS/s. The signals are subsequently inte-

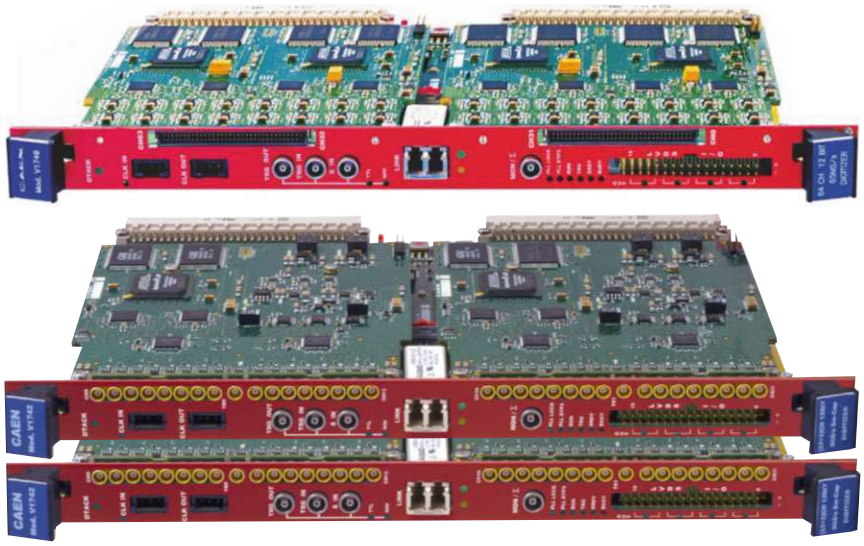

Figure 4.6: CAEN V1740 digitizer and two CAEN V1742 digitizers used for the acquisition of the charge and time signals respectively.

grated by the FPGA present on the module itself and, for each event, the values of the integrals of the signals from each channel are sent to the computer through an optical fiber cable.

The time square signals are fed to two TDCs CAEN V1742, shown on the bottom of Figure 4.6, one for each FEB. These modules are based on a DRS4 chip and sample the signal with a frequency of 5 GS/s (1024 points, corresponding to 200 ps binning). The TDCs digitize the waveforms, which are then sent to the computer via an optical link and analyzed online by the DAQ software. The timestamp for each pulse is computed as the intersection of the rising edge with a fixed threshold.

Each FEB also extracts the sum signal as the sum of all the charge signals, which is used to generate a trigger, as the three CAEN digitizers require the trigger to start the acquisition and digitization of the signals of an event. This involves several NIM modules and is done in multiple steps. First, the sum signal from each FEB is inverted using a LeCroy 428F FAN IN/FAN OUT to match the following modules' input requirements. The inverted signal is fed to an LRS 623A Octal Discriminator with a fixed threshold that produces a square impulse when the threshold is exceeded. One of the two square pulses produced is extended in time using a CAEN 2255B Dual Timer module, to account for the different relative distances between radioactive source and detectors. The square pulses are used as input to an LRS 622 Quad Coincidence module (with AND/OR switches), producing a square pulse in output if the input pulses overlap (AND switch). The coincidence square pulse is multiplied and fed to each CAEN board, to provide a trigger timestamp for the digitizers.

For each triggering event, the V1740 ADC board saves the integral of the charge signal of the 64 channels and the trigger timestamp in one file. Moreover, the two

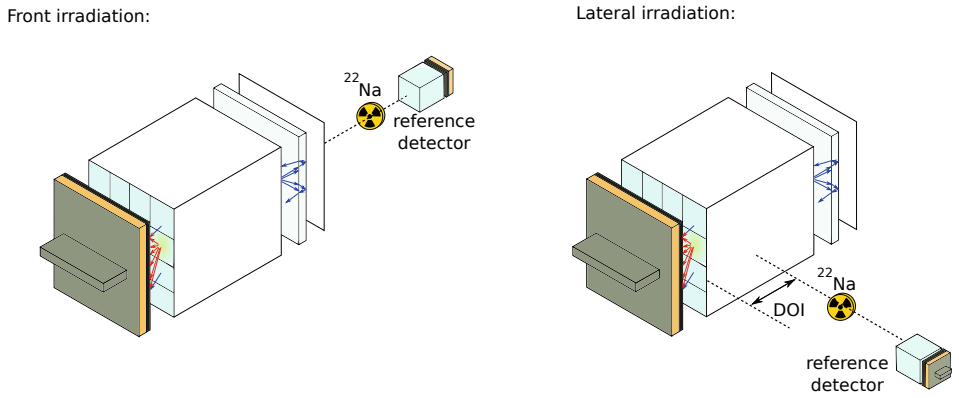

Figure 4.7: Front irradiation set-up used to characterize the crystal-based modules (left) and lateral irradiation set-up used to evaluate the DOI resolution (right).

V1742 TDC boards analyze the signals online to extract the signal timestamps. Also in this case, each board saves the trigger timestamp and the 32 timestamps extracted, one for each channel, in one file. Once the data acquisition is finished, the software parses the three files and compares the trigger timestamps, matching those close enough to be considered relative to the same event. The output of this procedure is a single file that contains, for each event, the trigger timestamps, 64 integrals, and 64 timestamps. The final step is to convert this file into ROOT format for offline analysis. This readout software, which governs the acquisition of the three CAEN boards, also controls the two voltage power supplies for the SiPM arrays and the movement of the stages eventually involved in the acquisition.

4.1.6 Front irradiation

As shown in Figure 4.7 on the left, a PET-like set-up is used to run the standard characterization of the module. The reference detector is placed in front of the crystal matrix, i.e. opposite to the SiPM array, with the source placed in between such that the entire module is irradiated head-on.

4.1.7 Lateral irradiation

To evaluate the DOI resolution, an electronic tagging configuration is used. The source (and the reference detector) are placed to the side of the module so as to irradiate the crystals laterally (Figure 4.7 right). Two Zaber programmable linear stages allow to precisely align and move its position to establish a scan of different DOI positions along the 15 mm long axis of the crystals.

4.2 Methods

4.2.1 Module characterization: timing resolution

The front irradiation set-up allows the characterization of each module in a two-step process: a calibration run followed by an acquisition run to assess the timing performance.

The calibration run is used to record the charge spectrum of the reference crystal and to remove events outside the 511 keV photopeak of the reference crystal. For the remaining events, the calculated values of the (u, v, w) coordinates in the module are entered into a 3D plot. Figure 4.8a shows the sixteen accumulation volumes that can be distinguished and Figure 4.8b the zoom on one of the regions. The accumulation volumes can be identified and separated by means of a custom clustering algorithm [70]. The algorithm starts from a seed defined as the voxel with the highest number of counts C_0. It then analyses all nearby voxels, discarding the ones with a number of counts lower than a threshold C_{th}, which is defined as a fraction of C_0. The procedure is then repeated recursively for all seeds and, when no more new seeds are found, the volume associated with the complete set of seeds defines a cluster. These voxels are then removed from the 3D histogram, and the procedure starts again until 16 clusters are found. Figure 4.9b shows the results of the algorithm applied to one of the crystal volumes. The volumes identify gamma rays interacting with individual crystals. Events

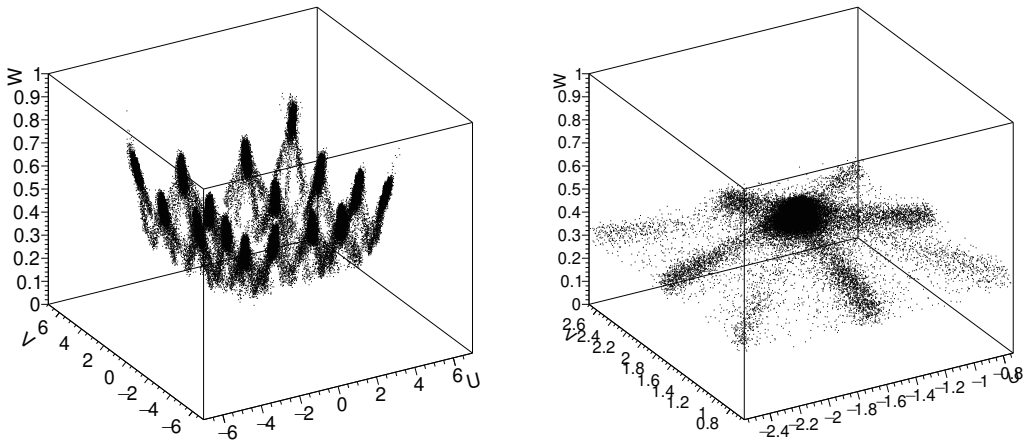

(a) (b)

Figure 4.8: Identification of the crystal of interaction of the gamma rays using the DOI-capable module, Hamamatsu model S13361-3050AE-04 SiPM array and NINO 32-chip board for the readout. (a) 3D histogram of all events of a calibration run plotted for a DOI capable module. 16 accumulation volumes can be distinguished. (b) To help visualization, the histogram is zoomed into an (u, v) area corresponding to crystals coupled to a single SiPM.

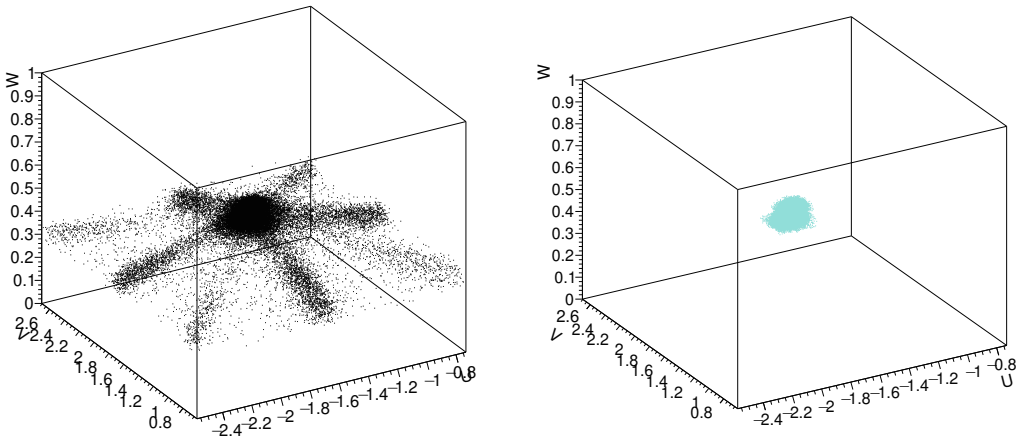

(a) (b)

Figure 4.9: Identification of the crystal of interaction of the gamma rays using the DOI-capable module, Hamamatsu model S13361-3050AE-04 SiPM array and NINO 32-chip board for the readout. (a) (u, v) area corresponding to a crystal coupled to a single SiPM. (b) Result obtained after application of the clustering algorithm.

whose (u, v, w) coordinates fall outside of these delineated regions can be interpreted as inter-crystal scatters, i.e. events where a single gamma ray is depositing its energy in more than one crystal. For the purpose of this study, these events are discarded. Using the standard module, the events will be confined within a region close to w = 1.0, whereas in the DOI-capable module, the region is more widely spread out and closer to w = 0.0. For events in each volume, the charge spectrum is reconstructed, allowing to determine the region of photopeak selection and at the same time to evaluate the energy resolution. Once the events in the photopeak of the individual crystals are selected, a DOI calibration curve (Figure 4.10) can be established for each scintillator that allows the exact reconstruction of the physical gamma interaction coordinate from the w value, as described in [70] using the exponential gamma attenuation function in the crystal (Section 2.1.3).
Subsequently, a 2D histogram of the time delay $t_1 - t_i$ versus w is built for each detector (Figure 4.11a), and the experimental relations $g_i(w) = [t_i - t_1](w)$, denoting the average delay of the i_{th} photodetector with respect to the detector of interaction D_1, and the DOI coordinate w are plotted for each i. Finally, a 2D scatter plot of $t_1 - t_{ref}$ versus w is produced, to derive $d(w)$, i.e. the average delay expected as a function of w between t_1 and a fixed external reference (Figure 4.11b).

After calibration, the acquisition run is analyzed to assess the timing performance. Only events simultaneously recorded in the photopeak of one of the crystals of the module and the reference crystal are taken into account. The first delay histogram H_{std} is constructed without taking advantage of the DOI correction, i.e. taking into account only the difference between the timestamp t_1 of the photodetector coupled to

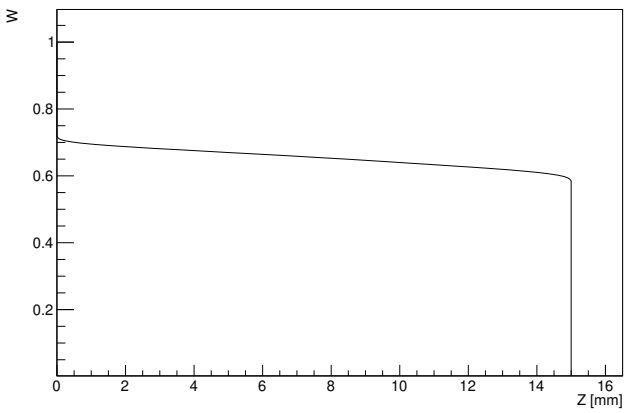

Figure 4.10: Calibration curve to correctly reconstruct the physical DOI coordinate using the gamma attenuation function, in front irradiation, after selection of events in the accumulation volume and photopeak region of each individual crystal using the DOI-capable module, Hamamatsu model S13361-3050AE-04 SiPM array and NINO 32-chip board for the readout.

the crystal of interaction and t_{ref} the timestamp of the reference crystal.

$$\Delta t_{std} = t_1 - t_{ref} \tag{4.3}$$

The second histogram H_{corr} exploits the $d(w)$ and $g_i(w)$ functions extracted from the calibration run to correct for the DOI by using

$$\Delta t_{corr} = \hat{\Theta_{in}} - t_{ref} \tag{4.4}$$

with

$$\hat{\Theta_{in}} = \frac{\sum_{i=1}^{16}(1/\sigma^2)\cdot(t_i - g_i(w))}{\sum_{i=1}^{16}(1/\sigma^2)} - [d(w) - d(w_0)] \tag{4.5}$$

The H_{std} and H_{corr} distributions are fitted with an exponentially modified Gaussian distribution to extract the FWHM, and are corrected for the contribution of the reference detector as

$$CTR = \sqrt{2\cdot CTR^2_{measured} - CTR^2_{reference}} \tag{4.6}$$

4.2.2 Module characterization: DOI resolution

Using the lateral irradiation set-up, it is possible to irradiate the matrix at known DOI positions, provided by the vertical position of the source and the reference crystal. Thus, the correlation of the DOI with the w coordinate can be studied. After applying the clustering algorithm [70], the w distribution for the different vertical positions of the reference crystal is shown in Figure 4.12a. It is observed that, as expected, the peak position varies with z in strong correlation with the w coordinate derived from DOI

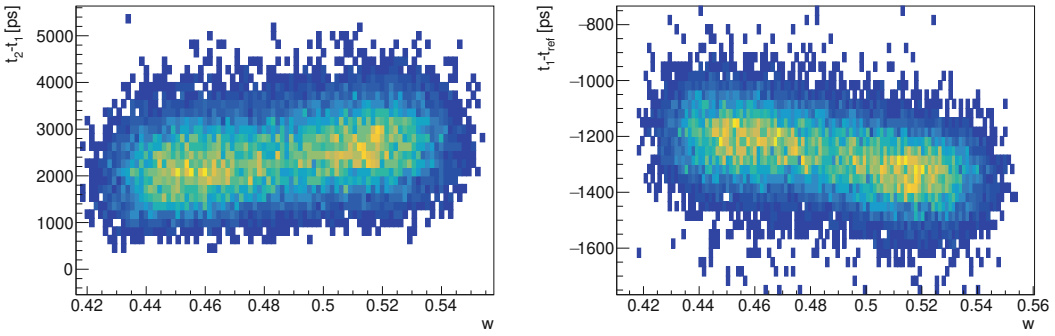

(a) (b)

Figure 4.11: (a) Scatter plot of the time delay $t_1 - t_i$ versus w built for each detector to extract the average time delay of the i_{th} photodetector with respect to the detector of interaction as a function of w. (b) Scatter plot of the time delay $t_1 - t_{ref}$ versus w, to derive the average delay expected as a function of w between the crystal of interaction and the external reference crystal.

information. Plotting the vertical position of the interaction versus the peak position of the w distributions a linear relation between the two variables can be established (Figure 4.12b)

$$DOI = m \cdot w + q \tag{4.7}$$

Using this correlation to correct the peak values of each w distribution for the corresponding position in space and summing all events, a Gaussian distribution is obtained. Fitting the distribution with a Gaussian function yields the crystal DOI resolution in FWHM. Repeating the process for each irradiated crystal, the DOI resolution of the module is defined as the mean value of all the extracted DOI resolutions.

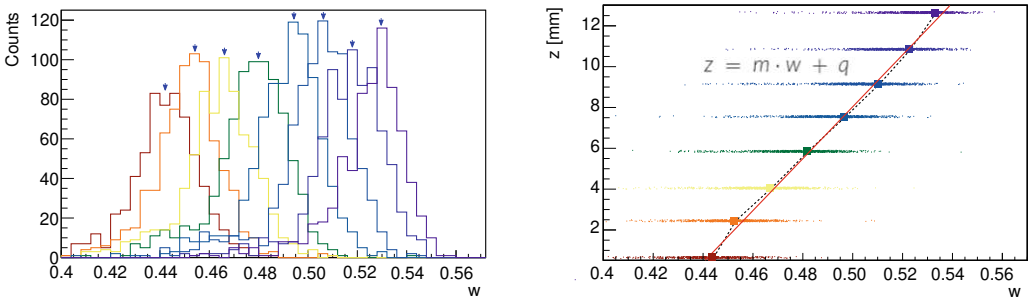

(a) (b)

Figure 4.12: Lateral irradiation after application of the clustering algorithm using the DOI-capable module, Hamamatsu model S13361-3050AE-04 SiPM array and NINO 32-chip board for the readout. (a) w distributions for different vertical positions of the reference crystal. (b) Linear relationship between the vertical position of the interaction and the peak position of the w distributions.

4.3 Results

This section presents the evaluation of the timing performance for both the standard and DOI-capable modules using different SiPM arrays from Hamamatsu and Broadcom. Additionally, the DOI-capable module is laterally irradiated to assess its performance in terms of DOI resolution.

4.3.1 Standard module

Table 4.1 summarises the results obtained for each SiPM array. The new high-performance NUV-MT SiPM array from Broadcom achieves the best result, with a CTR of 141 ± 4 ps FWHM, at an overvoltage (OV) of 9 V. In comparison, the Broadcom NUV-HD SiPM array reaches a CTR of 166 ± 5 ps at OV = 4 V, while the Hamamatsu 13361-3050AE-04 array achieves a resolution of 162 ± 2 ps at OV = 7 V. These results highlight the superior performance of the NUV-MT SiPM array in terms of timing resolution under the tested conditions.

Table 4.1: CTR results using the standard module, coupled to different SiPM types from Hamamatsu and Broadcom, with NINO 32-chip board in front irradiation configuration.

SiPM array	OV [V]	CTR FWHM [ps]
Hamamatsu 13361-3050AE-04*	7 V *	162 ± 2 ps*
Broadcom NUV-HD	4 V	166 ± 5 ps
Broadcom NUV-MT	9 V	141 ± 4 ps

* Values from [5]

4.3.2 DOI-capable module

DOI evaluation

The reference detector is positioned on the lateral side of the detector array at a distance that ensures the irradiation of a spot with a maximum diameter of 1 mm. Measurements are conducted at the optimal OV identified for the standard module. The DOI resolution is evaluated as described in Section 4.2.2. The results obtained using the Hamamatsu and Broadcom arrays are summarized in Table 4.2.

Table 4.2: DOI results of the DOI-capable module, coupled to different SiPM types from Hamamatsu and Broadcom, with the NINO 32-chip board in lateral irradiation.

SiPM array	OV [V]	DOI FWHM [mm]
Hamamatsu 13361-3050AE-04*	7 V *	3.1 ± 0.1 mm*
Broadcom NUV-HD	4 V	3.2 ± 0.1 mm
Broadcom NUV-MT	9 V	2.5 ± 0.2 mm

* Values from [5]

CTR evaluation

The reference detector is repositioned in front of the detector array, with the source placed in between to ensure uniform irradiation across the entire crystal matrix. Measurements are performed at the optimal overvoltage settings determined for each SiPM array. The results are summarized in Table 4.3, where the CTR is compared before and after applying the DOI correction, as well as with the standard module.

Table 4.3: CTR results using the DOI module, coupled to different SiPM types from Hamamatsu and Broadcom and readout using the NINO 32-chip board in front irradiation configuration. The results of the standard module at the same SiPM array OV are also shown for comparison. The Hamamatsu SiPM type is 13361-3050AE-04.

	DOI module		std module
SiPM array	CTR_{std}	CTR_{corr}	CTR_{std}
Hamamatsu*	233 ± 2 ps *	165 ± 2 ps *	162 ± 2 ps*
Broadcom NUV-HD	253 ± 8 ps	179 ± 6 ps	166 ± 5 ps
Broadcom NUV-MT	247 ± 7 ps	170 ± 5 ps	141 ± 4 ps

* Values from [5]

4.4 Discussion

The Broadcom NUV-MT SiPM array demonstrated a significant improvement in the timing performance of the standard module, achieving a coincidence timing resolution of 141 ± 4 ps FWHM when read-out with the custom-made NINO 32-chip board. This result outperforms those of the other tested SiPM arrays, highlighting the potential of the NUV-MT technology for high-precision applications.

For the development of a high-resolution PET scanner designed for imaging small animals or specific organs in the human body, the ability to extract DOI information is essential for correcting parallax errors. The DOI-capable module achieves a DOI resolution of approximately 3 mm. This resolution improves slightly when the Broadcom NUV-MT array is used, thanks to its capability to operate at higher bias voltages while maintaining a low current and therefore benefitting from a higher PDE and number of detected photons, compared to the other technologies. Despite initial degradation in time performance due to the depolishing of the crystal surfaces and increased light-sharing, the integration of DOI information partially recovers the time resolution. The Broadcom NUV-MT array once again achieves the best results among the tested arrays. Nevertheless, the CTR for the DOI-capable module remains worse compared to that of the standard module. This can be attributed to several factors. Firstly, the geometry of the crystal matrix allows a perfect one-to-one alignment of crystals to SiPMs only for the Hamamatsu SiPM array. In contrast, the Broadcom NUV-HD and NUV-MT arrays, with active areas of 3x3 mm^2 and 3.72x3.62 mm^2 respectively, do not perfectly

match the crystal matrix. Despite precise alignment is less critical for polished crystal matrices, it becomes crucial for DOI-capable configurations because they are prone to correlations due to light detected by neighboring SiPMs. Additionally, the use of Cargille Meltmount instead of a 50 μm OCA layer to couple the crystal matrices to the Broadcom SiPM arrays contributes to increased front light sharing. Over time, the coupling material penetrates between the crystals, thus increasing front light sharing and reducing DOI dependence in the region close to the SiPM. Simulations indicate that this effect could be mitigated by employing thinner layers of coupling material between the crystal matrix and the SiPMs. While such a solution was not feasible in this study due to the fragile nature of the SiPM arrays, it holds promise for improving both DOI resolution and time performance in future designs.

Although the custom-made NINO 32-chip board demonstrates excellent timing performance, it is not scalable to a full system, due to the limitation in the number of channels, power consumption (27 mW/channel [53]), and the need for a more integrated signal digitization and acquisition system.

4.5 Summary and conclusion

The DOI-capable module has been evaluated in terms of both timing and DOI performance using different SiPM arrays from Broadcom and Hamamatsu available on the market and the custom-made NINO 32-chip based electronics. Promising results are obtained, with a DOI resolution of 2.5 $\pm$ 0.2 mm FWHM and a timing resolution of 170 $\pm$ 5 ps FWHM achieved using the newly introduced NUV-MT array. [69]. These improvements can be attributed to the high PDE and low cross-talk of this technology.

Despite these encouraging results in terms of timing resolution, the custom-made setup is not scalable to a full system due to its high power consumption and large dimensions. Consequently, the PETsys TOFPET2 ASIC has been explored to assess the performance of the detector module with a commercially available and scalable readout electronics solution. This evaluation will be discussed in detail in the next chapter.

5 Scalability of the TOF - DOI capable PET module using PETsys TOFPET2 ASIC

The detector module presented in the previous chapter makes use of a matrix of several LYSO:Ce scintillators coupled to an array of SiPMs and a light guide to perform measurements of time and energy and exploit their combination to extract the information on the depth of interaction of the gammas inside the detector.

To apply this concept on a full system, such as small PET prototypes, preclinical or clinical PET scanners, advanced readout techniques that handle a large number of channels, as well as event digitization using ASICs and advanced data handling using FPGAs, capable of operating under high-rate conditions, are essential. TOFPET2 ASIC by PETsys Electronics S.A [54] represents a promising solution as a 64-channel integrated circuit able to process data rates of up to 600 kHz per individual channel and a maximum power consumption of 8.2 mW per channel.

This chapter presents the evaluation of the performance of the TOF- and DOI-capable module using the commercially available low-power and scalable PETsys TOFPET2 ASIC [71, 72] illustrated in Figure 5.1. Section 5.1 introduces the TOFPET2 ASIC and its readout chain. Section 5.2 presents the results obtained, followed by the discussion on the comparison with the NINO 32-chip based electronics (Section 5.3) and conclusions (Section 5.4).

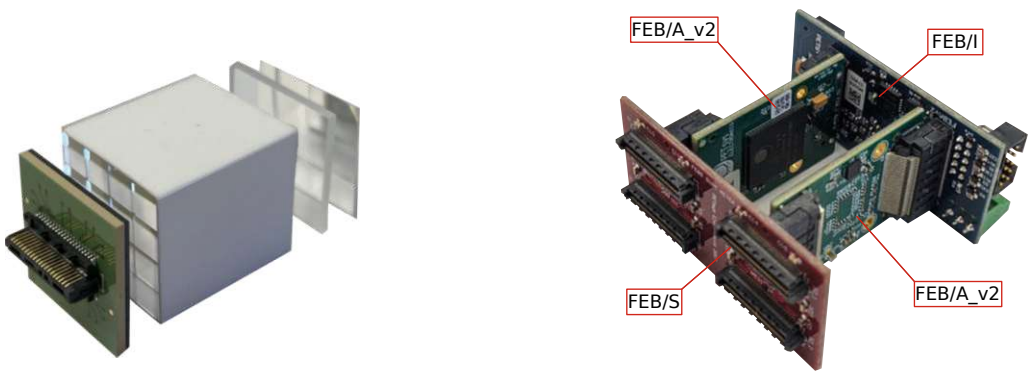

Figure 5.1: Pictures of TOF- and DOI-capable module and PETsys TOFPET2 ASIC from PETsys Electronics S.A.

5.1 Materials and Methods

For this study, an experimental set-up based on the use of PETsys TOFPET2 ASIC is exploited for the measurement of two detectors read-out in coincidence. The experimental measurements have been conducted at the RWTH Aachen University in Aachen, Germany, in collaboration with the Department of Physics of Molecular Imaging Systems.

Standard and DOI-capable TOF-PET modules, coupled to the S13361-3050AE-04 SiPM array from Hamamatsu, the array of 16 NUV-HD SiPMs and the 4×4 NUV-MT SiPM array from Broadcom, are measured in coincidence with a reference detector made of a 2x2x3 mm^3 LSO:Ce:Ce crystal coupled to a high-performance NUV-MT SiPM from Broadcom (model AFBR-S4N44P014M).

5.1.1 PETsys TOFPET2 ASIC

The TOFPET2 ASIC evaluation kit by PETsys Electronics S.A. (TOFPET2 ASIC version 2c) is used for this study. After calibrating the channel baselines and TDCs and QDCs, making use of the calibration routine provided with the evaluation kit software, bias and threshold scans can be performed. In particular, a reduced input stage impedance of approximately 11Ω (by setting fe_ib1 = 0 in the ASIC configuration file) and default trigger configuration (three-threshold trigger logic) are used. Increasing vth_t2 and vth_e by one digital-to-analog converter (DAC) step is equal to increasing the trigger level by approximately 15 mV and 20 mV, respectively, over a baseline set during calibration. The second timing threshold vth_t2 = 20 and the energy threshold vth_e = 15 are kept constant, whereas the first timing threshold vth_t1 is set to the least significant bit (lsb) value of 6.66 mV [73]. Using the convert_raw_to_singles_method, acquired raw data are converted to single hit information, each with a timestamp, energy value, and channel-ID, as described in Section 3.3.2, allowing the evaluation of the energy deposited and photon time deposition for each crystal of the detector module array. As opposed to the set-up described in Chapter 4, where coincidence events between the detectors are directly recorded, in this case, single hits are stored, and coincidence events must be reconstructed using an appropriate coincidence window. The window is carefully chosen to ensure that up to sixteen channels of the array can be activated for coincidences within the detector module itself, as shown in Figure 5.2, or up to seventeen channels when the reference detector is included.

5.1.2 Measurement set-up

Two FEM-128 are used to read out in coincidence, using a ^{22}Na source with 3.2 MBq activity, the reference detector and a detector module. Figure 5.3 shows the picture of the experimental set-up, consisting of the detectors readout by the FEM-128 boards, the flexible HQCD cable connecting the FEMs to the motherboard, and the motherboard placed on top. The set-up is enclosed in a box kept at a stable temperature of 18°C and is connected via a USB cable to a computer to control the acquisition.

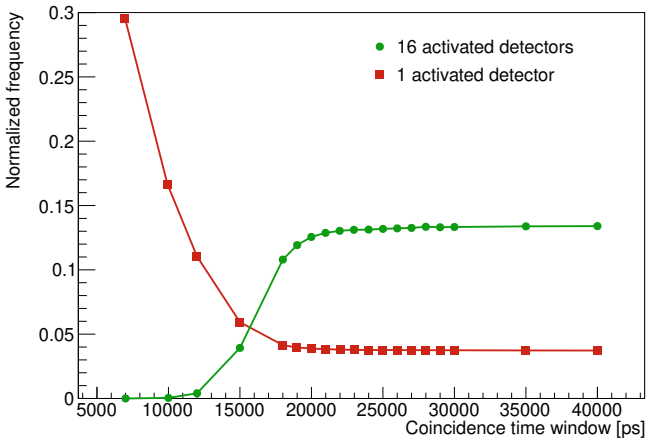

Figure 5.2: Frequency of events in which only 1 or 16 coincidences are obtained as a function of the time window. A time window greater than 30000 ps is chosen.

Mechanical set-up

The detector array is mounted on an automatic linear stage from Zaber to allow movements in the two directions of the plane perpendicular to the axis described by the reference crystal and sodium source, as shown in Figure 5.3. The stage is connected to the computer used to run the acquisition that automatically changes the positioning during multiple data acquisitions.

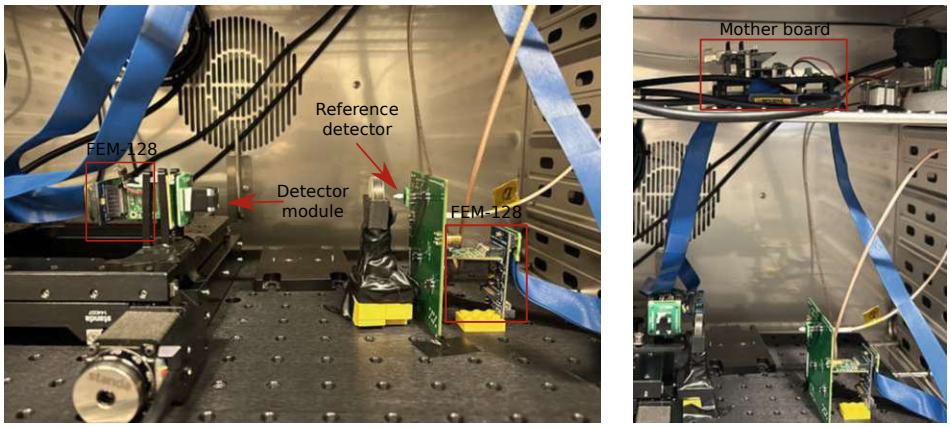

Figure 5.3: Pictures of the FEMs connected via flexible HQCD cables to the motherboard placed on top. Everything is placed inside a black box and connected via a USB cable to the computer to control the acquisition. The two FEMs are respectively connected to a reference detector on the right and a standard detector module on the left that is mounted on two automatic linear stages from Zaber (left) in front irradiation configuration or (right) in lateral irradiation configuration.

5.1.3 Energy calibration

Due to the limited number of SPADs that compose each SiPM, saturation effects occur in the energy response. To be able to make the response of the SiPM linear with respect to the deposited energy in the crystal coupled to it and to evaluate and compensate for the different gains of each SiPM, energy calibration is needed. Short measurements are performed without coincidence with the reference detector to acquire the full energy spectrum of ^{22}Na for each SiPM. The position of the two photopeaks, corresponding to the 511 keV and 1275 keV gamma emissions as described in Figure 2.10, are used. From Equation 3.14

$$y = a \cdot (1 - e^{-x \cdot \frac{b}{a}}) \tag{5.1}$$

It is possible to extract the saturation parameter a and use it to equalize and linearize the response of each SiPM inverting Equation 5.1. The procedure must be repeated at different OV (Figure 5.4).

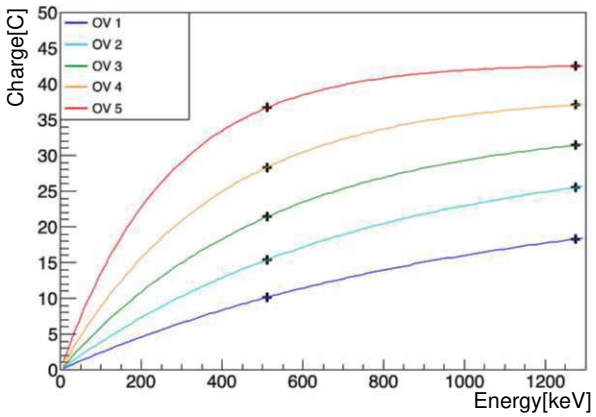

Figure 5.4: Saturation curves at different OV using the polished detector module using PETsys TOFPET2 ASIC.

5.2 Results

Results of time and DOI resolutions are presented for the standard and DOI-capable modules respectively. A comparison with the performance obtained using the custom-made NINO 32-chip board presented in Chapter 4 is also included.

5.2.1 Standard module

Using the PETsys TOFPET2 ASIC, measurements are repeated by varying the SiPM array overvoltage OV and the timing threshold vth_t1 for the different SiPM arrays. The results of these measurements are displayed in Figure 5.5. The best timing resolution for the Hamamatsu SiPM array is found to be 205 ± 8 ps FWHM at overvoltage OV = 4 V and a threshold vth_t1 = 20. A similar value of 206 ± 8 ps is achieved for the Broadcom NUV-HD array at a threshold vth_t1 = 20 and OV = 8 V. The Broadcom NUV-MT

array delivers an improved timing resolution of 193 ± 6 ps at OV = 7 V and threshold vth_t1 = 40. To convert the threshold vth_t1 into mV, a lbs value of 6.6 mV should be used. Table 5.1 summarises the best timing resolution results achieved with the PETsys TOFPET2 ASIC, compared to those obtained with the NINO 32-chip board. Notably, the best result with the NINO 32-chip board is a CTR of 141 ± 4 ps FWHM using the Broadcom NUV-MT array.

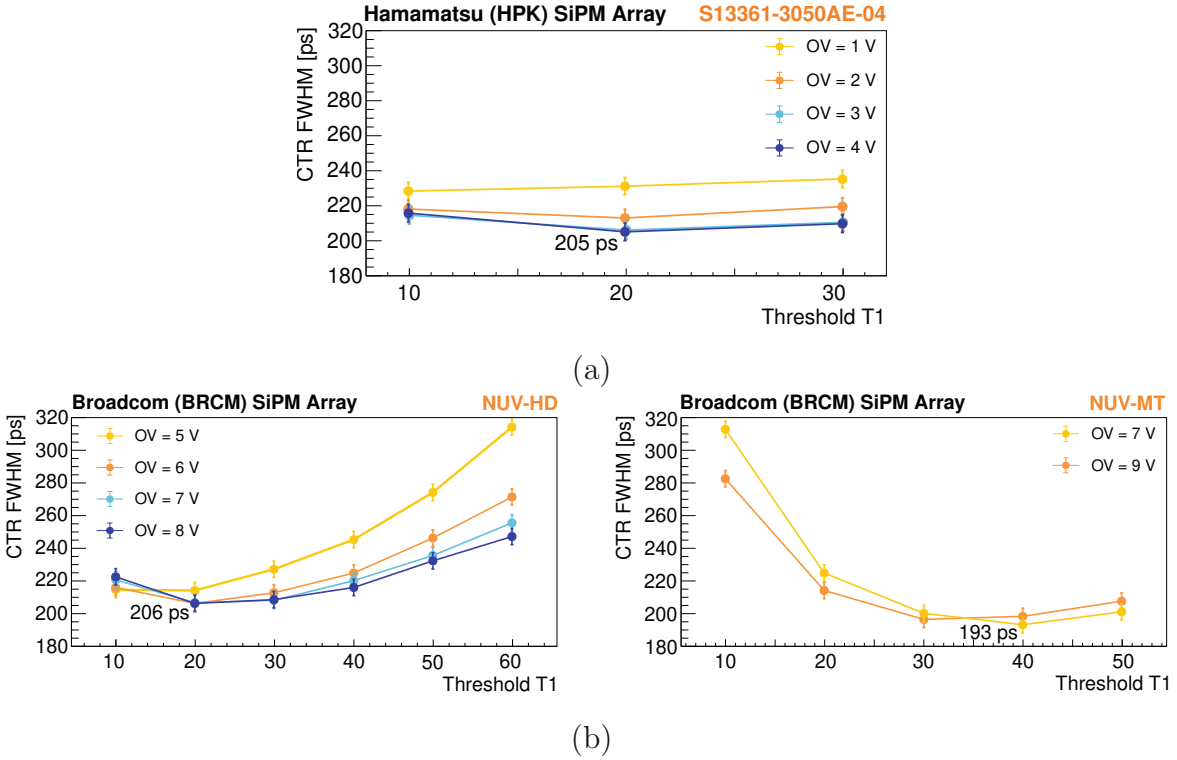

Figure 5.5: CTR results using the standard module and PETsys TOFPET2 ASIC. (a) Hamamatsu SiPM array and (b) Broadcom NUV-HD and NUV-MT.

Table 5.1: CTR results using the standard module, coupled to different SiPM types from Hamamatsu and Broadcom with PETsys TOFPET2 ASIC and NINO 32-chip board readout in front irradiation configuration. To convert the threshold vth_t1 into mV, a lbs value of 6.6 mV should be used. The Hamamatsu SiPM model is 13361-3050AE-04.

Electronic readout	SiPM array	OV [V]	Threshold	CTR FWHM [ps]
PETsys TOFPET2 ASIC	Hamamatsu	4 V	20	205 ± 8 ps
	Broadcom NUV-HD	7 V	20	206 ± 6 ps
	Broadcom NUV-MT	9 V	40	193 ± 6 ps
NINO 32-chip board	Hamamatsu*	7 V *	-	162 ± 2 ps*
	Broadcom NUV-HD	4 V	-	166 ± 5 ps
	Broadcom NUV-MT	9 V	-	141 ± 4 ps

* Values from [5]

5.2.2 DOI-capable module

DOI evaluation

As described in Section 4.3.2, the reference detector is positioned on the side of the detector array at a distance that ensures the irradiation of a spot with a maximum diameter of 1 mm. The measurement is made at the optimal OV of the measurement of the standard module. Results and comparison with the DOI resolution obtained using the NINO 32-chip board are summarized in Table 5.2.

Table 5.2: DOI results with the DOI capable module, coupled to different SiPM types from Hamamatsu and Broadcom, and read out with PETsys TOFPET2 ASIC and the NINO 32-chip board in lateral irradiation configuration.

Electronic readout	SiPM array	OV [V]	DOI FWHM [mm]
PETsys TOFPET2 ASIC	Hamamatsu 13361-3050AE-04	4 V	3.5 ± 0.3 mm
	Broadcom NUV-HD	7 V	2.9 ± 0.4 mm
	Broadcom NUV-MT	9 V	2.6 ± 0.2 mm
NINO 32-chip board	Hamamatsu 13361-3050AE-04*	7 V *	3.1 ± 0.1 mm*
	Broadcom NUV-HD	4 V	3.2 ± 0.1 mm
	Broadcom NUV-MT	9 V	2.5 ± 0.2 mm

* Values from [5]

CTR evaluation

Using the PETsys TOFPET2 ASIC, measurements are repeated varying the threshold vth_t1 at the optimal overvoltage found for the different SiPM arrays and the standard module. The results of the measurements are shown in Figure 5.6 for the DOI capable module, comparing the CTR extracted before and after DOI correction. The optimal values are summarized in Table 5.3 and compared to the results obtained using NINO 32-chip board.

5.3 Discussion

The feasibility of building a full PET scanner using modules based on commercially available crystals, SiPMs and electronics with a timing resolution below 200 ps is demonstrated through the measurements of the standard module coupled to a NUV-MT SiPM from Broadcom. This configuration achieves a CTR of 193 ± 6 ps FWHM when read-out with the PETsys TOFPET2 ASIC. The performance of the crystal detector is further enhanced when using the custom-made NINO 32-chip board, where a CTR of 141 ± 4 ps FWHM is achieved. Despite the superior timing resolution demonstrated by the custom-made NINO 32-chip board, it is not scalable to a full system due to several limitations. These include the restricted number of channels (limited to 32 for each board), relatively high power consumption (27 mW/channel [53]), and a signal digitization and acquisition system that relies on CAEN digitizers, which offer a higher

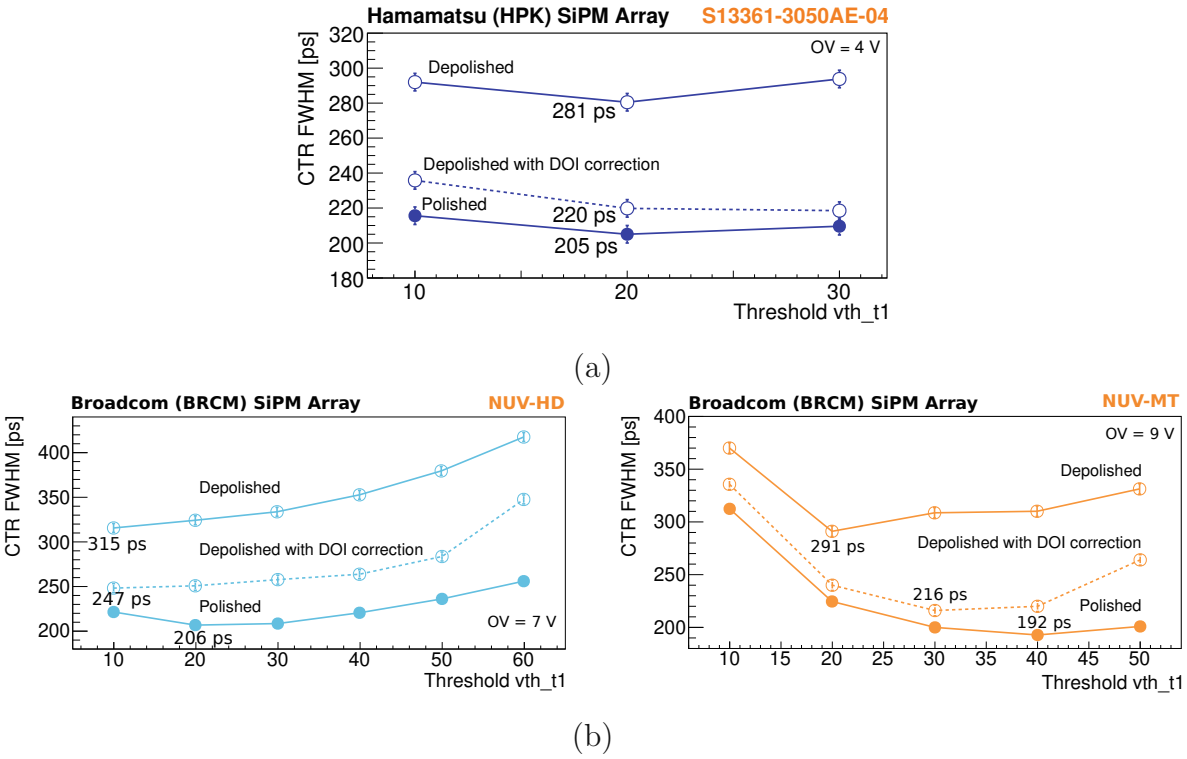

Figure 5.6: CTR results using the DOI-capable module and PETsys TOFPET2 ASIC. (a) Hamamatsu SiPM array and (b) Broadcom NUV-HD and NUV-MT.

Table 5.3: CTR results using the DOI module, coupled to different SiPM types from Hamamatsu and Broadcom and readout using PETsys TOFPET2 ASIC and the NINO 32-chip board in front irradiation configuration. The results of the standard module at the same SiPM array OV are also shown for comparison. The Hamamatsu SiPM model is 13361-3050AE-04.

		DOI module		std module
Electronic readout	SiPM array	CTR_{std}	CTR_{corr}	CTR_{std}
PETsys TOFPET2 ASIC	Hamamatsu	281 ± 8 ps	224 ± 8 ps	205 ± 8 ps
	Broadcom NUV-HD	315 ± 7 ps	247 ± 7 ps	206 ± 6 ps
	Broadcom NUV-MT	291 ± 6 ps	216 ± 6 ps	193 ± 6 ps
NINO 32-chip board	Hamamatsu*	233 ± 2 ps*	165 ± 2 ps*	162 ± 2 ps*
	Broadcom NUV-HD	253 ± 8 ps	179 ± 6 ps	166 ± 5 ps
	Broadcom NUV-MT	247 ± 7 ps	170 ± 5 ps	141 ± 4 ps

* Values from [5]

sampling frequency compared to the PETsys TDC/ADC setup but is not integrated to the read-out. Regarding DOI performance, the DOI-capable modules using the PETsys TOFPET2 ASIC achieve a DOI resolution as good as 2.6 ± 0.3 mm when coupled to the Broadcom NUV-MT array, which is consistent with the measurement obtained using the NINO 32-chip board.

5.4 Summary and conclusion

Using the commercially available PETsys TOFPET2 ASIC, TOF and DOI performances as good as 216 ± 6 ps FWHM CTR and 2.6 ± 0.2 mm FWHM DOI resolution are achieved. While the DOI resolution is comparable to that obtained with the custom-made NINO 32-chip board, the CTR performance is worse when using the PETsys TOFPET2 ASIC. However, the advantage of the TOFPET2 ASIC lies in its scalability, making it suitable for large-scale applications in both preclinical and clinical PET detectors. The light-sharing scheme effectively enables the extraction of the DOI information with high resolution, partially compensating for the loss in CTR. Furthermore, when the standard module is coupled with the NUV-MT arrays and the PETsys TOFPET2 ASIC, a CTR of 193 ± 6 ps FWHM is achieved, demonstrating the feasibility of building a prototype with time resolution below 200 ps FWHM. Both PETsys TOFPET2 ASIC and the custom-made NINO 32-chip board demonstrate excellent performance when paired LYSO:Ce crystals, thanks to its high light yield and fast scintillation kinetics. These characteristics allow for good energy and time resolutions, even at high thresholds of timestamp extraction. This is not the case for BGO or materials with slower scintillation profiles (Table 3.1). For these materials, faster electronics and lower leading edge detection thresholds are necessary to effectively exploit their fast yet faint Cherenkov production. To address this need, the HF concept is investigated in the next chapter.

III

Pushing the timing resolution towards 100 ps

6 Pushing the timing performance using Low-power Low-noise High-Frequency electronics

A promising solution for electronic readout is the use of low-noise high-frequency circuits, which have demonstrated outstanding timing performance in TOF-PET applications[60, 61]. The use of HF circuits allows to minimize the electronic noise jitter influence on the single photon time resolution. This capability allows fast luminescence signatures and prompt optical phenomena to be optimally exploited for time of interaction estimators, overcoming the timing limitation of the NINO amplifier-discriminator chip and PETsys ASIC.

The readout of a single SiPM coupled to a scintillator pixel using single-channel HF electronics has been extensively studied [60, 61] to evaluate the characteristics and limitations of crystal light emission and SiPMs. However, to investigate the TOF-PET modules introduced in the previous chapter, comprising segmented matrices of small crystals coupled to photodetector arrays, parallel readout of multiple SiPMs using multi-channel electronics is required. This chapter presents an evaluation of the performance of the first prototypes of a sixteen-channel electronic readout, based on radio-frequency amplifiers and fast discriminators, developed by the Biomedical Imaging team at Berkeley National Laboratory. The low-power low-noise high-frequency

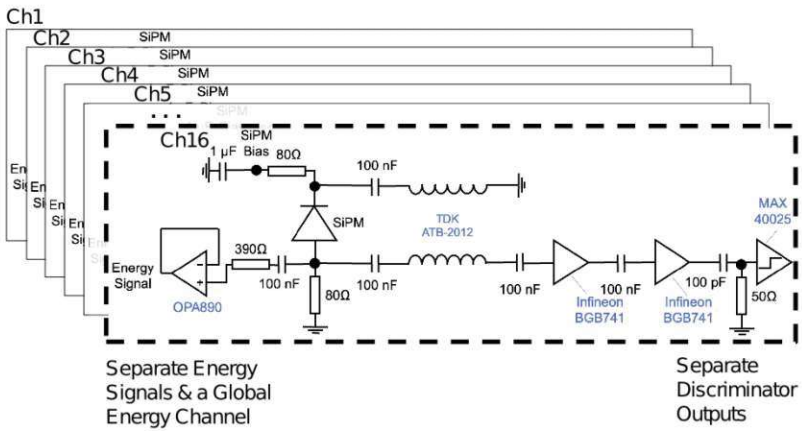

Figure 6.1: Schematic representation of the 16-channel LPLN-HF development board.

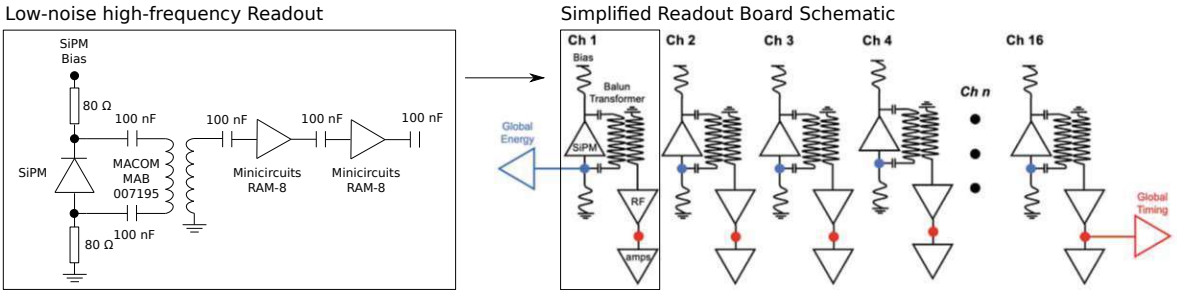

Figure 6.2: Schematic representation of the first version of the sixteen-channel low-noise high-frequency development board.

(LPLNHF) sixteen-channel development board is shown in Figure 6.1. The development and refinement of the single-channel low-power high-frequency (LNHF) electronics, which led to the sixteen-channel board, has been a journey of several years that accompanied me through my PhD research.

Section 6.1 presents the first version of the board and discusses its performance and limitations. Section 6.2 introduces a second, improved version of the board, which addresses the issues encountered with the first design. The time, energy, and DOI performance evaluations are presented and compared with the electronic readout boards discussed in previous chapters. Finally, Section 6.3 and 6.4 discuss the results and suggest potential improvements for the characterization and study of alternative materials to LYSO:Ce.

6.1 LNHF electronics readout - version 1.0

The first prototype of a sixteen-channel LNHF development board [55] consists of a modified version of the LNHF signal processing chain described in [7] and presented in Section 3.3.3. The schematic is illustrated in Figure 6.2, and Figure 6.3 displays a picture of the board. In the sixteen LNHF electronic readout board (Figure 6.3a):

- A RF-amplifier is used to provide high gain and large amplitude for single photon pulses, producing fast analog time signals.
- Moreover, the analog signals are also extracted before the amplification stages and used for energy quantification.
- Finally, a global energy signal, containing the information on the charge collected by all the SiPMs is also extracted.

The analog timing signals are then fed into a booster board (Figure 6.3b), where they undergo a second amplification stage and where a fast discriminator extracts a fast digital signal containing in its leading edge the time information of the crossing point between the analog time signal and a fixed threshold.

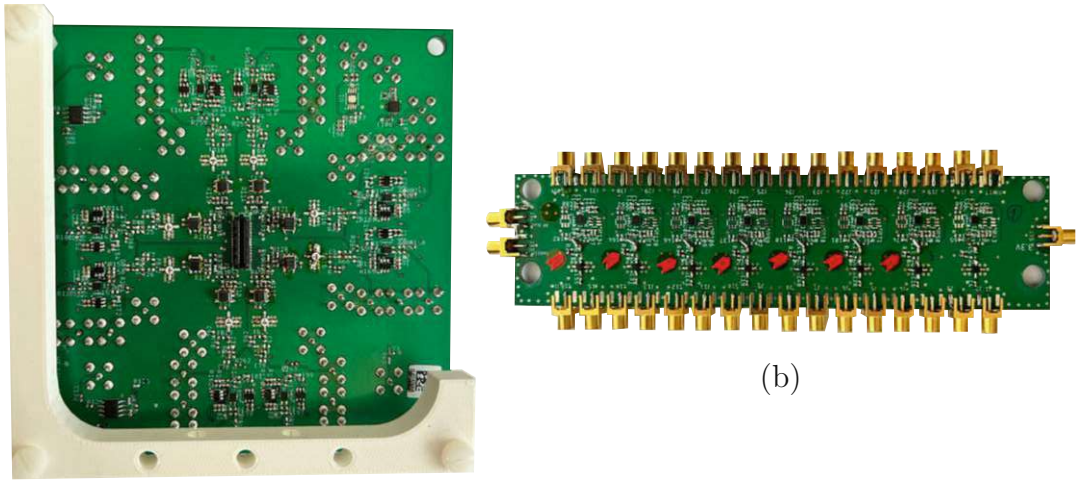

(a) (b)

Figure 6.3: (a) Picture of the sixteen-channel LNHF electronics readout board and (b) booster board.

6.1.1 Results with LYSO:Ce standard matrix

The LYSO:Ce standard module, coupled to the Hamamatsu S13361-3050AE-04 SiPM array, is used to test the board. The limitation of the current electronic board is the poor resolution of the analog energy signals, which anyway allows to be able to distinguish sixteen accumulation volumes in the scatter plot of the reconstructed (u,v) coordinates, as illustrated in Figure 6.4a. CTR_k is evaluated for each channel k at 58 V of bias voltage (5 V of OV), and the resulting values, corrected for the contribution of the reference detector, are shown in Figure 6.4b. After averaging over the entire detector array, we achieve a CTR value of

$$CTR_{HF} = 153 \pm 3 \text{ ps FWHM} \tag{6.1}$$

The same measurement, performed with the custom-developed 32 channels FEB based on the NINO-32 amplifier discriminator chip provided a CTR value of

$$CTR_{NINO} = 162 \pm 2 \text{ ps FWHM}. \tag{6.2}$$

6.2 LPLNHF electronics readout - version 2.0

The second version of the board is called low-power, low-noise, and high-frequency (LPLNHF) electronics readout board. It maintains the idea of a timing signal with high gain and large amplitude, improving the extraction of the information on the energy deposited and the consequent charge collection, to allow not only a precise energy determination but also its use for DOI evaluation. Therefore, the output signal of each SiPM of the array is split and processed in parallel by two distinct branches:

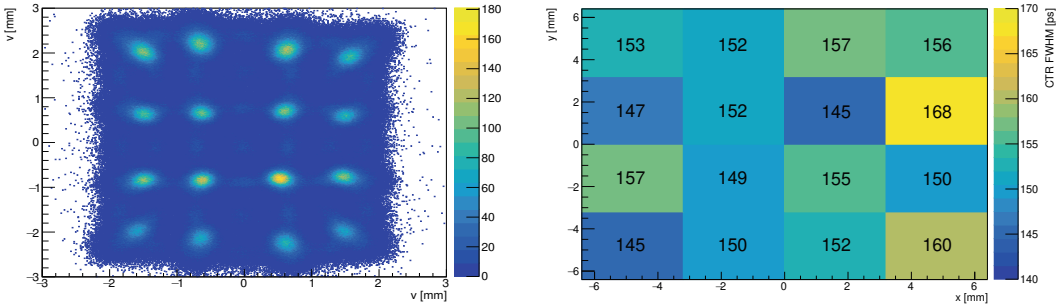

(a) (b)

Figure 6.4: Results using the LYSO:Ce standard matrix coupled to the Hamamatsu S13361-3050AE-04 SiPM array readout using the first version of the sixteen-channel LNHF development board and the CAEN V1742 digitizer. (a) Reconstruction of (u,v) coordinates from the physical coordinates of the center of the sixteen photodetectors and the charge collected by each of them. (b) CTR results for the sixteen pixels of the LYSO polished array coupled to Hamamatsu S13361-3050AE-04 MPPC at 58 V.

- ***time branch***: a balun transformer connected to a cascade of two RF amplifiers (monolithic microwave integrated circuits (MMICs)) that extract a highly amplified, fast, and high bandwidth signal. The analog time signal is then fed to a fast double-edge discriminator integrated into the board that extracts with high precision two fast digital signals containing in its leading edge the time information of the crossing point between the analog time signal and a fixed external threshold.
- ***energy branch***: a low-power operational amplifier with unit gain for energy quantification.

Moreover, ***a global energy signal***, obtained from the sum of all the 16 energy signals of the SiPMs, is extracted.

The double-edge discriminator is used to set two distinct fixed thresholds on the leading edge of the analog time signal and measure the time interval between the two crossing points. This measurement is particularly useful in cases where the extracted time signals present a strong time walk and hence a rise time correction of the timestamp is needed. However, the double-edge discriminator was not functioning properly, as the use of two discriminators created problems in the stability of the signals in this version of the prototype readout, and only one threshold could be applied to the analog timing signal.

The schematic of the board is illustrated in Figure 6.1 and the picture of the board is presented in Figure 6.5a. The board has ten subminiature version A connectors:

- V_{S+}, V_{fast}, V_{ref} to power the energy branch.
- $V_{global\ energy}$ to power the global energy branch and $E_{global\ energy}$ to extract the global energy output.

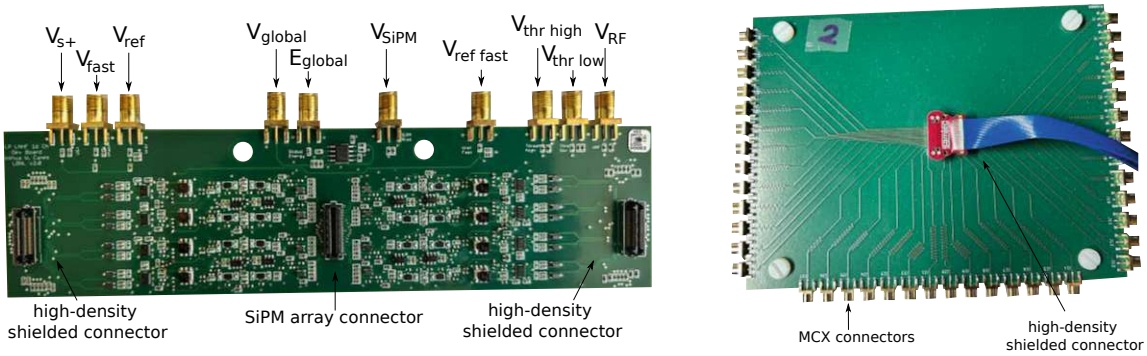

(a) (b)

Figure 6.5: (a) Picture of the sixteen-channel LPLNHF electronics readout board. (b) Picture of the breakout board.

- V_{SiPM} to power the SiPM array
- $V_{ref\ fast}$, $V_{thr\ high}$, $V_{thr\ low}$, V_{RF} to power the time branch.

A pair of high-density shielded Samtec cables are connected on the right and left sides of the board (Figure 6.5a) and are used to transfer the board output signals, consisting of one analog energy signal, an analog time signal and two equal digital time signals (one positive and one negative) for each channel, to two breakout boards (Figure 6.5b). Each board splits the output signals coming from the high-density cable and directs them to the MCX edge-mounted connectors, which are then individually fed to the V1742 CAEN digitizer boards via MCX-MCX cables.

6.2.1 Measurement set-up

The LPLNHF development board is fixed on a set of two orthogonal motorized linear stages (Zaber, X-LHM series) with micrometric precision to properly align the detector module for the coincidence measurements. A Python script was written to remotely and precisely control the stages and hence the board position via software. 3D printed holders shown in Figure 6.6 are designed to fix the board to the set of linear stages, one to hold the board vertically to perform a frontal irradiation of the detector module and one for the lateral irradiation of the detector module, in which the board is held horizontally. In the design, it was ensured that there was no contact between the holders and the electronic circuits of the readout board. Moreover, with respect to the set-up described in section 4.1.5, a power supply is monitored through a Python script to control the threshold set for the discriminator via software.

The global energy output is used to generate a trigger for the acquisition as described in Section 4.1.5. The ***analog energy signals*** are fed to one of two CAEN V1742 digitizers of Figure 4.6 via the MCX-MCX cables using a frequency of 2.5 GS/s (1024 points, 400 ps apart) and integrated over the entire range after evaluation and subtraction of the baseline, as shown in Figure 6.7a. The amplitude of the pulse is also saved. The positive ***digital time signals*** are fed to the second CAEN V1742

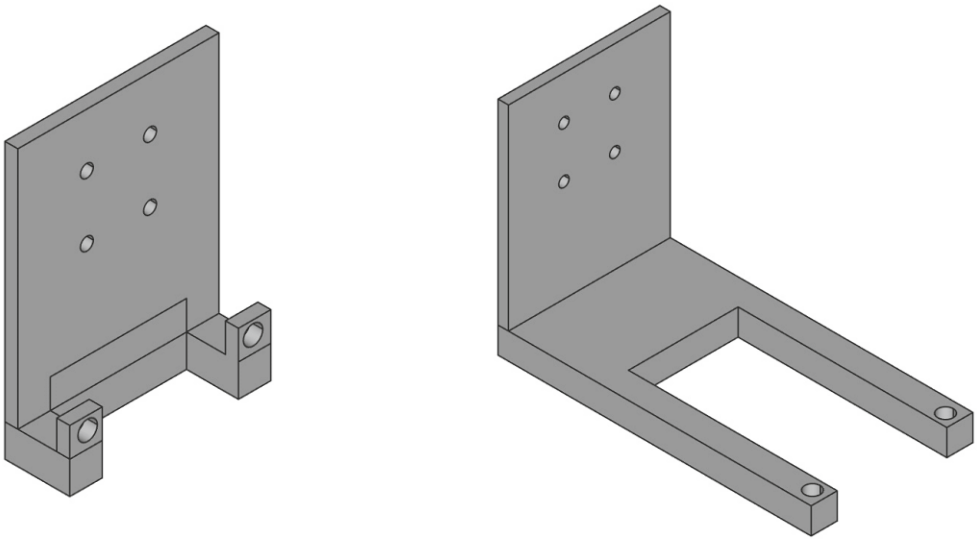

(a) (b)

Figure 6.6: Design of the 3D printed holder for the (a) front irradiation and (b) lateral irradiation of the sixteen-channel LPLNHF electronics readout board.

digitizer, set at 5 GS/s frequency (1024 points, 200 ps apart). The timestamp is extracted by evaluating online the crossing point between a fixed threshold and the linear interpolation of the leading edge of the signal, as shown in Figure 6.7b.

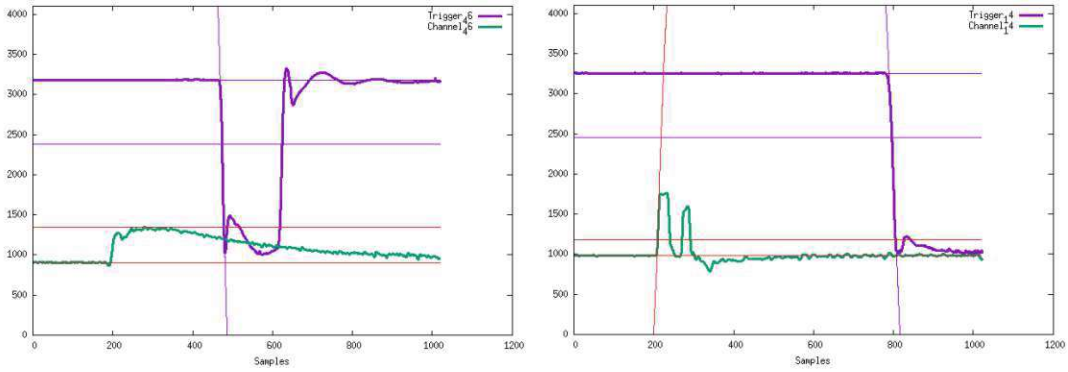

(a) Positive analog energy signal (b) Positive time digital signal

Figure 6.7: Digitalization of the energy and time signals (in green) of the sixteen-channel LPLNHF electronics readout board using two CAEN V1742 digitizers. In purple, the common trigger signal is visualized.

6.2.2 Energy calibration

To be able to make the response of the SiPM linear with respect to the deposited energy and to evaluate and compensate for the different gains of each SiPM, energy calibration is needed. The linearity study of the system was performed channel by channel using a single Teflon-wrapped LYSO:Ce polished crystal identical to those of the standard module and subsequently coupling the crystal to each SiPM of the array. In particular, the response function of each channel of the detection system was obtained using various characteristic X-rays and gamma rays from radioactive sources, in the energy range between 31 and 1274 keV, and measuring the integrated charge for photopeak events. The used sources with the relative energies are: ^{133}**Ba**: 30.85, 81, 302.85 and 356.02 keV; ^{57}**Co**: 122 keV; ^{176}**Lu**: 56 keV; ^{22}**Na**: 170.33 (backscatter peak of 511 keV), 511, 1274.5 keV; ^{137}**Cs**: 184.33 (backscatter peak), 661.7 keV. The saturation effect that is expected due to the limited number of SPADs of each SiPM can be derived from Equation 3.14 as

$$y = a \cdot (1 - e^{-x \cdot \frac{b}{a}}) \tag{6.3}$$

Figure 6.8 shows the response function measured for a single channel and the interpolation using Equation 6.3 in green. The high saturation visible for the 511 keV gamma rays is expected considering the high light yield of LYSO:Ce (41000 ph/MeV, see Table 3.1), high PDE of 0.63 for the MT SiPM array used [74], and the limited number of SPADs of each SiPM (around 8000). However, when an energy range up to 1274 keV is considered, the measured response function cannot be simply described by the exponential function of Equation 6.3. In fact, the SPADs can recharge and, after a certain recovery time, they are ready to detect another photon (55 ns in the case of the Broadcom NUV-MT array [74]). The possibility for SPADs of detecting more than a single photon during the scintillation emission becomes more relevant for higher energies, because of the higher number of photons in the queue of the pulse.

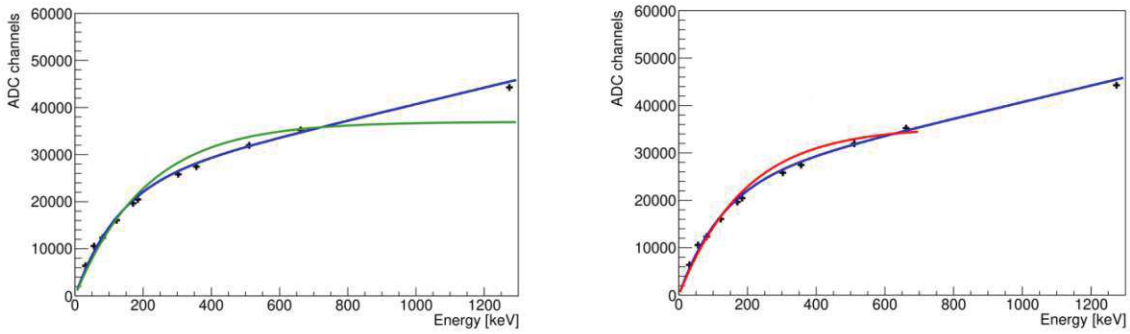

Figure 6.8: Measured response function at different energies of a single channel of the standard module readout by the LPLNHF electronics. Left: fit up to 1274 keV with function 6.3 (green line) and with the same function plus a linear term (Equation 6.4, blue line). Right: the red line shows the interpolation of the data up to 662 keV with the simple exponential function (Equation 6.3).

Modifying the expected exponential behavior of Equation 6.3 with the addition of a linear term, the following function is obtained

$$y = a \cdot (1 - e^{-x \cdot \frac{b}{a}}) + c \cdot x \tag{6.4}$$

This function provides a better fit to the data than the simple exponential model (as shown by the blue line in Figure 6.8). However, Equation 6.4 is not analytically invertible, and small discrepancies are observed when fitting with the two different functions up to 511 keV, which is the energy range of interest. Therefore interpolation is performed with the simple exponential function. This is repeated for all the channels and the parameters a and b are extracted from each fit and used to linearize the response function.

6.2.3 Standard module

Using the standard module coupled to the Broadcom NUV-MT array, bias voltage and threshold scans are performed. The lowest applicable threshold is 45 mV, below which the signal becomes unstable. Figure 6.9a shows the reconstruction of the (u,v) coordinates from the physical coordinates of the center of the sixteen photodetectors and the charge collected by each of them. An improvement in resolution compared to Figure 6.4a is noticeable. Figure 6.9b displays the mean CTR for the four central channels as a function of the bias voltage and threshold. A minimum value of 124 ± 3 ps at a bias voltage of 45 V and a threshold of 60 mV is obtained. Under this optimal configuration, an average energy resolution of 8.2 ± 0.2 % FWHM is achieved.

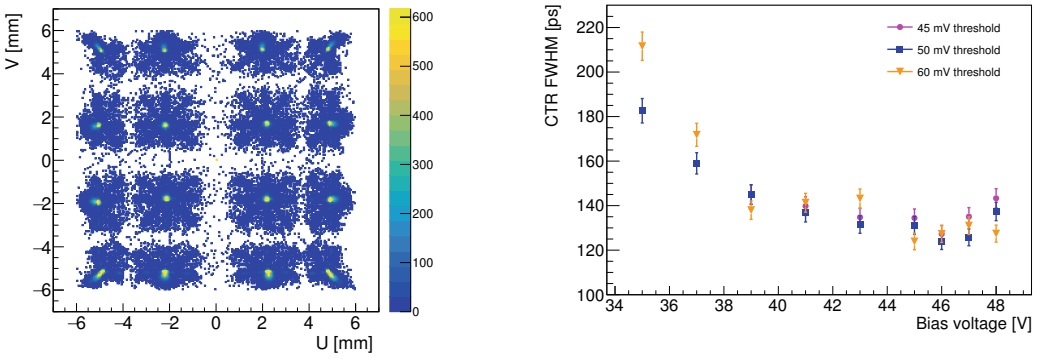

(a) (b)

Figure 6.9: Results obtained for the standard module coupled to the Broadcom NUV-MT array and readout by the LPLNHF development board and the CAEN V1742 digitizer. (a) Reconstruction of (u,v) coordinates from the physical coordinates of the center of the sixteen photodetectors and the charge collected by each of them. (b) CTR values (average on the 4 central crystals) as a function of the SiPM array bias voltage for three different discriminator thresholds.

6.2.4 DOI-capable module

The performance of the DOI-capable module is evaluated at the optimal configurations of bias voltage and discriminator threshold, respectively 45 V and 60 mV, as determined in the study of the standard module. Under these conditions, the average energy achieved for the four central channels is 9.7 ± 0.4 %. The CTR obtained before (CTR_{std}) and after ($CTR_{DOI\,corr}$) timing correction are respectively 196 ± 6 ps FWHM and 146 ± 4 ps FWHM. Performing the lateral scan, a DOI resolution of 2.4 ± 0.2 mm FWHM is achieved on the four central crystals.

6.3 Discussion

Table 6.1 and 6.2 summarize the CTR, DOI and energy resolution results obtained using both standard and DOI-capable modules coupled to the Broadcom NUV-MT SiPM array. These tables provide a comparative analysis with the electronic systems discussed in previous chapters. While the energy and DOI resolution are only slightly improved, these results illustrate the benefits of using the HF concept for timing optimization. A clear trend of improved performance is observed as we progress from the PETsys TOFPET2 ASIC to the custom-made NINO 32-chip board, and finally to the sixteen-channel LPLNHF development board. With the latter, when utilizing the DOI-capable module, we initially recorded a CTR of 196 ± 6 ps. After timing optimization using the DOI information, we achieved a significant enhancement in time performance, bringing it below 150 ps. This improvement also coincided with a DOI resolution of 2.4 ± 0.2 mm. In the case of the standard module, the CTR values show a progressive improvement in timing resolution across the different electronic boards. Starting from 193 ps measured with the PETsys TOFPET2 ASIC, the CTR improves to 141 ps with the NINO 32-chip board, and further down to 124 ps with the LPLNHF board.

Table 6.1: Time resolution on the four central channels using the standard and DOI-capable modules, coupled to the Broadcom NUV-MT array and readout using the LPLNHF development board. Comparison with NINO 32-chip board and PETsys TOFPET2 ASIC.

	DOI-capable module			std module
Electronic readout	CTR_{std}	CTR_{corr}	DOI res.	CTR_{std}
PETsys TOFPET2 ASIC	291 ± 6 ps	216 ± 6 ps	2.6 ± 0.2	193 ± 6 ps
NINO 32-chip board	247 ± 7 ps	170 ± 5 ps	2.5 ± 0.2	141 ± 4 ps
LPLNHF development board	**196 ± 6 ps**	**146 ± 4 ps**	**2.4 ± 0.2**	**124 ± 3 ps**

Table 6.2: Energy resolution on the four central channels using the standard and DOI-capable modules, coupled to the Broadcom NUV-MT array and readout using the LPLNHF development board. Comparison with NINO 32-chip board and PETsys TOFPET2 ASIC.

	DOI-capable module	std module
Electronic readout	En. res [%]	En. res [%]
PETsys TOFPET2 ASIC	9.6 ± 0.5	9.5 ± 0.4 ps
NINO 32-chip board	9.8 ± 0.4	8.7 ± 0.3 ps
LPLNHF development board	**9.7 ± 0.4**	**8.2 ± 0.2 ps**

6.4 Summary and conclusion

The use of the LPLNHF development board shows notable improvements in the readout of LYSO:Ce scintillators compared to other electronic readouts and represents a significant step towards the achievement of a CTR in the order of 100 ps FWHM in TOF-PET detectors, applicable to both standard and DOI-capable detectors. These promising results also highlight the potential of multichannel HF electronics for future applications using different scintillation materials. This readout allows the exploration of fast light production mechanisms thanks to the ability to lower the leading edge detection threshold and utilize the fastest photons produced, such as Cherenkov emission in BGO and rapid scintillation in plastic. Furthermore, the excellent timing resolution allows the distinction between different light production processes within the same material. For instance, it enables the differentiation between slow scintillation and fast Cherenkov emission in BGO. Additionally, the good energy resolution helps identify energy deposition in different materials, thereby enabling event classification in Heterostructures composed of alternating layers of various materials. However, the current design of the board has limitations, particularly regarding the threshold value, which cannot be set below 45 mV. While the performance of LYSO:Ce scintillators does not significantly depend on this threshold, BGO scintillators require an optimal threshold of around 10 mV for improved performance.

This chapter has accurately evaluated both the advantages and limitations of the LPLNHF board, highlighting the necessity for enhancements in the timing branch of the electronic design. As a result, a new, versatile electronic board has been developed to meet the specific requirements of various scintillation crystals. This new design is introduced in the next chapter, aiming to provide the flexibility needed for a broader range of applications.

7 Optimization of Low-power Low-noise High-frequency electronics for novel material application

The achievement of a time resolution towards 10 ps FWHM in TOF-PET would represent a paradigm shift, as it would not only improve image quality and reduce the delivered doses but would also pave the way towards reconstruction-less image production. In fact, with a CTR of 10 ps, the precision in the localization of the annihilation point would be equal to the positron range in matter for FDG, which represents the intrinsic limit to the achievable spatial resolution of the reconstructed image. A challenge has been launched to push research towards this goal [62]. Nonetheless, the achievement of 10 ps is proved to be quite challenging as it requires optimization of all the components of the detection chain. Given the improvements in photodetectors and readout electronics, the major limitation is now represented by the stochastic process of light emission. Current research is actively exploring strategies to exploit the prompt photon emission processes, such as Cherenkov photons [75, 76, 64], cross-luminescence, hot-intraband luminescence, to improve the overall time resolution of PET detectors. The common drawback of these light emission mechanisms is the low associated light yield, which affects both the time and energy resolution. One possible solution is to incorporate a material that guarantees fast emission or high light output in a detector that also includes another material that provides the missing properties, i.e. stopping

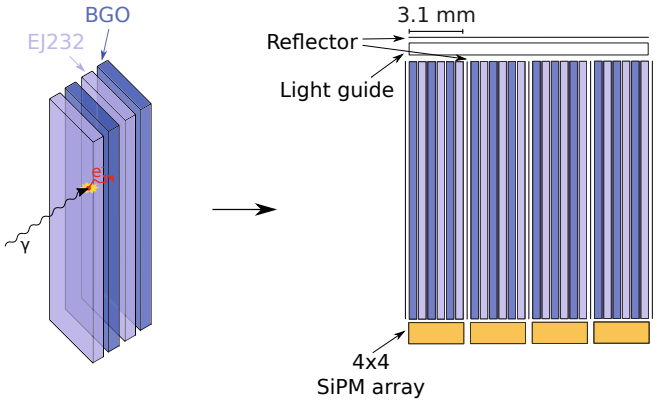

Figure 7.1: Schematic of a heterostructure pixel and a DOI-capable module made of sixteen heterostructured scintillators.

power, in a so-called heterostructure [77, 6], illustrated in Figure 7.1. The concept of heterostructure is intrinsically based on a layered structure. The stratification of thin plates of materials worsens the light transport inside these structures, degrading their timing properties. On the other hand, the impaired transport of light can be exploited to recover the DOI information [78] and correct for the induced bias in timing using the light recirculation mechanism between single pixels as illustrated in the previous chapters.

The development of the multi-channel HF readout allows us to investigate for the first time the performance achievable with matrices of heterostructures. This chapter presents the results obtained with the last version of the sixteen-channels board. Section 7.1 describes the heterostructured scintillator concept, the energy sharing and DOI evaluation enabled in such configuration. Section 7.2 presents the upgrades of the electronics and experimental set-up compared to the work described in the previous chapter. Section 7.3 describes the results obtained with different materials, including a heterostructured scintillator matrix. Finally, Sections 7.4 and 7.5 present the discussion and conclusion.

7.1 New detector concept: Heterostructures

Heterostructured scintillators combine two or more materials with distinct properties, used to exploit the advantages of each component. In particular, BGO can be used for efficient stopping power for gamma rays at 511 keV and plastic EJ232 for the high photon density (Figure 7.1). The principle at the basis of the concept of heterostructures is a mechanism of energy sharing between the two materials that are combined. When a material with high stopping power is combined with a fast but low-density one, the incident 511 keV gamma ray can be stopped by the photoelectric effect in the heavier material, but there is a non-negligible probability that the photoelectron will escape from it to the faster one, where it will deposit the remaining energy. The events in which energy sharing occurs are called *shared events*. This phenomenon becomes relevant when the thickness of the heavy material is comparable to the range of the recoil electron. The mechanism of energy sharing between the two materials allows for obtaining a fraction of fast events and the more energy is deposited in the faster material, the more fast photons are produced, achieving a better time performance [79] compared to the slow material itself.

The identification of the shared events can be performed via pulse shape discrimination [6, 79], as BGO and EJ232 have similar light yield between 8 and 10 ph/keV but different decay kinetics (the effective decay time of BGO is almost a factor 100 slower than EJ232 [80]), as highlighted in Table 3.1. Therefore, the pulse shape changes depending on how the deposited energy is distributed between the two materials, and the amplitude and integrated charge of the pulses proved to be two features allowing for clear pulse shape discrimination [6, 79]. Figure 7.2 shows the scatter plot of the integral versus the amplitude of the signals obtained for the case of one pixel of a Heterostructured matrix. In the plot on the left, all the events are shown. The events depositing

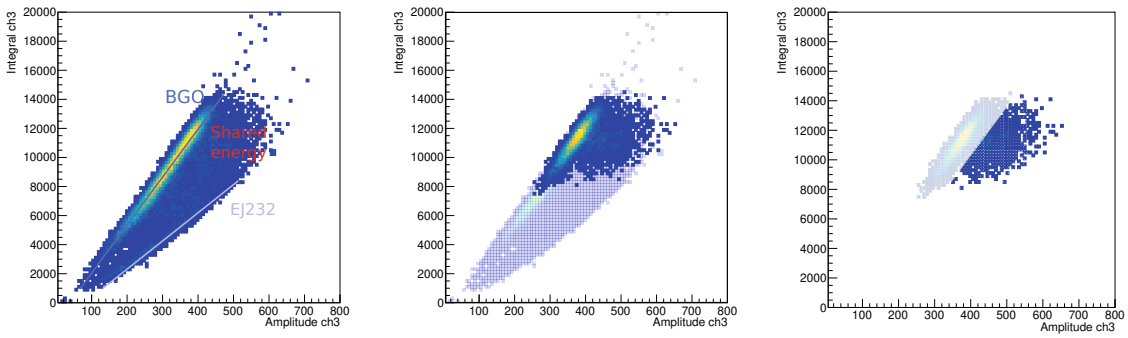

(a) All events (b) Photopeak events (c) Shared events

Figure 7.2: Example of a scatter plot of the integrated charge versus the amplitude for one pixel of the Heterostructured matrix. Events depositing energy in only one of the two materials (in this case BGO and the plastic scintillator EJ232) can be distinguished from those depositing energy in both materials (lying in the middle). (a) All events. (b) Events depositing 511 keV in the heterostructured pixel. (c) Shared photopeak events that deposit energy in both materials.

energy uniquely in BGO or EJ232 can be distinguished from the shared ones, that lie in the middle. Figure 7.2b highlights the events depositing the full 511 keV energy in the pixel (photopeak events) and Figure 7.2c only the events depositing energy in both materials (shared photopeak events).

Furthermore, the concept of heterostructure is intrinsically based on a stratification of thin layers, which worsens the light transport due to the attenuation of the light produced in it and degrades the energy and time properties. However, the attenuation is strongly correlated to the depth-of-interaction of the gamma and it can be exploited to retrieve its information and correct for the induced bias on the timing. The well-described mechanism of light sharing between neighboring crystals is therefore exploited by coupling the matrix to the light guide made of glass, which allows the recovery of the DOI information using a single-sided readout. In this case, attenuation is achieved by the layered structure instead of the depolishing of the lateral surfaces of the crystals.

7.2 Materials and Methods

7.2.1 Heterostructured pixels and matrices

Heterostructured pixels of 3x3x20 mm^3 are produced by CPI, made of alternated layers of BGO and EJ232 with a thickness of 250 μm each. Matrices are made of sixteen pixels separated from each other by foils of ESR (Figure 7.3a). One side of the matrix is coupled to the Broadcom NUV-MT array using a layer of 50 μm of OCA. The other side is coupled to the glass light guide using a layer of 150 μm of OCA (Figure 7.3b). As described in Table 3.1, the plastic scintillator EJ232 has a decay time below 2 ns, with

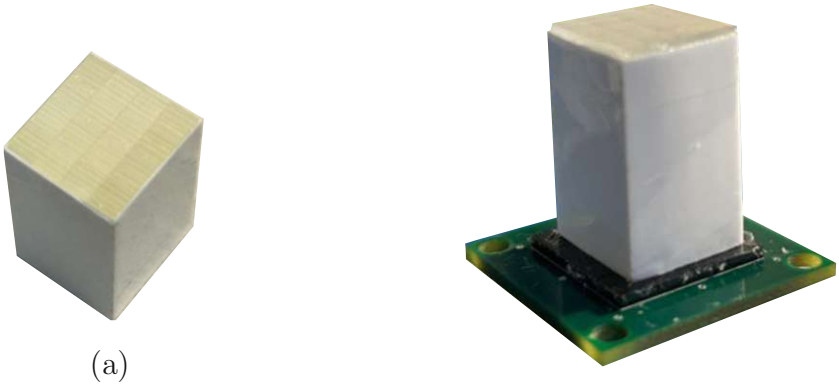

(a) (b)

Figure 7.3: (a) Picture of the heterostructures matrix wrapped in Teflon and (b) picture of the matrix coupled to the Broadcom MT SiPM array to one side and the light guide to the other.

a light yield of around 8400 ph/MeV, but a density of 1 g/cm^3. BGO has a density of 7.1 g/cm^3, a similar light yield (10700 ph/MeV), but a much slower decay time. A schematic representation of the heterostructured light-sharing module is shown in Figure 7.1.

7.2.2 LPLNHF electronics readout - version 3.0

The third and last version of the LPLNHF electronics readout board investigated improves the extraction of the time information using a fast single-edge discriminator that extracts with high precision a fast digital signal at very low thresholds (few mV). Therefore, similarly to the previous version, the output signal of each SiPM of the array is split and processed in parallel by two distinct branches:

- ***time branch***: the balun transformer connected to a cascade of two RF amplifiers. The analog time signal is then fed to a fast single-edge discriminator integrated into the board that extracts with high precision a fast digital signal containing in its leading edge the time information of the crossing point between the analog time signal and a fixed external threshold.
- ***energy branch***: a low-power operational amplifier with unit gain for energy quantification.

Finally, ***a global energy signal***, obtained from the sum of all the 16 energy signals of the SiPMs, is extracted. Figure 7.4 shows a picture of the board and the subMiniature version A (SMA) connectors used to power the board and the SiPM array and extract the signals. $V_{thr\ low}$ is the threshold on the leading edge employed to extract the digital time signal. Compared to the lower limit of 45 mV of $V_{thr\ low}$ for the previous version, this readout board allows extraction of the time information with thresholds as low as a few mV. If the performance of LYSO:Ce does not strongly depend on the threshold set, the time performance of BGO, plastic and therefore heterostructured scintillators,

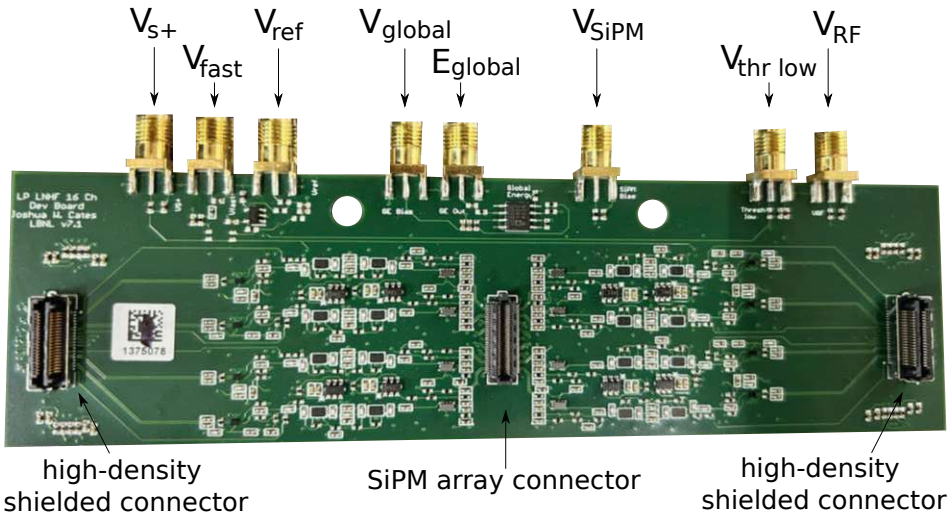

Figure 7.4: Picture of the last version of the sixteen-channel LPLNHF electronics readout board.

is strongly degraded at a high threshold level. This is due to the low number of fast photons produced. Setting a low threshold allows to make use of them, while the higher the threshold, the slower the photons used for timing estimation.

7.2.3 Digitizer Calibration

The two CAEN V1742 digitizers used for the acquisition and digitization of the signals are modules housing 32 channels and based on the use of 4 Switched Capacitor Array DRS4 chip (Domino Ring Sampler), one every 8 channels [81]. This technology relies on a series of 1024 capacitors (analog memory) in which the analog input signal is continuously sampled in a circular way. The sampling frequency is 5 GHz by default and it can be programmed to 2.5 GHz, 1 GHz, and 750 MHz. The analog-to-digital conversion is not simultaneous with the chip sampling phase, and it starts as soon as the trigger condition is met. When the trigger stops, the analog memory buffer is frozen, and the cell content is made available to the 12-bit ADC for digital conversion. The input dynamic range is 1 V.

The boards come pre-calibrated with a factory calibration that provides an intrinsic time resolution σ between 4 ps, when using channels of the same DRS4 chip, and 20 ps, when using channels of different DRS4 chips. The multi-channel board requires digitalization of at least 16 channels, thus making use of two or more groups. Therefore, the digitizer contributes to the final timing resolution with more than 50 ps FWHM. This contribution is not negligible if CTR values of about 100 ps are to be reached. Therefore, a custom calibration following the publication of D. A. Stricker-Shaver, S. Ritt and B. J. Pichler [82] is performed. In particular, two calibrations and one synchronization are needed:

- *Calibration of voltage offsets for each cell.* It is performed by injecting into each channel of the board a set of constant voltages (-0.3 V, 0 V, 0.3 V). For each cell,

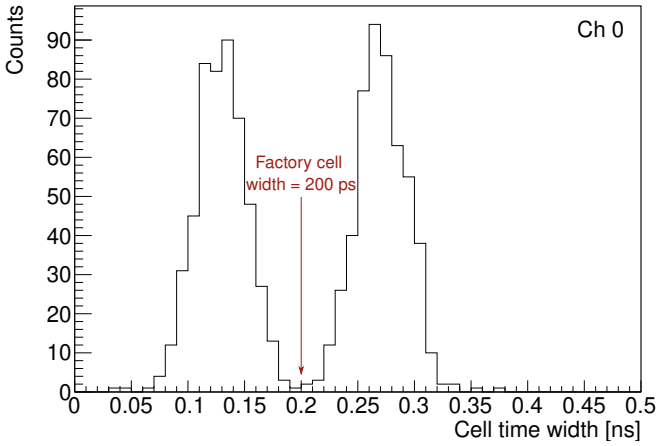

Figure 7.5: Example of distribution of the cell's time width for channel 0 of the first digitizer used compared to the cell's width fixed value used in the factory calibration. Odd and even cells have different time widths.

a linear fit of the voltage as a function of the average ADC counts is performed. The parameters of the fit provide the absolute voltage calibration, including offset correction.

- *Calibration of time width of each cell.* To measure the effective time width of every cell, a 50 MHz sinusoidal waveform is injected in each channel. The voltage difference between adjacent cells is measured, which is proportional to the time difference between the cells. This is because, approximately, the voltage increase (or decrease) is nearly linear at the center of the waveforms. By averaging the voltage difference between adjacent cells over many events and normalizing the sum of all 1024 cell widths to one readout period (204.8 ns), an absolute calibration of the time difference between all adjacent cells can be obtained. While the factory calibration assumes a fixed cell width of 200 ps, odd and even cells in each channel exhibit significantly different time widths (Figure 7.5). In addition to cell-by-cell time calibration, injecting a 100 MHz sinusoidal waveform into the DRS4 channels allows for the measurement of the time difference between zero crossings over one or multiple periods. This difference is then used to correct the time widths of all intermediate cells.

- *Synchronization of the 4 DRS4 chips.* Injecting a sinusoidal waveform at 100 MHz into one channel of each group allows to perform a time synchronization of the different DRS4 chips on the board. By sacrificing 4 channels out of the total 32, optimal time precision can be achieved across the remaining 28 channels.

As a result of this dedicated calibration, an intrinsic time resolution σ below 6 ps is achieved between channels, both within the same digitizer and across different DRS4 chips.

7.3 Results

Pixels made of different materials are measured using the LPLNHF electronic board. Next, 20 mm LYSO:Ce matrices are tested in both standard and DOI configurations. Finally, the board is used to measure matrices of heterostructures, utilizing the light-sharing method to retrieve the DOI information, which is then employed to enhance the timing resolution.

7.3.1 LYSO:Ce, BGO, EJ232 and Heterostructure Pixels

Pixels of various materials and sizes, including LYSO:Ce, BGO, EJ232 and Heterostructured scintillators are tested by coupling them to a single channel of the Broadcom NUV-MT array using Meltmount grease. The results are summarised in Table 7.1 and represent the best achievable time resolution, as degradation is expected when measuring a matrix, due to light dispersion. Additionally, as described in Section 6.2.2, a 3.6x3.6x20 mm^3 LYSO:Ce pixel, wrapped in Teflon, is used to measure the response function of each SiPM of the array, using sources of different energies. These response functions are used to linearize the SiPMs output.

Table 7.1: Timing resolution results using pixels coupled to one channel of the Broadcom NUV-MT array and readout using the LPLNHF development board.

Material	producer	geometry [mm^3]	CTR [ps] FWHM
LYSO:Ce	CPI	3x3x15	115 ± 4 ps
LYSO:Ce	CPI	3x3x20	125 ± 4 ps
LYSO:Ce	CPI	3.6x3.7x20	130 ± 4 ps
EJ232	CPI	3x3x20	94 ± 2 ps
BGO	EPIC	3x3x20	192 ± 5 ps
Heterosctructure	EPIC	3x3x20	262 ± 8 ps
only shared events			159 ± 5 ps

7.3.2 Matrices of LYSO:Ce

Standard and DOI-capable matrices made of pixels of LYSO:Ce are measured. The geometry of the pixels enables perfect one-to-one matching between the crystals and the SiPMs. Both the crystals and the active areas of the SiPMs measure 3.6x3.7x20 mm^3, with a pitch of 4 mm between SiPMs. ESR is placed between the crystals to act as a reflector and align with the dead areas of the SiPM. This results in a total crystal matrix dimension of 16x16x20 mm^3. Meltmount is used to couple the crystals with the SiPM array, and in the light-sharing module, to couple the crystals with the light guide. A final layer of ESR was placed on top. The results obtained from the matrices of LYSO:Ce are summarized in Table 7.2. At the optimal bias voltage of 45 V and discriminator threshold of 20 mV, the timing performance of the DOI-capable module on the central channels, after DOI correction, is 133 ± 2 ps FWHM. The result is in

Table 7.2: Timing and DOI resolutions in FWHM using matrices of LYSO:Ce coupled to the Broadcom NUV-MT array and readout using the LPLNHF development board. A bias voltage of 45 V and a threshold of 20 mV are used.

	DOI-capable module			std module
Crystals	CTR_{std} [ps]	CTR_{corr} [ps]	DOI res. [mm]	CTR_{std} [ps]
all	189 ± 2	140 ± 2	2.7 ± 0.2	131 ± 2
central	195 ± 2	**133 ± 2**	**2.2 ± 0.2**	**130 ± 2**

agreement with the 130 ± 2 ps FWHM obtained with the standard module, as well as the 130 ± 4 ps FWHM measured using a single 3.6x3.7x20 mm^3 LYSO:Ce crystal. Additionally, the DOI-capable module achieves a DOI resolution of 2.7 ± 0.2 mm FWHM.

7.3.3 Matrices of Heterostructures

Matrices of Heterostructured scintillators are finally measured. The comparison between the reconstructed (u,v) coordinated for the LYSO:Ce and Heterostructures matrices is shown in Figure 7.6. For each pixel of the heterostructured DOI-capable module, the CTR is evaluated both before and after the DOI correction for two distinct selections of events: first selecting all the photopeak events (shown in Figure 7.2b) and then selecting only those depositing energy in both materials (shared photopeak events in Figure 7.2c). Table 7.3 reports the results obtained.

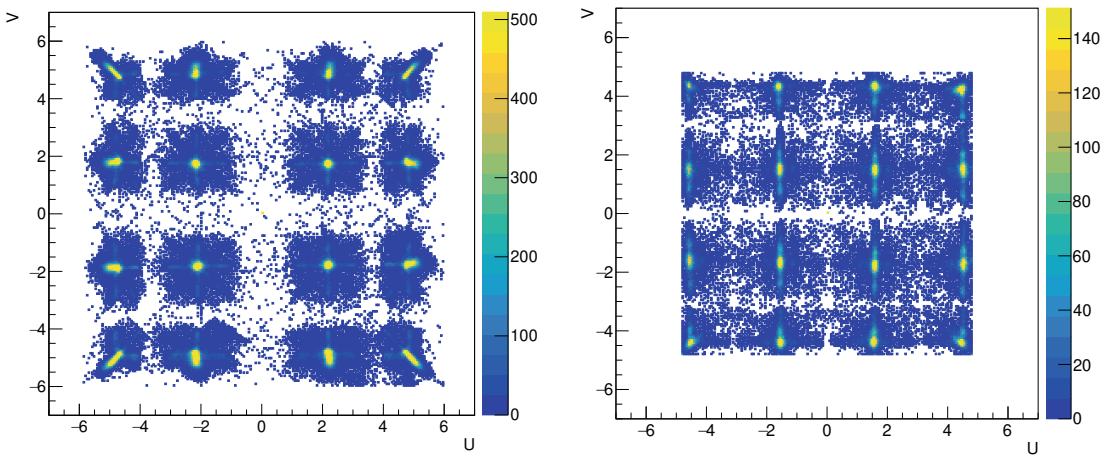

(a) LYSO:Ce depolished matrix using the light-sharing principle

(b) Heterostructures matrix using the light-sharing principle

Figure 7.6: Reconstruction of (u,v) coordinates from the physical coordinates of the center of the sixteen photodetectors and the charge collected by each of them.

Table 7.3: Timing resolution results on the central channels in FWHM using matrices of heterostructures coupled to the Broadcom NUV-MT array and readout using the LPLNHF development board. A bias voltage of 45 V and a threshold of 10 mV are used.

Events	CTR_{std} [ps]	CTR_{corr} [ps]
All photopeak	290 ± 11	270 ± 9
Shared photopeak	194 ± 8	182 ± 6

7.4 Discussion

The last version of the LPLNHF development board allows for setting a threshold as low as a few mV on the analog timing signal to extract a fast digital signal. This enables the exploitation not only the fast scintillation of LYSO:Ce and EJ232, but also the even faster production of Cherenkov photons in BGO. The board, tested with pixels of various materials, achieves state-of-the-art results in terms of timing resolution compared to results obtained using single-channel readout boards [7, 61] and other multi-channel HF readout developments [83]. In particular, timing resolutions as low as 130 ps are achieved with 20 mm long LYSO:Ce matrices that are one-to-one coupled to the SiPM array, for both the standard and DOI-capable modules. Additionally, the DOI-capable modules provide depth-of-interaction (DOI) information with a resolution of sub-3 mm. These results are highly competitive with the current performance of available PET scanners, although not yet scalable to a full system. However, integrating these electronics into commercially available TDCs could enable scalability to a larger number of channels. Table 7.4 summarizes the best CTR results achieved through the progressive improvements of the sixteen-channel development board presented in this chapter and the previous one.

Table 7.4: Time resolution results on the central channels using the standard and DOI-capable module readout using the various versions of the sixteen-channel HF development boards.

		DOI-capable module		std module
Board version	crystals	CTR_{std}	CTR_{corr}	CTR_{std}
LNHF - v.1.0	15 mm LYSO:Ce	-	-	150 ± 3 ps
LPLNHF - v.2.0	15 mm LYSO:Ce	196 ± 6 ps	146 ± 4 ps	124 ± 3 ps
LPLNHF - v.3.0	20 mm LYSO:Ce	195 ± 2 ps	133 ± 2 ps	130 ± 2 ps
	20 mm Heterostructure	194 ± 8 ps	182 ± 6 ps	-

Furthermore, the concept of heterostructured scintillators is explored, observing energy sharing between the two combined materials. By selecting shared events, it is possible to enhance the time resolution compared to using all photopeak events or bulk BGO. Although the heterostructures presented do not yet achieve the same timing performance of pure LYSO, they offer a cost-effective compromise between good timing resolution and high sensitivity. Incorporating heterostructures into a matrix with the

light-sharing principle also allows for the extraction of DOI information, which can be used both for timing and spatial correction. Faster materials can be combined to achieve better timing performance. For example, BGO with BaF_2 [84], or LYSO:Ce, GAGG:Mg or BGO with nanomaterials [85].

7.5 Summary and conclusion

The LPLNHF development board demonstrates state-of-the-art performance with the well-known LYSO:Ce scintillation emission. The DOI-capable concept achieves the same time performance of 131 ± 2 ps as the standard configuration, with the added advantage of retrieving the DOI information with 2.7 ±0.2 mm, which can be used to correct parallax errors in scanners. Furthermore, the concept of a heterostructured scintillator, extensively studied in single- and double-side readout [6, 86], is tested for the first time in a multi-channel set-up using the light-sharing principle. The combination of BGO and EJ232 represents a proof of concept and combinations of faster materials that can achieve improved time resolutions are being investigated in several studies [85, 79], showing promising results when used with this type of readout. These measurements demonstrate the potential of HF multi-channel electronics in the readout of materials with fast light emissions. Further studies are planned to investigate matrices composed of BGO, plastic, and combinations of these materials with faster alternatives, as well as the use of active light guides that generate scintillation.

IV

An innovative method to solve the inter-crystal scattering kinematics

8 An innovative method to solve the inter-crystal scattering kinematics

To achieve high spatial resolution, commercial PET scanners often utilize detectors based on pixellated crystals with a shared readout. In this configuration, over half of the total coincidence events deposit energy in two or more crystals [8], Inter-Crystal Scatter (ICS) events (Figure 8.1). These events, if not properly addressed, can degrade spatial resolution due to the mispositioning of the crystal of first interaction. Various approaches have already been investigated to address this problem: discarding of ICS events, selection of the crystal of first interaction with a dedicated algorithm [87, 88], inclusion of multiple LORs in the reconstruction process, and use of dedicated geometry or readout. Using the DOI-capable detector concept, this chapter presents a new algorithm to evaluate the temporal sequences of gamma interactions in the crystals and the most likely impact positions, removing the ambiguity in determining the true LOR.

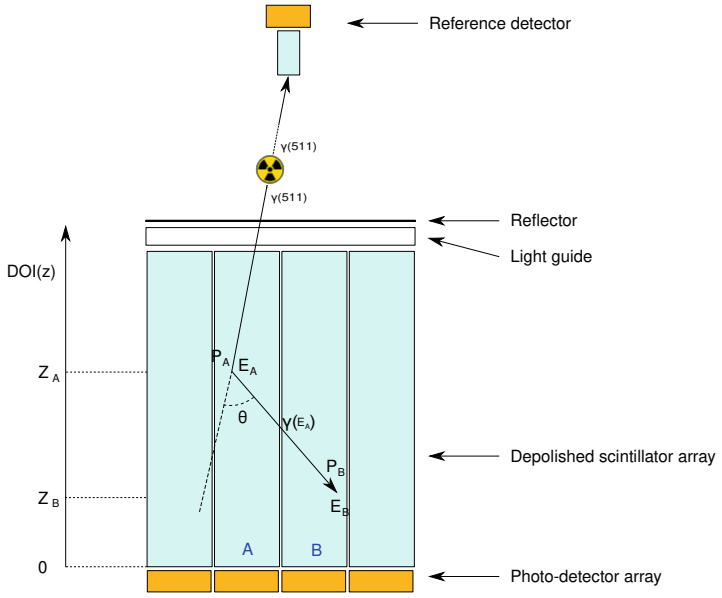

Figure 8.1: Representation of the inter-crystal scattering (ICS) problem using the light-sharing PET module configuration.

Section 8.1 introduces the inter-crystal scattering problem and presents the proposed method to address it, along with an overview of the simulated set-up used for validation. Section 8.2 summarizes and discusses the results obtained, while conclusions are drawn in Section 8.3.

8.1 Materials and Methods

8.1.1 Light-sharing detector configuration

The configuration of the PET detector module used in this study is extensively described in Section 4.1. It consists of a 4x4 matrix of 3.1x3.1x15 mm^3 LYSO:Ce depolished scintillators, separated by foils of ESR. One side of the matrix is coupled to a 4x4 SiPM array, while the other side is coupled to a glass light guide. An additional layer of ESR is placed on top of the light guide to reflect light back into the matrix, promoting light recirculation throughout the module [66].

8.1.2 Inter-Crystal scattering

Inter-Crystal Scatter (ICS) events occur when a gamma ray deposits its energy across two or more crystals. They are sometimes discarded since, if not properly addressed, they can degrade the spatial resolution due to the uncertainty in determining the crystal where the first interaction occurred [8]. However, excluding ICS events results in a loss of sensitivity. Several methods for addressing ICS events have been explored in the literature. These include the use of multiple crystals where the gamma interacts to generate different LORs that are then incorporated into the reconstruction process [89]. Otherwise, algorithms can be employed to identify the crystal of the first interaction based, for example, on the Compton Kinematics ([87]) or the Klein-Nishina cross-section ([88]). Alternatively, dedicated detector designs can be developed specifically to resolve ICS events [90].

This work, making use of the pixellated detector with the light-sharing mechanism, presents an algorithm to evaluate the temporal sequences of gamma interactions in the crystals making use of the Compton kinematics and probability of interaction as a function of the scattering angle. The algorithm evaluates the most likely impact positions, thus removing the ambiguity in the determination of the LOR [91].

The ICS problem is illustrated in Figure 8.1. A 511 KeV gamma ray produced in positron annihilation undergoes a Compton scattering in crystal A, with a Compton angle θ, depositing energy E_A in point P_A. The scattered photon travels until crystal B, where it deposits all its energy E_B in P_B, by photoelectric interaction. Solving the ICS problem consists in determining the impact positions P_A and P_B and the temporal order of the interaction, i.e. which crystal between A and B is hit first. The proposed method considers the interactions in A and B separately, superimposes their expected signals on the SiPM array, compares the result to the signals observed, and calculates

the most probable impact sequence from the cross-sections of the physical processes involved.

8.1.3 Method definition

Calibration of the detector module

To calibrate the detector module, each crystal n of the matrix is irradiated head-on using a spot size smaller than the area of a single pixel. For each measurement, the dataset is filtered to accept only events with energy deposition confined in the irradiated crystal n, using the same procedure employed to isolate gamma rays depositing energy in a single scintillator and described in Section 4.2.1. The relation between w and z is then derived as outlined in the same Section 4.2.1. For each SiPM k, the distribution of the charge q_k^n recorded by each SiPM is plotted against the extracted DOI information z and the energy E deposited by the gamma-ray, resulting in a 3D distribution similar to the one illustrated in Figure 8.2. E is derived from the sum of the charges measured by all the photodetectors. The sixteen 3D distributions are fitted with a plane function to obtain the $D_k^n(z, E)$ calibration maps

$$D_k^n(z, E) = p_0 + p_1 \cdot z + p_2 \cdot E \tag{8.1}$$

The process is repeated for each crystal n and, at the end of the procedure, a total of 16x16 calibration maps are available, representing the expected charge seen by the sixteen SiPMs when each one of them is separately irradiated.

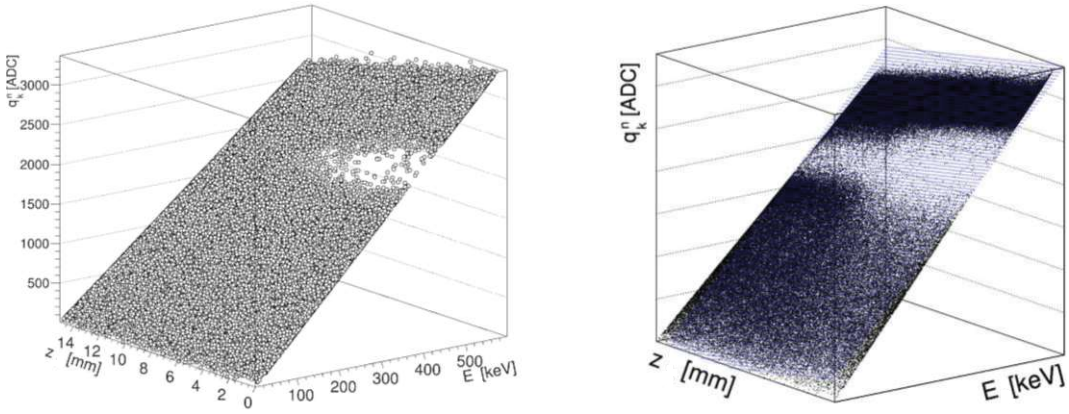

(a) (b)

Figure 8.2: (a) Representation of the distribution of the charge q_k^n recorded by a SiPM k plotted against the DOI information z and the energy E deposited by the gamma rays when a crystal n of the array is irradiated. (b) The $D_k^n(z, E)$ calibration map interpolating the data is shown in blu.

Selection of ICS events

The same procedure employed to isolate gamma rays depositing energy in a single scintillator is used to perform the selection of ICS events. The accumulation volumes identified and separated using the custom clustering algorithm correspond to events for which the energy deposition is confined to an individual scintillator. Based on the same principle, inter-crystal scatter events are the ones reconstructed in the areas between pairs of accumulation volumes. An example is given in Figure 8.3, where one crystal only of the detector array is irradiated.

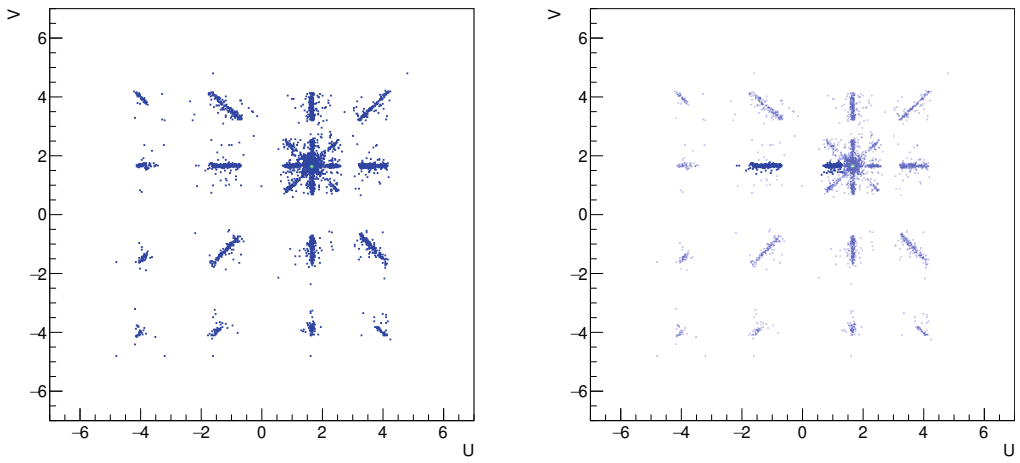

(a) (b)

Figure 8.3: (a) Reconstruction of (u,v) coordinates from the front irradiation of one of the pixels of the detector array. (b) Selection of one type of ICS event where the gamma interacted through Compton scattering in one crystal and then photoelectric interaction in a second one.

Determination of the impact points

After the calibration procedure and the isolation of ICS events between a pair of crystals A and B, two cases are analyzed separately: Compton scattering in crystal A followed by photoelectric absorption in crystal B ($\Lambda_{A\to B}$) or the opposite $\Lambda_{B\to A}$. In both cases, a series of theoretical interaction points are chosen in crystal A (z_A^h), and the same is done for crystal B (z_B^r), as illustrated in Figure 8.4. All the possible combinations $\varphi_{h,r} = (z_A^h, z_B^r)$ of interaction points for the ICS event are considered. For each point, the event kinematics is completely determined. The scattering angle θ is computed from the position of the source and z_A^h and z_B^r. From the Compton scattering formula, the energy of the scattered photon 511 keV$/(2 - cos(\theta))$ and therefore the energies E_A and E_B ($E_A + E_B = 511$ keV) deposited in z_A and z_B are computed.

For each SiPM k, the total expected signal q_k is the sum of the contribution due to the interaction in crystal A and crystal B and can be obtained from the calibration

maps $D_k^n(z, E)$

$$q_k(z_A^h, z_B^r) = q_k^A + q_k^B = D_k^A(z_A^h, E_A^h) + D_k^B(z_B^r, E_B^r) \tag{8.2}$$

This is compared to the actual p_k charges measured [91]:

$$\chi^2 = \sum_{k=1}^{K} \frac{(p_k - q_k)^2}{q_k} \tag{8.3}$$

The best estimation of the DOI positions is then found by selecting the $\varphi_{h,r}$ that minimizes χ^2. The ambiguity in the temporal sequence is solved by computing the probability of $\Lambda_{A\to B}$ and $\Lambda_{B\to A}$ on the basis of the physical processes involved in the ICS and the Λ hypothesis with the highest probability is then selected as the result of the method. The probability of each Λ is calculated as

$$P_\Lambda = P_{l_0} \times P_C \times P_{l_1} \times P_{PE} \times P_q \tag{8.4}$$

where P_{l_0} is the probability for a 511 KeV photon to reach the first interaction point, P_C the probability of a Compton scatter with angle θ to undergo in the first point, P_{l_1} the probability for the photon arising from Compton scatter to reach the second interaction point, P_{PE} is the probability for a photoelectric interaction in the second point. Finally, P_q is the probability of measuring the integrated charges p_k, given the theoretical values q_k derived in the previous step.

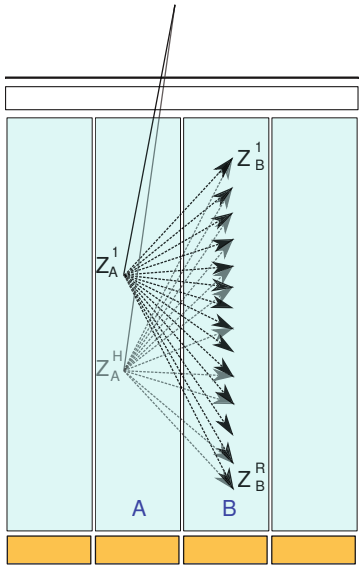

Figure 8.4: Representation of the procedure used to find the most likely impact point z_A^h and z_B^r. Considering crystal A as the first crystal of interaction, a series of possible interaction points is considered on crystal A and associated with a similar series of points on crystal B. Then the same procedure is repeated considering crystal B first.

8.1.4 Method validation

The effectiveness of the proposed method is validated through Monte-Carlo simulations performed using the Geant4 toolkit [92]. The experimental setup is simulated taking into account the composition of the crystals, their surface state, the optical coupling materials, the reflectors, and the silicon photodetectors, as displayed in Figure 8.5a. The electrons and optical photons produced by the interaction of primary gamma rays are tracked (Figure 8.5b) and the position of each energy deposition is recorded, as well as the amount of energy deposited. Optical photons are generated by scintillation and Cherenkov effect. The crystal surfaces are defined setting ground finish according to the unified model. Optical photons at the boundaries of scintillator volumes are considered as undergoing specular reflections on the micro-facets of a surface with roughness defined by the σ_α parameter [93, 94]. When an optical photon enters a silicon photodetector volume, it is absorbed and the position and time of arrival are recorded. The output of the Monte-Carlo simulation is processed to generate an electronic signal reproducing the processing of the electronic board and finally, a dataset is generated, saving a set of charges and timestamps for each coincidence event. Moreover, the ground truth information from Monte-Carlo is retained in the final dataset, for comparison.

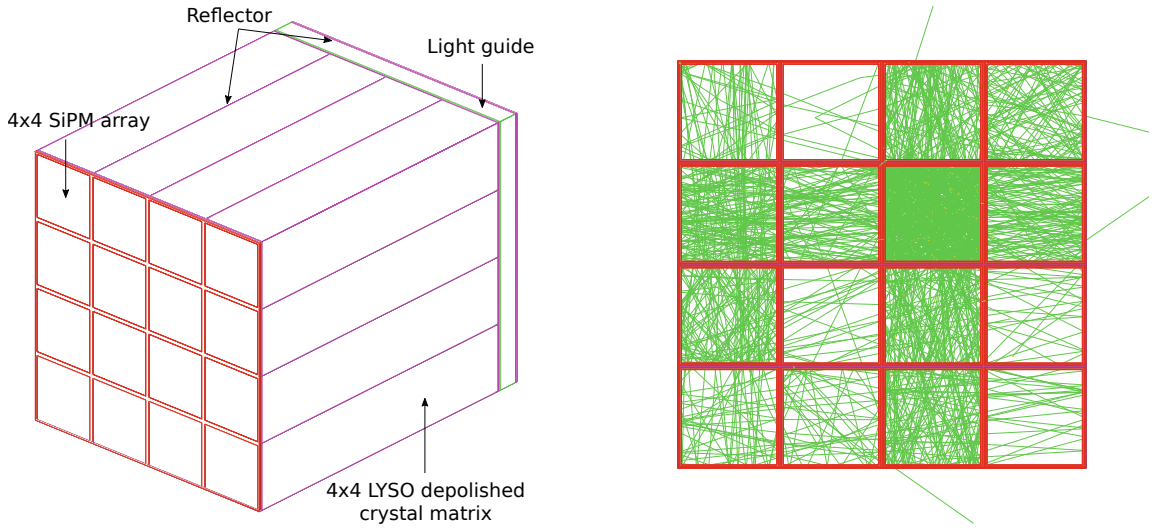

(a) (b)

Figure 8.5: (a) Simulated setup using Geant4 taking into account the composition of the crystals, their surface state, the optical coupling materials, the reflectors, and the silicon photodetectors. (b) Example of tracking of the optical photons produced by the interaction of primary gamma rays in the case of an ICS event.

8.2 Results and discussion

First, simulation runs are performed, directing a set of 511 keV gamma rays toward each crystal of the detector array. The resulting datasets are analyzed to extract sets

of sixteen calibration maps, as previously described and illustrated in Figure 8.2. In a subsequent run, one of the crystals is irradiated in a similar manner, and ICS events are selected for analysis, as depicted in Figure 8.3. The two most likely impact positions of the gamma within the two crystals of interaction are determined based on the distribution of the charge, and consequently light, on the sixteen SiPMs. The hypothesis with the highest probability is calculated according to Equation 8.4. The result is compared to the truth that is provided by the Monte Carlo simulation, focusing on both the identification of the first interaction crystal and the determination of the z_A and z_B.
The accuracy of the algorithm is evaluated as

$$accuracy = \frac{N_{correct\ assumption}}{N_{ICS\ events}} \tag{8.5}$$

Figure 8.6 illustrates the accuracy of the algorithm in determining the first crystal of interaction as a function of the number of theoretical interaction points chosen in crystals A and B, considering the events highlighted in Figure 8.3b. For this analysis, 150 iterations per crystal are selected. For the same pair of crystals, the distribution of the number of events as a function of $z_A - z_B$ is displayed in Figure 8.7a. This distribution takes into account both the Compton scattering probability (described in Equation 2.9 and Figure 2.7) and the gamma attenuation (described in Equation 2.16). Additionally, Figure 8.7b displays the accuracy of the algorithm as a function of the relative distance between the two interaction points z_A and z_B.

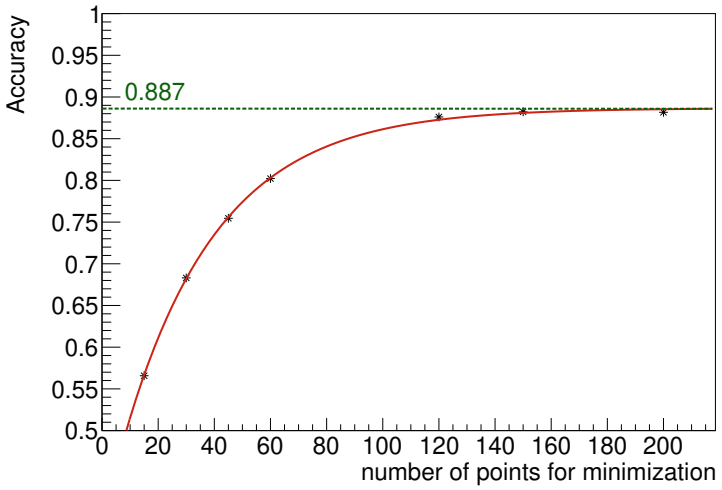

Figure 8.6: Accuracy of the algorithm in the determination of the first crystal of interaction as a function of the number of theoretical interaction points chosen in crystal A and in crystal B.

Finally, the deposited energy in the two crystals evaluated by the algorithm, along with their combined energy, is plotted as a function of the relative distance between the two interaction points z_A and z_B in Figure 8.8.

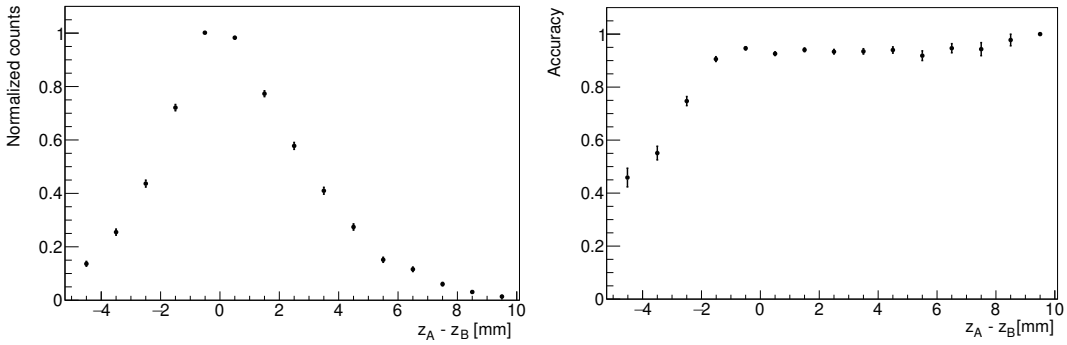

(a) (b)

Figure 8.7: (a) Distribution of the number of events as a function of $z_A - z_B$. (b) Accuracy of the algorithm as a function of the relative distance between the two interaction points z_A and z_B.

The analysis is repeated for ICS events shared with the remaining central adjacent crystals, as well as for all channel combinations when the other central crystals are irradiated. In this setup, we focus on the central crystals, which simulate the conditions of a scanner where each crystal is surrounded by nine neighboring ones. The average accuracy achieved across these measurements is 87 ± 1 %. The DOI resolution is 4.5 ± 0.2 mm in the determination of z_A and 4.6 ± 0.2 mm in the determination of z_B.

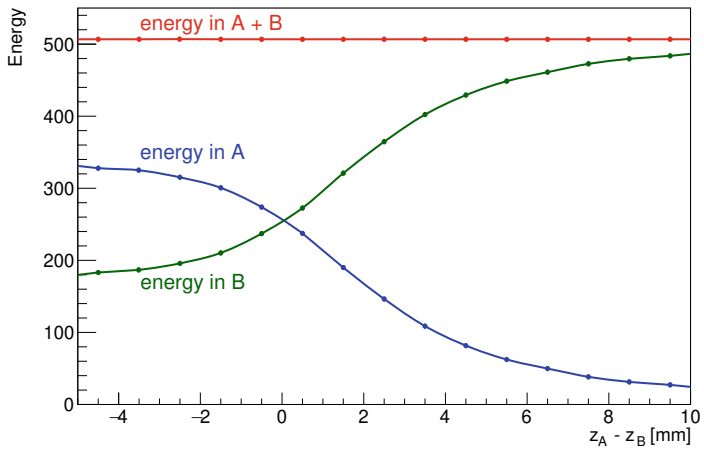

Figure 8.8: Evaluation of the deposited energy in the two crystals and their sum as a function of the relative distance between the two interaction points z_A and z_B.

8.3 Summary and Conclusion

The light-sharing detector configuration, thoroughly studied throughout this thesis work, allows the extraction of the information on the DOI with a high resolution. This information can be used to correct the DOI induced bias on the time and mitigate the parallax effect. In this work, we presented a statistical method, based on a pixellated DOI-capable detector, to estimate the multiple positions of interaction in case of inter-crystal scattering events. Specifically, we address events where a gamma photon first undergoes Compton scattering in one crystal, depositing part of its energy, and subsequently undergoes photoelectric interaction in a second crystal, depositing the remaining energy.

The accuracy of the proposed method is assessed by means of Geant4-based Monte Carlo simulations, first, to extract the calibration maps and then to select the ICS events of interest on which the algorithm is tested. The method demonstrates an accuracy of 87% in identifying the first crystal of interaction and achieves a precision of 4.6 ± 0.2 mm FWHM in determining the two interaction positions within the crystals.

V

Conclusion and Outlook

9 Summary and conclusions

THIS thesis aimed to explore and enhance the key benchmarks of TOF-PET detectors, with a particular emphasis on timing performance.

To reach this goal, all the aspects of the detector chain, including scintillating crystals, photodetectors and readout electronics, needed to be evaluated and optimized together. The scintillator of interest that has been used throughout the thesis work is LYSO:Ce. It is particularly suited for PET because of its high detection efficiency to the 511 keV gammas, and well-suited for TOF applications because of its large intrinsic light yield (41000 ph/keV) and fast decay time (τ_{eff} = 40 ns). Several photodetectors from different producers have been tested using a custom-made electronic readout board able to split the signal of each SiPM and process it respectively using a NINO 32-chip to extract a fast digital signal for time evaluation, and an amplifier to extract an analog signal for energy quantification. The new MT technology from FBK and Broadcom achieved the best results. A crystal module based on an array of sixteen polished LYSO:Ce crystals with ESR around of 15 mm length achieved timing performance of 141 ± 3 ps FWHM and 8.7 ± 0.3 %, with respect of 162 ± 2 ps from a previous work that made use of Hamamatsu 13361-3050AE-04 SiPM array.

As the frontier of timing is approaching 100 ps FWHM, with the extremely challenging final goal of reaching 10 ps, the influence of light transport on the CTR, and its dependence on the gammas DOI position, becomes no longer negligible. For this reason, a detector configuration making use of depolished crystals and a light guide on top that allows light recirculation within the matrix was tested to be able to extract the information on the DOI, in addition to the TOF and energy quantification. This is of particular importance for preclinical and organ-dedicated human PET scanners that require very high spatial resolution and that suffer from a large influence of parallax errors. The DOI-capable detector, with the Broadcom NUV-MT array, measured the DOI information with a resolution of 2.5 ± 0.2 mm FWHM. The time resolution was 247 ± 7 ps FWHM, which improved to 170 ± 5 ps FWHM after DOI correction. Although promising in terms of time resolutions, the electronic readout and digitization are not scalable to a full system due to its high power consumption and large dimensions. Therefore, the PETsys TOFPET2 ASIC from PETsys Electronics S.A. has been investigated to evaluate the performance of the detector module with a commercially

available and scalable readout electronic, which allows extraction of time and energy information as the NINO 32-chip-based readout. The standard module achieved a CTR of 193 ± 6 ps FWHM, proving that sub-200 ps FWHM timing resolution is easily reachable using commercially available crystals, photo-detectors, and electronic readout and acquisition. Using the DOI-capable module, a similar result in terms of DOI resolution, 2.6 ± 0.2 mm FWHM, was achieved. While a CTR of 216 ± 6 ps FWHM after DOI correction was measured.

Another interesting scintillator that represents a good choice for PET is BGO, in terms of its high density, stopping power and low production cost. However, due to its slow decay time and low light yield, it was substituted in the past with LSO. To overcome the dichotomy between high sensitivity and ultra-fast timing, a possible solution is to incorporate a material that guarantees high stopping power in a detector that also includes another material that provides fast emission or high light output, in a so-called heterostructure. An example is given by the combination of BGO with a plastic scintillator, such as EJ232. To be able to exploit the faint Cherenkov signal produced by BGO and the very fast production of scintillating photons of plastic, the fast SiPM signals should be combined with fast and low-noise electronic readout. Both PETsys TOFPET2 ASIC and the custom-made NINO 32-chip board demonstrated excellent performance with LYSO:Ce, as it shows good energy and time resolution, also at a high threshold of extraction of the timestamp. This is not the case for BGO or materials with slower scintillation profiles and faster electronics are needed. For this reason, a low-power low-noise high-frequency development board has been designed and tested. Using LYSO:Ce these electronics showed CTR results as good as 124 ± 3 ps FWHM with the standard matrices of 15 mm and 130 ± 2 ps FWHM with 20 mm. Employing the DOI-capable concept with 20 mm long crystals, the four central channels exhibited a CTR of 195 ± 2 ps before DOI correction. After applying the DOI correction, the CTR improved to 131 ± 2 ps FWHM. Therefore the DOI-capable matrix not only allows to acquire the timing information with the same resolution as a standard matrix but also provides information on the depth of interaction of the gamma rays inside the detector with 2.7 ± 0.2 mm FWHM resolution.

A matrix based on the concept of heterostructured scintillators was then tested. The combination of 250 μm thick BGO an EJ232 layers allows stopping the gamma via photoelectric absorption in the heavy material and depositing part of the energy of the recoil photoelectron in the fast material. The drawback is that the stratification of thin layers worsens the light transport due to the attenuation of the light produced in it and degrades the energy and time properties. However, the attenuation is strongly correlated to the DOI of the gamma and it can be exploited to retrieve its information and correct for the induced bias on the timing. To test this concept, a matrix of heterostructures was coupled on one side with the Broadcom NUV-MT array and on the other side, opposite to the photo-detectors, with a light guide. By selecting events where part of the energy was shared between the two materials, the array achieved a time resolution of 182 ± 6 ps FWHM after DOI correction.

A possibility to maintain good sensitivity, without degradation in spatial resolution, is the use of an algorithm to identify and solve Inter-Crystal Scatter events, which account for more than half of the total coincidence events acquired. If the expected charge seen by all the photo-detectors, as a function of the DOI and energy deposition, is known through calibration procedures, this information can be used to evaluate the most probable gamma interaction position across multiple crystals. The statistical method developed for this purpose was tested using Geant4 Monte Carlo simulations, demonstrating an accuracy rate of 87 % and a DOI resolution of 4.6 mm FWHM in determining the multiple gamma interaction positions.

To conclude, this work advanced the understanding of a detector concept with both TOF and DOI capability for PET. The performance was evaluated using a commercially available and scalable electronic readout board concluding that sub-200 ps timing resolution and sub 3 mm DOI resolution are reachable. Additionally, custom-designed electronics were developed and optimized to improve timing performance further towards 100 ps FWHM, while maintaining the same energy and DOI resolution using LYSO:Ce. The new design based on the high-frequency concept allowed us to approach this goal and study a new material concept that represents a compromise between high sensitivity and ultra-fast timing. Finally, a new statistical method is presented for solving the kinematics of ICS events, aiming to maintain both good sensitivity and high spatial resolution.

9.1 Outlook and directions for future research

Considering the outcome of the research summarized above, there are several potential research lines that can be pursued.

First, the overview provided on the electronic readout studied is not comprehensive, and there are many other readout methods that could be evaluated and compared [95]. Among these, we can cite FastIC [96] and the Weeroc ASIC family [97].

Second, the high-frequency readout concept is currently exploited in a single-channel environment to test the performance of various materials that are currently under research and development for different applications. This includes innovative materials for high-energy physics applications, such as GAGG [98], or for more generic applications including also PET such as nanomaterials [85] or materials exploiting different fast light production such as BaF_2 [99]. Consequently, the multi-channel low-power low-noise high-frequency readout, owing to its versatility, can be employed to evaluate matrices made of materials beyond those presented in this work. Additionally, new detector configurations and reconstruction algorithms can be tested using the developed experimental setup.

Third, the developed algorithm for Compton recovery can be tested on experimental measurements that can be performed using one of the setups tested or developed

throughout this thesis work. Furthermore, the algorithm developed for ICS events is not limited to PET applications, as it does not necessitate the acquisition of two coincident events. Specifically, it can be applied in scenarios involving single events, such as in a Compton camera, or in applications where multiple gamma sources are used simultaneously.

Acknowledgements

This work has been performed in the framework of the Crystal Clear Collaboration and supported by the CERN Austrian Doctoral Student Programme and CERN Budget for Knowledge Transfer to Medical Applications. A special thanks to all the collaborators from institutes all around the world who enriched this thesis work with their precious help and support.

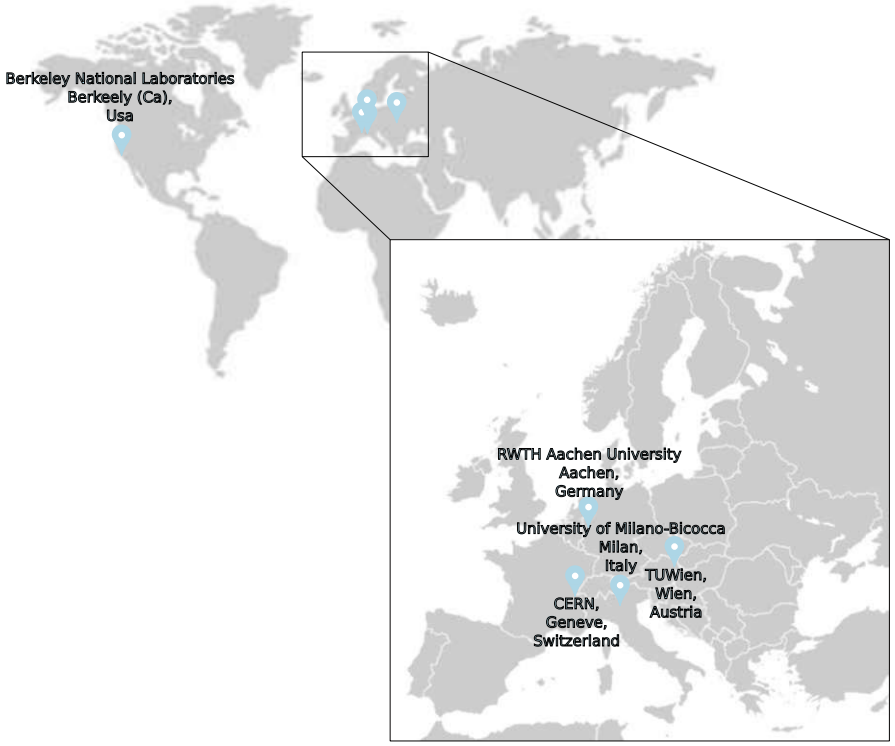

Figure 9.1: Universities and research institutions with which close collaboration was carried out during this thesis work and from which this work benefited.

First of all, thanks to Prof. Johann Marton, for supervising me on this thesis topic, for your support and belief in my research.

Thanks to Dr. Etiennette Auffray for welcoming me into their laboratory at CERN, for your guidance and knowledge transfer.

Thanks to Dr. Vanessa Nadig and Dr. Stefan Gundacker, for welcoming me in the laboratories at RWTH Aachen, for the fruitful collaboration and support.

Thanks to Dr. Joshua Cates, from Berkeley National Laboratories, for the continuous support and knowledge sharing that made my PhD experience unique.

Thanks to Prof. Marco Pizzichemi, for your uncountable help and for including me in your unique research, and thanks to the students from the University of Milano-Bicocca that I had the honor to guide.

Glossary

ADC Analog to Digital Converter. 58

ALICE A Large Ion Collider Experiment. 28

APD avalanche photodiode. 29

BGO bismuth germanate. 26

CCC Crystal Clear Collaboration. 27

CERN European Council for Nuclear Research (Conseil Européen pour la Recherche Nucléaire). 27

CMS Compact Muon Solenoid. 28

CT computed tomography. 9

CTR coincidence time resolution. 27

DAC digital to analog converter. 70

DOI depth of interaction. 24

DTR Detector Time Resolution. 34

ESR enhanced specular reflector. 54

F-18-FDG fluorine-18-fluorodeoxyglucose. 11

FEB front end board. 44

FOV field of view. 24

FWHM full width at half maximum. 12

G-APD geiger-mode avalanche photodiode. 40

GAGG gadolinium aluminium gallium garnet. 30

HEP high-energy physics. 28

HF high-frequency. 46

HQCD high-speed coaxial cable. 45

ICS Inter-Crystal Scattering. 23, 105

LHC large hadron collider. 27

LNHF low-noise high-frequency. 47, 82

LOR line of response. 10

LPLNHF low-power low-noise high-frequency. 83

LSO lutetium oxyorthosilicate. 14

LVDS low-voltage differential signaling. 44

MCP microchannel plate. 37

ML-EM maximum likelihood expectation maximization. 22

MPPC multi-pixel photon counter. 40

MRI magnetic resonance imaging. 9

NaI:Tl sodium iodide. 25

OCA optical clear adhesive. 55

OV overvoltage. 65

$PbWO_4$ lead tungstate. 28

PD photo diode. 39

PDE photon detection efficiency. 41

PET positron emission tomography. 9

PMT photomultiplier tube. 29

PSF point spread function. 24

QDC charge to digital converter. 45

QE quantum efficiency. 38

SiPM silicon photomultiplier. 29

SMA subMiniature version A. 94

SNR signal-to-noise ratio. 23

SPAD single photon avalanche diode. 40

TDC time to digital converter. 45

TOF time of flight. 10

TOT time over threshold. 44

VOR volume of responce. 24

List of Figures

List of Tables

Bibliography

[1] Siemens Healthineers. *Biograph Vision PET/CT Scanner*. Accessed: 2024-08-26. 2024.

[2] D. R. Schaart. "Physics and technology of time-of-flight PET detectors". In: *Physics in Medicine & Biology* 66.9 (2021), 09TR01.

[3] P. Lecoq. "On the way to the 10 ps time-of-flight PET challenge". In: *The European Physical Journal Plus* 137.8 (2022), pp. 1–7.

[4] S. Gundacker, R. M. Turtos, N. Kratochwil, R. H. Pots, M. Paganoni, P. Lecoq, and E. Auffray. "Experimental time resolution limits of modern SiPMs and TOF-PET detectors exploring different scintillators and Cherenkov emission". In: *Physics in Medicine & Biology* 65.2 (2020), p. 025001.

[5] M. Pizzichemi, A. Polesel, G. Stringhini, S. Gundacker, P. Lecoq, S. Tavernier, M. Paganoni, and E. Auffray. "On light sharing TOF-PET modules with depth of interaction and 157 ps FWHM coincidence time resolution". In: *Physics in Medicine & Biology* 64.15 (2019), p. 155008.

[6] R. M. Turtos, S. Gundacker, E. Auffray, and P. Lecoq. "Towards a metamaterial approach for fast timing in PET: experimental proof-of-concept". In: *Physics in Medicine & Biology* 64.18 (2019), p. 185018.

[7] J. W. Cates and C. S. Levin. "Electronics method to advance the coincidence time resolution with bismuth germanate". In: *Physics in Medicine & Biology* 64.17 (2019), p. 175016.

[8] C. Zhang, Z. Sang, X. Wang, X. Zhang, and Y. Yang. "The effects of inter-crystal scattering events on the performance of PET detectors". In: *Physics in Medicine & Biology* 64.20 (2019), p. 205004.

[9] T. F. Budinger, K. M. Brennan, W. W. Moses, and S. E. Derenzo. "Advances in positron tomography for oncology". In: *Nuclear medicine and biology* 23.6 (1996), pp. 659–667.

[10] The Nobel Prize. *The Nobel Prize in Physics 1936*. Accessed January 7, 2024. 1936. URL: https://www.nobelprize.org/prizes/physics/1936/summary/.

[11] *The Nobel Prize in Physics 1939*. NobelPrize.org. 1939. URL: https://www.nobelprize.org/prizes/physics/1939/summary/.

[12] *The Nobel Prize in Physics 1943*. NobelPrize.org. 1943. URL: https://www.nobelprize.org/prizes/chemistry/1943/hevesy/facts/.

[13] G. Treglia, R. Sadeghi, A. Del Sole, and L. Giovanella. "Diagnostic performance of PET/CT with tracers other than F-18-FDG in oncology: an evidence-based review". In: *Clinical and Translational Oncology* 16 (2014), pp. 770–775.

[14] Wikipedia. *Fluorodeoxyglucose (^{18}F)*. https://en.wikipedia.org/wiki/Fluorodeoxyglucose_(18F). Accessed: 2024-08-11. 2024.

[15] A. Del Guerra, N. Belcari, and M. Bisogni. "Positron emission tomography: its 65 years". In: *La Rivista del Nuovo Cimento* 39 (2016), pp. 155–223.

[16] J. L. Humm, A. Rosenfeld, and A. Del Guerra. "From PET detectors to PET scanners". In: *European journal of nuclear medicine and molecular imaging* 30 (2003), pp. 1574–1597.

[17] N. D. Services. *Table of Isotopes - Isotope Search*. http://nucleardata.nuclear.lu.se/toi/nucSearch.asp. Accessed: 2024-08-11. 2024.

[18] G. F. Knoll. *Radiation detection and measurement*. John Wiley & Sons, 2010.

[19] C. Melcher and J. Schweitzer. "Cerium-doped lutetium oxyorthosilicate: a fast, efficient new scintillator". In: *IEEE Transactions on Nuclear Science* 39.4 (1992), pp. 502–505.

[20] National Institute of Standards and Technology (NIST). *"XCOM: Photon cross section database,"* Accessed January 17, 2024. URL: https://physics.nist.gov/cgi-bin/Xcom/xcom2?Method=Comp&Output2=Hand.

[21] R. D. Evans and R. Evans. *The atomic nucleus*. Vol. 582. McGraw-Hill New York, 1955.

[22] T. E. Johnson, B. K. Birky, and B. Shleien. *Health physics and radiological health*. 1998.

[23] D. W. Townsend. "Positron emission tomography". In: *Diagnostic Imaging Applications*. Vol. 516. SPIE. 1985, pp. 52–55.

[24] J. Radon. "Über die Bestimmung von Funktionen durch ihre Integralwerte längs gewisser Mannigfaltigkeiten". In: *Akad. Wiss.* 69 (1917), pp. 262–277.

[25] S. Gundacker. "Time resolution in scintillator based detectors for positron emission tomography". PhD thesis. Technische Universität Wien, 2014.

[26] S. R. Cherry, J. A. Sorenson, and M. E. Phelps. *Physics in nuclear medicine*. Soc Nuclear Med, 2013.

[27] M. Conti. "State of the art and challenges of time-of-flight PET". In: *Physica Medica* 25.1 (2009), pp. 1–11.

[28] W. W. Moses. "Fundamental limits of spatial resolution in PET". In: *Nuclear Instruments and Methods in Physics Research Section A: Accelerators, Spectrometers, Detectors and Associated Equipment* 648 (2011), S236–S240.

[29] W. H. Sweet. "The uses of nuclear disintegration in the diagnosis and treatment of brain tumor". In: *New England Journal of Medicine* 245.23 (1951), pp. 875–878.

[30] F. R. Wrenn Jr, M. L. Good, and P. Handler. "The use of positron-emitting radioisotopes for the localization of brain tumors". In: *Science* 113.2940 (1951), pp. 525–527.

[31] W. Sweet. "Localization of brain tumors with positron emitters". In: *Nucleonics* 11 (1953), pp. 40–45.

[32] T. Jones and D. Townsend. "History and future technical innovation in positron emission tomography". In: *Journal of Medical Imaging* 4.1 (2017), pp. 011013–011013.

[33] H. O. Anger. "Scintillation camera". In: *Review of scientific instruments* 29.1 (1958), pp. 27–33.

[34] G. N. Hounsfield. "Computerized transverse axial scanning (tomography): Part 1. Description of system". In: *The British journal of radiology* 46.552 (1973), pp. 1016–1022.

[35] W. W. Moses. "Recent advances and future advances in time-of-flight PET". In: *Nuclear Instruments and Methods in Physics Research Section A: Accelerators, Spectrometers, Detectors and Associated Equipment* 580.2 (2007), pp. 919–924.

[36] *The Crystal Clear Collaboration*. URL: https://crystalclearcollaboration.web.cern.ch/.

[37] CMS Collaboration. "The CMS electromagnetic calorimeter project: technical design report". In: *Technical Design Report CMS. CERN, Geneva* 47 (1997).

[38] ALICE collaboration. "Technical design report of the photon spectrometer". In: *CERN/LHCC* 4 (1999).

[39] A. Gektin and M. Korzhik. "Inorganic scintillators for detector systems". In: *Berlin: Springer* (2017), pp. 20–77.

[40] *The Nobel Prize in Physics 1958*. NobelPrize.org. 1958. URL: https://www.nobelprize.org/prizes/physics/1958/summary/.

[41] G. Ariño-Estrada, G. S. Mitchell, H. Kim, J. Du, S. I. Kwon, L. J. Cirignano, K. S. Shah, and S. R. Cherry. "First Cerenkov charge-induction (CCI) TlBr detector for TOF-PET and proton range verification". In: *Physics in Medicine & Biology* 64.17 (2019), p. 175001.

[42] S. Gundacker, R. M. Turtos, E. Auffray, and P. Lecoq. "Precise rise and decay time measurements of inorganic scintillators by means of X-ray and 511 keV excitation". In: *Nuclear Instruments and Methods in Physics Research Section A: Accelerators, Spectrometers, Detectors and Associated Equipment* 891 (2018), pp. 42–52.

[43] *Eljen Technology*. URL: https://eljentechnology.com/products/plastic-scintillators/ej-232-ej-232q/.

[44] *Crystal Photonics, Inc.*

[45] *Epic Crystals*. URL: https://www.epic-crystal.com/scintillation-crystals/bgo-crystal.html%5C.

[46] S. Gundacker, E. Auffray, K. Pauwels, and P. Lecoq. "Measurement of intrinsic rise times for various L (Y) SO and LuAG scintillators with a general study of prompt photons to achieve 10 ps in TOF-PET". In: *Physics in Medicine & Biology* 61.7 (2016), p. 2802.

[47] R. Cala', N. Kratochwil, L. Martinazzoli, M. Lucchini, S. Gundacker, E. Galenin, I. Gerasymov, O. Sidletskiy, M. Nikl, and E. Auffray. "Characterization of mixed Bi4 (GexSi1- x) 3O12 for crystal calorimetry at future colliders". In: *Nuclear Instruments and Methods in Physics Research Section A: Accelerators, Spectrometers, Detectors and Associated Equipment* 1032 (2022), p. 166527.

[48] R. Bock, T. Hansl-Kozanecka, and T. Shah. "Parametrization of the longitudinal development of hadronic showers in sampling calorimeters". In: *Nuclear Instruments and Methods in Physics Research* 186.3 (1981), pp. 533–539.

[49] G. Grindhammer and S. Peters. "The parameterized simulation of electromagnetic showers in homogeneous and sampling calorimeters". In: *arXiv preprint hep-ex/0001020* (2000).

[50] D. Renker and E. Lorenz. "Advances in solid state photon detectors". In: *Journal of Instrumentation* 4.04 (2009), P04004.

[51] *Hamamatsu Technical notes*. URL: https://hub.hamamatsu.com/us/en/technical-notes/mppc-sipms.html.

[52] *Broadcom Data sheets*. URL: https://www.broadcom.com/products/optical-sensors/silicon-photomultiplier-sipm/high-performance-sipm-nuv-mt.

[53] F. Anghinolfi, P. Jarron, F. Krummenacher, E. Usenko, and M. Williams. "NINO, an ultra-fast, low-power, front-end amplifier discriminator for the Time-Of-Flight detector in ALICE experiment". In: *2003 IEEE Nuclear Science Symposium. Conference Record (IEEE Cat. No. 03CH37515)*. Vol. 1. IEEE. 2003, pp. 375–379.

[54] *PETsys Electronics SA*. URL: https://www.petsyselectronics.com/web/.

[55] J. W. Cates, W.-S. Choong, and E. Brubaker. "Scintillation and cherenkov photon counting detectors with analog silicon photomultipliers for TOF-PET". In: *Physics in Medicine & Biology* 69.4 (2024), p. 045025.

[56] PETsys Electronics S.A. *TOFPET2 ASIC Evaluation Kit - Hardware User Guide (v1.2)*. v1.2. Accessed May 2018. 2018.

[57] PETsys Electronics S.A. *TOFPET2 ASIC Evaluation Kit - Software User Guide V2018.04*. v2018.04. Accessed Apr 2018. 2018.

[58] J. W. Cates, S. Gundacker, E. Auffray, P. Lecoq, and C. S. Levin. "Improved single photon time resolution for analog SiPMs with front end readout that reduces influence of electronic noise". In: *Physics in Medicine & Biology* 63.18 (2018), p. 185022.

[59] N. Zhang and M. J. Schmand. *Bootstrapping readout for large terminal capacitance analog-SiPM based time-of-flight PET detector*. US Patent 10,128,801. Nov. 2018.

[60] J. W. Cates and W.-S. Choong. "Low power implementation of high frequency SiPM readout for Cherenkov and scintillation detectors in TOF-PET". In: *Physics in Medicine & Biology* 67.19 (2022), p. 195009.

[61] S. Gundacker, R. M. Turtos, E. Auffray, M. Paganoni, and P. Lecoq. "High-frequency SiPM readout advances measured coincidence time resolution limits in TOF-PET". In: *Physics in Medicine & Biology* 64.5 (2019), p. 055012.

[62] P. Lecoq. *The 10 ps TOF-PET challenge*. https://the10ps-challenge.org/.

[63] F. Loignon-Houle, S. Gundacker, M. Toussaint, F. C. Lemyre, E. Auffray, R. Fontaine, S. A. Charlebois, P. Lecoq, and R. Lecomte. "DOI estimation through signal arrival time distribution: a theoretical description including proof of concept measurements". In: *Physics in Medicine & Biology* 66.9 (2021), p. 095015.

[64] G. Terragni, M. Pizzichemi, E. Roncali, S. R. Cherry, J. Glodo, K. Shah, G. Ariño-Estrada, E. Auffray, A. Ghezzi, and N. Kratochwil. "Time resolution studies of thallium based Cherenkov semiconductors". In: *Frontiers in Physics* 10 (2022), p. 93.

[65] S. Gundacker, A. Knapitsch, E. Auffray, P. Jarron, T. Meyer, and P. Lecoq. "Time resolution deterioration with increasing crystal length in a TOF-PET system". In: *Nuclear Instruments and Methods in Physics Research Section A: Accelerators, Spectrometers, Detectors and Associated Equipment* 737 (2014), pp. 92–100.

[66] M. Pizzichemi, G. Stringhini, T. Niknejad, Z. Liu, P. Lecoq, S. Tavernier, J. Varela, M. Paganoni, and E. Auffray. "A new method for depth of interaction determination in PET detectors". In: *Physics in Medicine & Biology* 61.12 (2016), p. 4679.

[67] I. Vilardi, A. Braem, E. Chesi, F. Ciocia, N. Colonna, F. Corsi, F. Cusanno, R. De Leo, A. Dragone, F. Garibaldi, et al. "Optimization of the effective light attenuation length of YAP:Ce and LYSO:Ce crystals for a novel geometrical PET concept". In: *Nuclear Instruments and Methods in Physics Research Section A: Accelerators, Spectrometers, Detectors and Associated Equipment* 564.1 (2006), pp. 506–514.

[68] J. Trummer, E. Auffray, and P. Lecoq. "Depth of interaction resolution of LuAP and LYSO crystals". In: *Nuclear Instruments and Methods in Physics Research Section A: Accelerators, Spectrometers, Detectors and Associated Equipment* 599.2-3 (2009), pp. 264–269.

[69] S. Merzi, S. E. Brunner, A. Gola, A. Inglese, A. Mazzi, G. Paternoster, M. Penna, C. Piemonte, and M. Ruzzarin. "NUV-HD SiPMs with metal-filled trenches". In: *Journal of Instrumentation* 18.05 (2023), P05040.

[70] G. Stringhini, M. Pizzichemi, A. Ghezzi, A. Stojkovic, M. Paganoni, and E. Auffray. "Development and evaluation of a practical method to measure the Depth of Interaction function for a single side readout PET detector". In: *Journal of Instrumentation* 11.11 (2016), P11014.

[71] R. Bugalho, A. Di Francesco, L. Ferramacho, C. Leong, T. Niknejad, L. Oliveira, L. Pacher, M. Rolo, A. Rivetti, M. Silveira, et al. "Experimental results with TOFPET2 ASIC for time-of-flight applications". In: *Nuclear Instruments and Methods in Physics Research Section A: Accelerators, Spectrometers, Detectors and Associated Equipment* 912 (2018), pp. 195–198.

[72] A. Di Francesco, R. Bugalho, L. Oliveira, L. Pacher, A. Rivetti, M. Rolo, J. Silva, R. Silva, and J. Varela. "TOFPET2: a high-performance ASIC for time and amplitude measurements of SiPM signals in time-of-flight applications". In: *Journal of Instrumentation* 11.03 (2016), p. C03042.

[73] V. Nadig, M. Yusopova, H. Radermacher, D. Schug, B. Weissler, V. Schulz, and S. Gundacker. "A comprehensive study on the timing limits of the TOFPET2 ASIC and on approaches for improvements". In: *IEEE Transactions on Radiation and Plasma Medical Sciences* 6.8 (2022), pp. 893–903.

[74] *Broadcom MT 4x4 array*. URL: https://www.broadcom.com/products/optical-sensors/silicon-photomultiplier-sipm/afbr-s4n44p164m.

[75] S. Brunner and D. Schaart. "BGO as a hybrid scintillator/Cherenkov radiator for cost-effective time-of-flight PET". In: *Physics in Medicine & Biology* 62.11 (2017), p. 4421.

[76] G. Ariño-Estrada, E. Roncali, A. R. Selfridge, J. Du, J. Glodo, K. S. Shah, and S. R. Cherry. "Study of Čerenkov light emission in the semiconductors TlBr and TlCl for TOF-PET". In: *IEEE transactions on radiation and plasma medical sciences* 5.5 (2020), pp. 630–637.

[77] P. Lecoq. *ERC Advanced Grant TICAL, GA:338953*. https://erc.europa.eu/projects-figures/erc-funded-projects/results?search_api_views_fulltext=338953. 2014.

[78] F. Pagano. "Heterostructured Scintillators: a Novel Approach to Achieve High Sensitivity and Fast Timing in TOF-PET". PhD thesis. Università degli Studi di Milano-Bicocca, 2024.

[79] F. Pagano, N. Kratochwil, M. Salomoni, M. Pizzichemi, M. Paganoni, and E. Auffray. "Advances in heterostructured scintillators: toward a new generation of detectors for TOF-PET". In: *Physics in Medicine & Biology* 67.13 (2022), p. 135010.

[80] F. Pagano, N. Kratochwil, I. Frank, S. Gundacker, M. Paganoni, M. Pizzichemi, M. Salomoni, and E. Auffray. "A new method to characterize low stopping power and ultra-fast scintillators using pulsed X-rays". In: *Frontiers in Physics* 10 (2022), p. 1021787.

[81] CAEN. *V1742 Technical Information Manual*. https://www.caen.it/products/v1742/. 2024.

[82] D. Stricker-Shaver, S. Ritt, and B. J. Pichler. "Novel calibration method for switched capacitor arrays enables time measurements with sub-picosecond resolution". In: *IEEE Transactions on Nuclear Science* 61.6 (2014), pp. 3607–3617.

[83] V. Nadig, M. Hornisch, J. Oehm, K. Herweg, V. Schulz, and S. Gundacker. "16-channel SiPM high-frequency readout with time-over-threshold discrimination for ultrafast time-of-flight applications". In: *EJNMMI physics* 10.1 (2023), p. 76.

[84] G. Konstantinou, R. Latella, L. Moliner, L. Zhang, J. M. Benlloch, A. Gonzalez, and P. Lecoq. "A proof-of-concept of cross-luminescent metascintillators: testing results on a BGO: BaF2 metapixel". In: *Physics in Medicine & Biology* 68.2 (2023), p. 025018.

[85] K. Děcká, F. Pagano, I. Frank, N. Kratochwil, E. Mihóková, E. Auffray, and V. Čuba. "Timing performance of lead halide perovskite nanoscintillators embedded in a polystyrene matrix". In: *Journal of Materials Chemistry C* 10.35 (2022), pp. 12836–12843.

[86] F. Pagano, N. Kratochwil, C. Lowis, W.-S. Choong, M. Paganoni, M. Pizzichemi, J. W. Cates, and E. Auffray. "Enhancing timing performance of heterostructures with double-sided readout". In: *Physics in Medicine & Biology* 69.20 (2024), p. 205012.

[87] M. Rafecas, G. Böning, B. Pichler, E. Lorenz, M. Schwaiger, and S. Ziegler. "Inter-crystal scatter in a dual layer, high resolution LSO-APD positron emission tomograph". In: *Physics in Medicine & Biology* 48.7 (2003), p. 821.

[88] J. E. Gillam, P. Solevi, J. F. Oliver, and M. Rafecas. "Inclusion of inter crystal scatter data in PET". In: *2012 9th IEEE International Symposium on Biomedical Imaging (ISBI)*. IEEE. 2012, pp. 62–65.

[89] J. E. Gillam, P. Solevi, J. F. Oliver, C. Casella, M. Heller, C. Joram, and M. Rafecas. "Sensitivity recovery for the AX-PET prototype using inter-crystal scattering events". In: *Physics in Medicine & Biology* 59.15 (2014), p. 4065.

[90] P. Peng, M. S. Judenhofer, and S. R. Cherry. "Compton PET: a layered structure PET detector with high performance". In: *Physics in Medicine & Biology* 64.10 (2019), 10LT01.

[91] A. Polesel et al. "Studies on a PET module prototype for the recovery of Compton events". PhD thesis. Università degli Studi di Milano-Bicocca, 2021.

[92] S. Agostinelli, J. Allison, K. a. Amako, J. Apostolakis, H. Araujo, P. Arce, M. Asai, D. Axen, S. Banerjee, G. Barrand, et al. "GEANT4—a simulation toolkit". In: *Nuclear instruments and methods in physics research section A: Accelerators, Spectrometers, Detectors and Associated Equipment* 506.3 (2003), pp. 250–303.

[93] M. Stockhoff, S. Jan, A. Dubois, S. R. Cherry, and E. Roncali. "Advanced optical simulation of scintillation detectors in GATE V8. 0: first implementation of a reflectance model based on measured data". In: *Physics in Medicine & Biology* 62.12 (2017), p. L1.

[94] E. Roncali, M. Stockhoff, and S. R. Cherry. "An integrated model of scintillator-reflector properties for advanced simulations of optical transport". In: *Physics in Medicine & Biology* 62.12 (2017), p. 4811.

[95] V. V. Nadig. "Time resolution limits on the way towards a positron emission tomography detector block with a time-of-flight resolution of 100 ps and depth-of-interaction encoding for 511 keV photons". PhD thesis. RWTH Aachen University, 2024.

[96] S. Gómez, J. Alozy, M. Campbell, J. M. Fernandez-Tenllado, R. Manera, J. Mauricio, C. Pujol, D. Sanchez, A. Sanmukh, A. Sanuy, et al. "FastIC: a fast integrated circuit for the readout of high performance detectors". In: *Journal of Instrumentation* 17.05 (2022), p. C05027.

[97] Weeroc. *Weeroc: Innovative Solutions for Your Detector Readout Needs.* Accessed: 2024-08-23. 2024.

[98] L. Martinazzoli, S. Nargelas, P. Boháček, R. Calá, M. Dušek, J. Rohlíček, G. Tamulaitis, E. Auffray, and M. Nikl. "Compositional engineering of multicomponent garnet scintillators: Towards an ultra-accelerated scintillation response". In: *Materials Advances* 3.17 (2022), pp. 6842–6852.

[99] R. Calà et al. "Exploring Novel Scintillating Materials and Light Production Mechanisms for Next-Generation High Energy Physics Detectors". PhD thesis. Università degli Studi di Milano-Bicocca, 2024.